IS-T 1892

Electrochemical and Scanning Probe Microscopic Characterization of Spontaneously Adsorbed Organothiolate Monolayers at Gold

by

Wong, Sze-Shun Season

PHD Thesis submitted to Iowa State University

Ames Laboratory, U.S. DOE

Iowa State University

Ames, Iowa 50011

Date Transmitted: December 10, 1999

PREPARED FOR THE U.S. DEPARTMENT OF ENERGY

UNDER CONTRACT NO. W-7405-Eng-82.

DISCLAIMER

AVAILABILITY:

To DOE and DOE contractors: Office of Scientific and Technical Information
P.O. Box 62
Oak Ridge, TN 37831

prices available from: (615) 576-8401
FTS: 626-8401

To the public: National Technical Information Service
U.S. Department of Commerce
5285 Port Royal Road
Springfield, VA 22161

TABLE OF CONTENTS

ACKNOWLEDMENTS

This work would not have been possible without the support of many people. They have contributed to my growth personally and professionally.

First, I would like to thank my major professor Marc Porter for his guidance and encouragement for the past five years. I especially admire his willingness to explore the new frontier of science.

Special thanks to Hajime Takano and C.-J. Zhong, whose assistance in this research was invaluable. Thanks are also extended to Brent Dawson and Janese O'Brien, who each voluntarily helped to edit my writings on many occasions. Further, the help of many formers members, including Man-Kit Ho, En-Yi Ting, John Green, Mark and Christie McDermott, Vivian Jones, Neal Simmons, are greatly appreciated. Their advice on research really helped me to get started when I was new to graduate school. To all other Porter group members, former and present, thanks for many insightful discussions, work-related and otherwise! Others who deserve special thanks include our group administrative specialist Becky Staedtler who always keep us well informed; and Drew Fullerton " the waste guy" from ES&HA for picking up our group's foul-smelling thiols waste bottles without complaints.

Appreciation is also extended to Professor Dennis Johnson, who gave me opportunity to collaborate with his student and personal friend, Matthew Johll.

To Drs Kirt Dreyer and Steven Spigarelli at Bemidji State University, I extend my appreciation for their guidance and encouragement. To Brenda Neri, the Resident Hall Director of Pine Hall, thanks for hiring me as the Resident Assistant. The leadership and interpersonal skills I learned have proven invaluable to my personal growth.

For their unconditional love and understanding, I would like to give my deepest appreciation to my parents Kam-Choi Wong, Sui-Kwan Sin, my brother Sze-Ling, my sisters Silvia and Sui-Lan, and many relatives of my family. Without their wholehearted support, I will have never been able to overcome the obstacles I faced during my nine years of stay in the U.S.

Last, but not least, I am eternally indebted to my savior Jesus Christ and His Church and the brothers and sisters in Ames. His peace and love, which transcends all understanding, have been guarding my heart and my mind. I can do everything through Him who gives me strength.

This work was performed at Ames Laboratory under Contract No. W-7405-Eng-82 with the U.S. Department of Energy. The United States government has assigned the DOE Report number IS-T 1892 to this dissertation.

GENERAL INTRODUCTION

A host of significant processes in the life and physical sciences (e.g., biological recognition, heterogeneous catalysis, corrosion, and mechanical lubrication) are controlled by interfacial architectures.[1-3] The origins of many of these macroscopic interfacial processes are controlled by the molecular level interactions at condensed phase interfaces. The development of methods that can detect differences in the composition and orientational disposition of these architectures at high spatial resolution is therefore technologically important. To this end, there are a number of techniques that have the capability to resolve spatially the chemical composition of the interfaces (e.g., secondary ion mass spectrometry,[4-6] scanning electron microscopy,[7,8] and FTIR microspectroscopy[9-11]) These techniques, however, have operative resolutions at micron length scales. With the invention and the development of a range of techniques commonly called scanning probe microscopy (SPM), probing details of interfaces at molecular length scales has now become a reality.

A main research interest of our group is to explore the utility of the many variants of SPM to map the chemical distribution of surface functional groups, exploiting a range of interfacial properties (e.g., friction and adhesion) as contrast mechanisms. Macroscopic level characterization of these assemblies by techniques such as infrared spectroscopy, ellipsometry, contact angle measurements, electrochemistry, and X-ray photoelectron spectroscopy has yielded details about the average population of the adsorbates.[12] It is the central goal of the research in this dissertation to develop a better understanding of the monolayer formation process, the spatial distribution of differing chemical functional groups

within the monolayer, and the orientation of the end-groups by combining the insights gained from SPM with those from macroscopic characterization techniques.

Scanning Probe Microscopy

Microscopy traditionally refers to the visualization of a small object by focusing an appropriate probe (visible light or electrons) on it followed by subsequent image reconstruction. The inventions of the scanning tunneling microscope (STM) by Binnig, Rohrer, and Gerber[13,14] in 1982 and the atomic force microscope (AFM) (also known as the scanning force microscope (SFM)) by Binnig, Quate, and Gerber in 1986[15] have redefined the field of microscopy. This new class of instruments, generally referred to as scanning probe microscopes, is now routinely used at laboratories to image samples with sub-nanometer resolution. Overall ease of use of these techniques and compatibility for operation in a variety of environments (e.g., air, liquid, and vacuum) has also contributed to their wide spread popularity. The early success in the imaging of atom-by-atom spacings of the Si(111)-(7x7) reconstruction,[15] highly ordered pyrolytic graphite (HOPG),[16,17] Au(111),[18] aromatic adsorbates,[19] the molecular spacing of organized organic films,[20,21] and the molecular topography of DNA[22-25] are but a few examples.

The following section presents an overview of SPM and includes a broad introduction to the fundamental aspects of the technique. Two subsequent subsections detail the key aspects of scanning tunneling microscopy (STM) and scanning force microscopy (SFM). In all scanning probe microscopes, a probe capable of interacting with a sample and a micropositioning actuator with an electrical feedback mechanism are common features. SPM

relies heavily on the development and use of piezoelectric materials as micropositioning elements for the sample or probe. A piezoelectric material (e.g., lead zircon titanate (PZT) ceramic) reacts to an applied electric field by extending in the direction perpendicular to the field. These dimensional changes can be precisely controlled at the sub-angstrom level. This extraordinary positional precision allows controllable movement of the probe or sample, and the potential of imaging at a comparable resolution.

An image is generally obtained by scanning the probe or the sample in a raster-like motion while measuring the probe-sample interaction. Movement in all three dimensions requires three different piezoelectric elements. STM, which relies on the very short-range nature of the tunneling process, functions by scanning a sharp metal tip 5-50 Å above the surface of a conducting or semiconducting sample.[26] Conversely, in its original design, SFM tracks surface topography by using a probe tip in contact with the sample surface, a principle similar to the action of a stylus profilometer[27,28] but at a significantly higher resolution and with lower applied force (10^{-8} to 10^{-13} N) on the sample. Detecting forces rather than tunneling currents means that neither the probe nor sample need to be conductive. The ability to image nonconductive materials greatly expands the range and scope of the applicability of SPM. There is no doubt that the astonishing application of SPM will continue, bringing a feverish pace of discovery in many areas of science.

Scanning Tunneling Microscopy

A number of excellent books[26,29-33] and reviews[34-37] of STM are available and provide in-depth discussions on both the theory of and issues in the application of STM as a

surface characterization tool. STM images, explained in the simplest way, are maps of the tunneling current recorded as the tip rasters across the sample. Operationally, STM employs a piezoelectric micropositioner to position a sharp metal tip, often made of Pt or W, within a few angstroms of a conductive sample surface. When the tip surface and sample surface are brought close enough together that their wave functions overlap, electrons tunnel through the classically insulating barrier when a bias voltage, V, is applied across the tip and the sample. The resulting tunneling current, I_t,[38] is

$$I_t \propto exp\ (-2kd) \tag{1}$$

where k is the decay constant for the wavefunctions ($k = \sim 12\ nm^{-1}$ for gold) in the tunneling barrier and d is the tip-sample separation. The decay constant is related to the height of the potential energy barrier through which electrons must tunnel. Equation (1) relates the tunneling current to the effective function of the surface, ϕ, since

$$k = \eta^{-1} (2m\phi)^{1/2} \tag{2}$$

where η is Planck's constant divided by 2π, and m is the mass of an electron.

Note that the tunneling current is exponentially dependent on the tip-sample separation, d. Using a typical work function of 4 eV and a k of 1.0 $Å^{-1}$, the tunneling current decreases by an order of magnitude for a 1 Å increase in the tip-sample separation. This high level of sensitivity of the tunneling current on the separation distance provides basis for the technique's astonishing vertical resolution of 0.01 Å.

Unfortunately, the simple one-dimensional model used above does not provide a full description of STM. The electronic structures of the tip and the surface are involved in a complex fashion which really demands a three-dimensional treatment. One of the most

widely used theories of STM is that of Tersoff and Hamann.[39] Here, the full general expression for the tunneling current is:

$$I_t = \left(\frac{2\pi e}{\eta}\right) e^2 V \sum_{\mu\nu} \left|M_{\mu\nu}\right|^2 \delta\left(E_\nu - E_F\right)\delta\left(E_\mu - E_F\right) \tag{3}$$

where E_F is the Fermi energy, E_μ is the energy of the state ψ_μ in the absence of tunneling, and $M_{\mu\nu}$ is the tunneling matrix element between states ψ_μ of the probe tip and ψ_ν of the sample, given by:

$$M_{\mu\nu} = \left(\frac{\eta^2}{2m}\right) \int dS\left(\psi_\mu^* \nabla \psi_\nu - \psi_\nu \nabla \psi_\mu^*\right) \tag{4}$$

Working on the assumption that the STM tip is spherical, one arrives at the following expression for the tunneling current[39]:

$$I_t = 32\pi^3 \eta^{-1} e^2 V \phi_o^2 D_t\left(E_F\right) R_t^2 k^{-4} e^{2kR_t} \sum \left|\psi_\nu\left(r_o\right)\right|^2 \delta\left(E_\nu - E_F\right) \tag{5}$$

in which ϕ_o is the work function, R is the radius of curvature of the tip, and $D_t(E_F)$ is the density of states at the Fermi level per volume of the tip. Thus the tunneling current is proportional to the local density of states at the Fermi level and at the center of the STM tip. This means that the STM can provide a direct image of quantum mechanical electron states at the surface.

STM images are usually generated under two modes of operation: the "height" (constant current) mode and the "current" (constant height) mode. In height mode imaging, a feedback mechanism is enabled that maintains a constant current (i.e., a setpoint current) while under a constant bias V. Therefore, the vertical position of the tip is altered to maintain a constant current while scanning. The voltage signal required to change the vertical tip

position of the z piezoelectric segment is then converted to a "height" image. A "height" image actually represents a constant charge density contour of the surface and altering the set point current or bias voltage creates contour of different charge density.

STM imaging operation can also be carried out in the "current" mode. In this mode, the z piezoelectric element is turned off and the tip is rastered in the x-y plane without any change in z position. The variation in tunneling current is then recorded and converted to height information when plotted as a function of the x-y coordinates. There are advantages inherent in both modes of operation; the "height" mode produces contrast directly related to electron charge density profiles while the "current" mode provides faster scan rates as it is not limited by the time constant of the z piezoelectric element.

Despite the ease of obtaining STM images with very high levels of resolution, one should always note that in reality the STM image represents a complex convolution of the structures of the tip and the sample surface. The tip structure plays an important role in determining the nature of the STM image. Variations in tip atomic structure may cause variations in the STM image, thus potentially complicating data interpretations.

Scanning Force Microscopy

Since its invention in 1986, the SFM has quickly become an invaluable tool in many research fields. A number of excellent books[26,33,40,41] and reviews[37,42-44] of SFM are available, ranging from discussions of fundamental principles to instrument design issues. Operationally, SFM is not much different from STM. However, the processes involved in tip-sample interactions are fundamentally different. Instead of a tunneling current, SFM

monitors the physical deflection of a cantilever-mounted tip as it interacts with the sample. These interactions include a variety of short- and long-range intermolecular forces (e.g., van der Waals, magnetic, and electrostatic forces). A number of methods have been designed to detect the deflection of the cantilever, including capacitance,[45] interferometry,[46] tunneling current,[15] and optical deflection.[47] All of the experimental data presented herein were obtained from an optical deflection type SFM (Figure 1) which consists of three major components: a cantilever-mounted tip, a piezoelectric micropositioner, and an electrical feedback mechanism for the micropositioner (not shown). A laser beam is reflected off the back of a cantilever (usually gold coated to enhance reflectivity and reduce thermal excitation), onto a mirror, and then to a quadrant, position-sensitive photodiode. This system can track the normal displacement (vertical motion) and the torsion of the cantilever simultaneously. In addition, the optical lever created by the reflected beam has the effect of amplifying the cantilever deflection, resulting in vertical detection limits on the order of 0.01 nm.

Figure 2 shows a scanning electron micrograph of a commercially available, microfabricated cantilever with a pyramidal tip. Cantilevers come in a wide range of sizes, shapes, and material compositions (e.g., silicon nitride (Si_3N_4) and silicon (Si)). Typical radi of curvature are 5-100 nm, with normal force constants (k_N) ranging from 0.01 N/m to 100 N/m. Therefore, the appropriate selection of cantilevers is critical and must be determined in accordance with the goals of the experiments.

Although there have been many novel techniques or detection modes designed and developed from the original SFM design, including force modulation microscopy (FM-

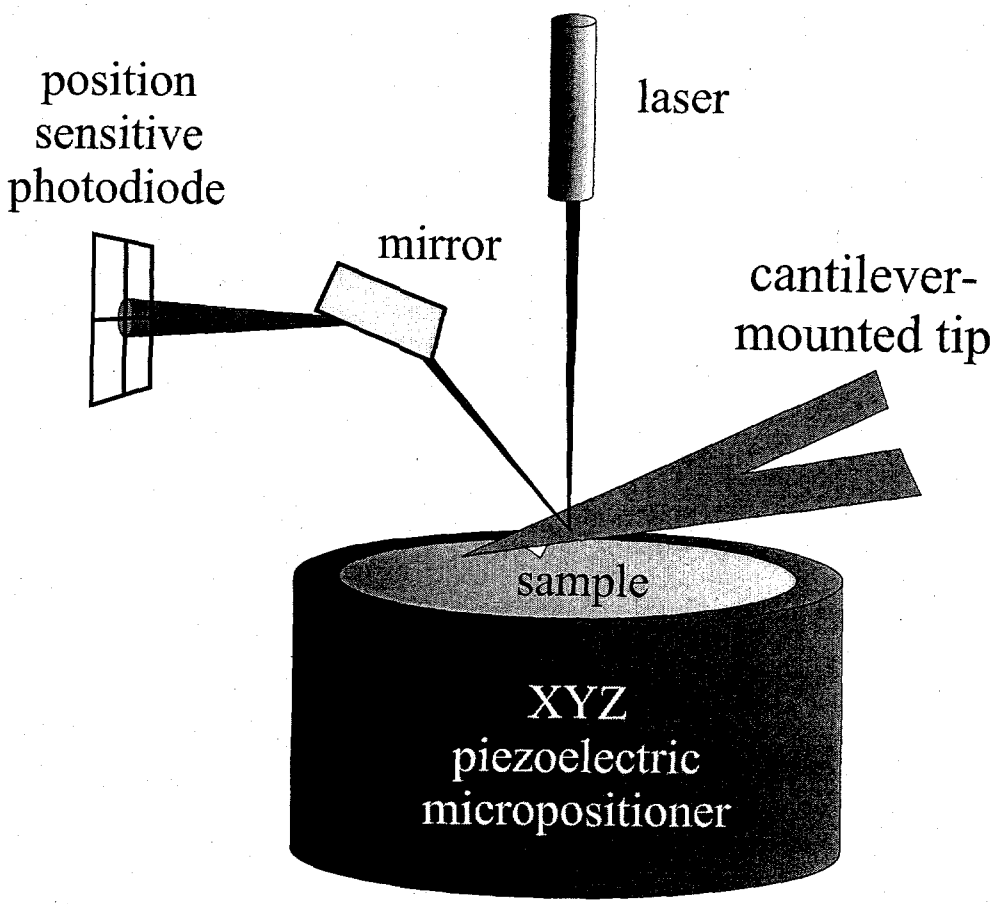

Figure 1. The principal components for an optical lever type SFM. The laser beam is reflected off the back of the cantilever onto a position sensitive photodiode.

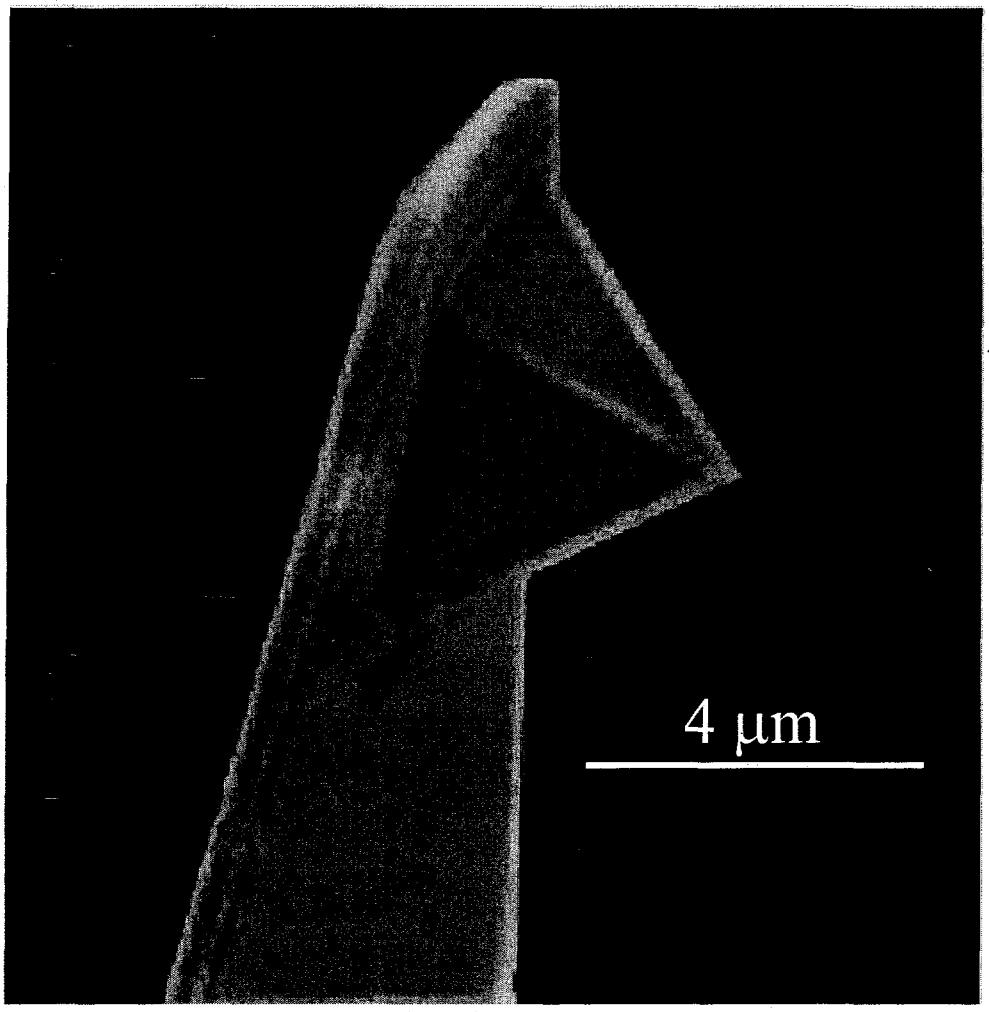

Figure 2. Scanning electron micrograph of a pyramidal tip at the end of a microfabricated silicon nitride cantilever.

SFM),[48,49] tapping mode SFM (TM-SFM),[50] electric force microscopy (EFM),[51-53] and magnetic force microscopy (MFM),[54,55] the most popular operational mode is still the contact mode, where the tip is brought into physical contact with the sample surface. The micropositioner, attached to the sample holder, is slaved to the feedback electronics in order to maintain a preset imaging force, which is monitored by the vertical deflection sensor while the sample is scanned under the tip. As the sample is rastered under the tip, the vertical deflection of the tip is used to map out surface topography. A map of the surface composition can also be constructed if there are topographical differences that can be directly correlated with compositional and/or other structural expectations.

When contact mode SFM is used, it is important to know the amount of force applied on the sample surface in order to avoid damaging the sample and obtaining images with associated artifacts. The normal load (F_N) can be calculated from the force-distance curve, often referred to simply as the force curve. The force curve is obtained by first bringing the tip and sample into close proximity but with no detectable interactions. At such separation distance, the cantilever is in its non-interacting equilibrium position and the cantilever displacement is unaffected by the change of the tip-sample separation. When the separation distance continue to decrease, various long-and short-range forces can induce a deflection of the cantilever. This deflection (bending) of the cantilever is monitored by the vertical segments of the photodetector as a function of the tip-sample separation distance. As the separation distance decreases further, the gradient of interaction force exceeds the force constant of the cantilever and the tip jumps into contact with the surface. The tip and surface are in contact, inducing a positive deflection of the cantilever. It is in this region that elastic

properties of the sample can be measured. On retraction, because of the adhesion between the tip and sample, the cantilever has to be pulled a large distance (a negative cantilever deflection) away from the surface until it snaps back, breaking all contact with the surface. The bending of the cantilever measured during the approach, contact and retraction portions of the cycle is plotted as a force-curve and is depicted in Figure 3. The cantilever displacement (Δz) is then converted into a force according to the relationship

$$F_N = k_N \Delta z \tag{6}$$

In addition to being used in determining the force applied to a sample, force curve characterizations have proven invaluable to chemical and biological analyses, such as mapping surface composition and determining the forces and energetics required to stretch and unwind DNA duplexes and proteins.[56-59]

To this point, the discussion of the transduction mechanism has centered on deflections of the tip normal to the surface. However, the force generated as the tip is moved across the sample surface perpendicular to the principal axis of the cantilever can also serve as a basis for an imaging mechanism. Lateral forces, commonly referred as friction forces, cause the cantilever to twist about its long axis, the extent of which can be monitored by the lateral segments of the quadrant position-sensitive photodetector. A plot of the torsional response of the tip with respect to the x-y movement of the sample results in a "friction loop". The detector signal difference in the magnitudes of the trace and retrace scans of the sample in the friction loop is indicative of the energy dissipated in the scan.[60,61] For example, in the friction loops of an uncoated gold surface and gold surface modified with an octadecanethiolate monolayer (Figure 4), the smaller signal difference for the thiolate-coated

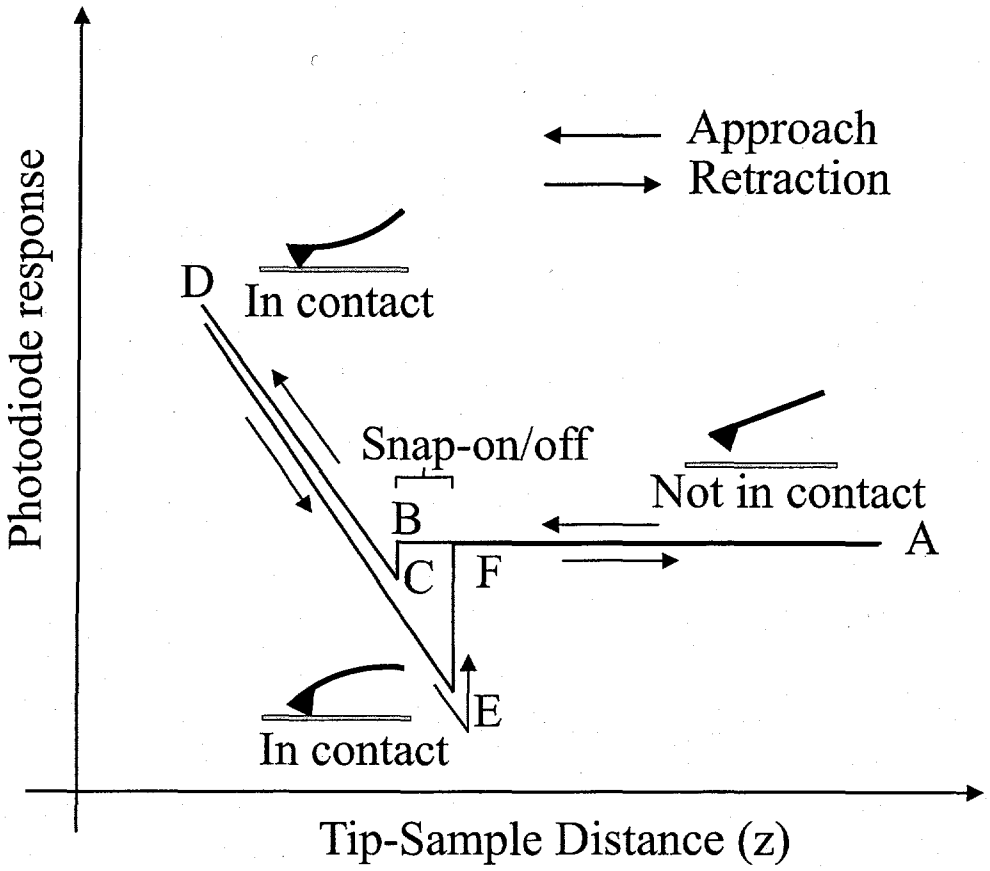

Figure 3. An idealized force curve. **A**. The tip-sample separation, z, is large and there is no measurable interaction. **Segment A-B**. The attractive force regime: z is decreased and the probe and sample begin to interact, but the strength of the interaction is less than the restoring force of the cantilever. **B**. The relatively sudden drop at B toward C occurs when the tip-sample interactions become greater than the cantilever restoring force. **C**. The tip and the surface are in "contact". **Segment C-D and segment D-E.** The tip and sample move together (C-D) or are pulled apart (D-E) with the slopes of the two segments reflecting a "hard" microcontact (segments offset for illustrated purposes). The slope of the segment C-D is indicative of the short-range repulsive force and it may be dependent of tip or sample. **E**. Adhesion contact is ruptured at this point because the cantilever restoring force exceeds the adhesive forces. **F**. The tip and the sample return to the non-interacting large separation.

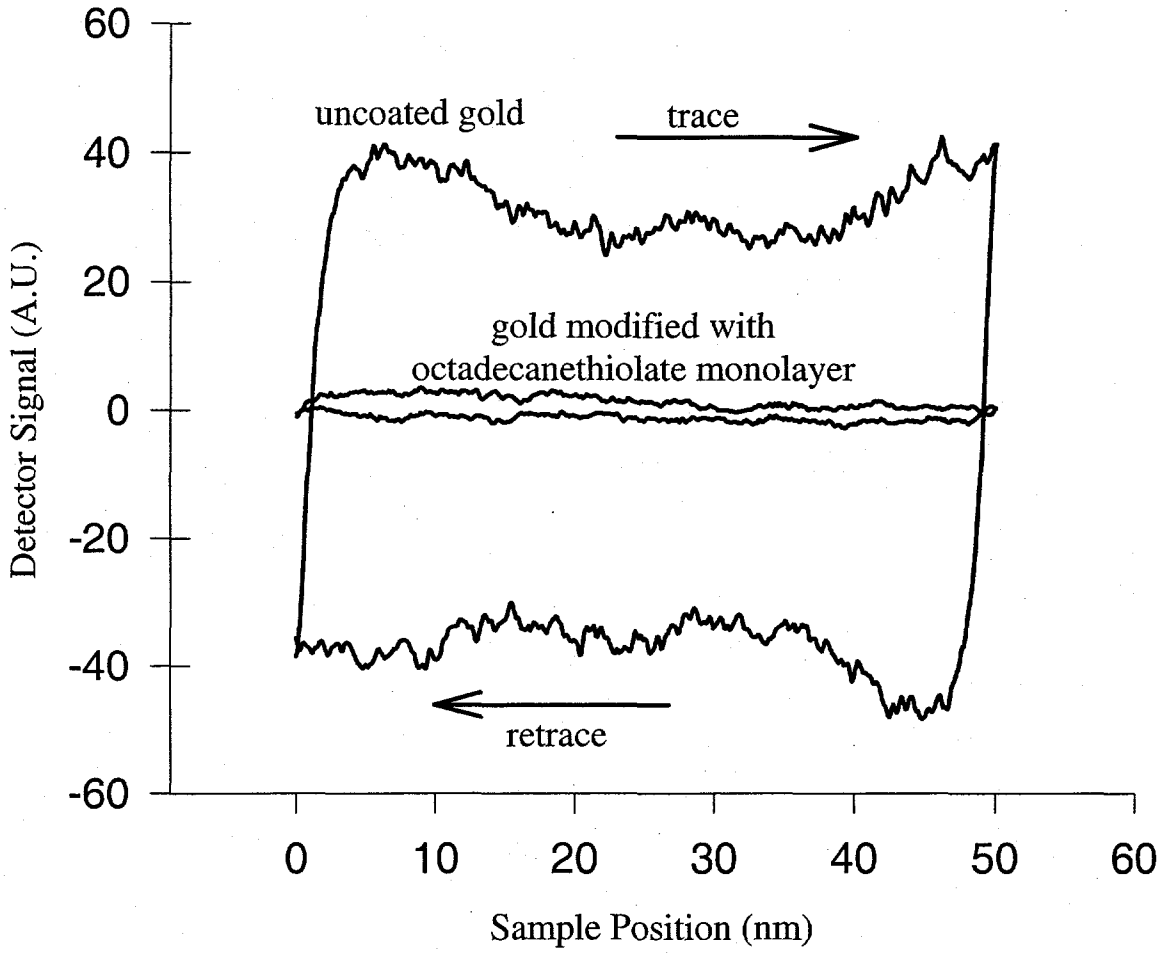

Figure 4. Friction loop of an uncoated gold surface and a gold surface modified with an octadecanethiolate monolayer (Adopted from ref 60).

gold is diagnostic of the boundary lubricant properties of the long chain monolayer.[60] With knowledge of the detector sensitivity to the twist of the cantilever and the torsional force constant of the cantilever (k_t, typical value:1-500 N/m), the friction force at the tip-sample microcontact[41,62] can be quantified.

Although friction-based scanning force microscopy, often referred to friction force microscopy or FFM, has been used extensively to study the nanoscale topography of many different interfacial materials, many researchers have used FFM to map surface composition.[63-69] The idea of compositional mapping by FFM arises from the fact that friction at a microcontact is a function of the contact load, the area of contact, and the surface free energies of the two contacting materials.[70-72] Therefore, variations in the interactions of the tip with different materials on a surface under the same applied normal load[70-74] will translate into different observed friction. Friction images therefore provide information about the spatial distribution of the different materials across interfaces as long as the friction difference can be detected. FFM has especially been successful in mapping spatial arrangement of organothiolate monolayers with different functional groups on the same surface[75-77] due to the well-defined structure of the monolayer system, the availability of end-group modified organothiols, and the invention of microcontact printing technique.[78] This technique, which will be covered later in this section, permits the controlled transfer of organothiols onto localized areas of a surface, which is not possible with solution deposition.

Furthermore, FFM can be used to examine systems whose frictional properties change with time.[79-82] Since the resolution of the FFM depends heavily on the sharpness of the tip, the sensitivity of the detector to detect tip torsion, the precision of the scanner, and

the inertness of the tip material to the scanning environment, advances in microfabrication, electronics, and nanomaterial preparation will no doubt bring the spatial mapping capability and the versatility of FFM to a new level of resolution, precision, and independence of scanning environment.

Resolution Issues

It has been mentioned previously that the fundamental event underlying the STM imaging process is the highly localized electron tunneling between the tip and the surface. Intuitively, STM tips must be atomically sharp in order to achieve an extreme localization in the tunneling current and therefore atomic scale spatial resolution. However the strong z-dependence in the tunneling current actually means that any atom on a tip that protrudes more than 0.05 nm beyond any of the other atoms at an asperity will function as a single-atom tip.[83] This situation means that any electrically conducting object which is terminated by a protruding atom will, in principle, be capable of resolving atoms on a flat surface. However, if there are topographic corrugations in the surface (e.g., steps, pores, cracks, pits, etc.), then the finite size and shape of the tip becomes important and the image becomes a convolution of both tip and surface geometries. Figure 5, for example, shows the consequences of the geometrical convolution of a tip of finite width with a corrugated surface. The existence of "forbidden" space, i.e., surface features inaccessible to the tip, leads to inaccurate representations in height/depth, surface roughness, and particles size.

While STM has produced molecular/atomic resolution images, questions have been raised about the mechanism for generation of atomic or molecular resolution images by

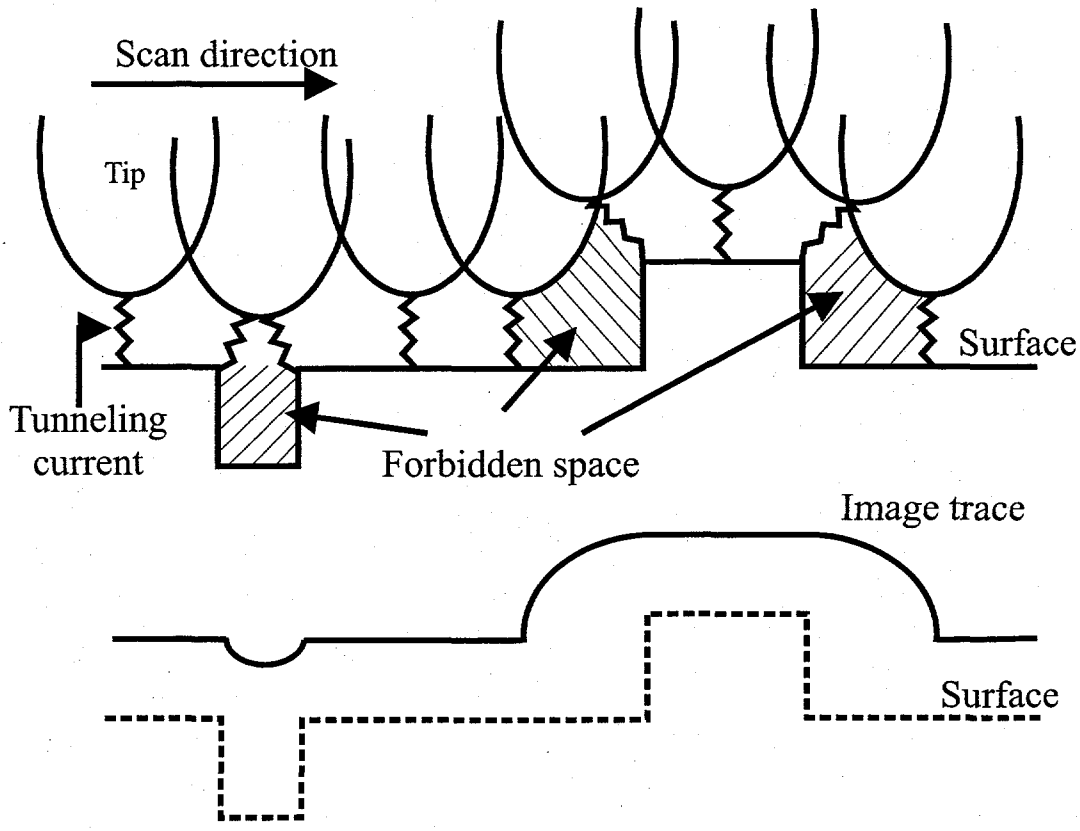

Figure 5. Schematic diagrams showing the geometrical convolution of a tip of finite width with a corrugated surface. Note the existence of "forbidden" space inaccessible to the tip, and the subsequent effect on the image.

SFM,[84,85] although in many cases, atomic or molecular resolution has been demonstrated.[86-91] The radius at the apex of a SFM probe tip microfabricated from silicon or silicon nitride is 5-10 nm at best. This situation translates into tens or even hundreds of molecules in forming contact between the tip and surface.[87] In addition, the contact area is highly dependent on F_N, especially for organic adlayers which are generally more compliant than inorganic materials. As a result, the SFM typically produces images with molecular periodicities, but not necessary molecular resolution, at surfaces with periodicity larger than the contact area. To achieve the highest possible resolution, one has to employ sharp probes, low loads, and relatively rigid films.

This concludes the general introduction into SPM, and some of these topics will be described again in more detail in later sections. At this point, the general introduction continues with an overview of spontaneously adsorbed monolayers, particularly organothiolate monolayers at gold. The use of these systems is particularly important not only because they form relatively stable, well ordered adlayers but they can also be characterized by a variety of techniques, as will soon become evident.

Spontaneously Adsorbed Monolayers

In recent years, the number of studies involving the application of spontaneously adsorbed organothiolate monolayers has grown drastically[3]. While most systems reported in the literature are formed by the adsorption of organothiols at gold from solutions, other noble metals such as silver,[92-100] copper,[94,101-103] and platinum[104-106] have been utilized, along with disulfide[107-114] and sulfide precursors[115-117]. The vast interest in this area can be

credited to Allara and Nuzzo,[107] and numerous other groups.[112,115,118-126] Various aspects of this field have been reviewed extensively by Whitesides and Laibinis,[127] Ulman,[3] Dubois and Nuzzo,[128] and Finklea.[129]

Gold is widely used over the other substrates because it is relatively inert to most common contaminants and resistant to air oxidation. In addition, the evaporation of thin gold film (100-300 nm) onto glass or fleshly-cleaved mica provides a convenient source of substrates which are relatively smooth at microscopic level. Moreover, subsequent annealing of Au/mica substrates after evaporation produces gold films with a predominant (111) surface crystallinity, large terraces (e.g., 100 nm x 100 nm) and low roughness (e.g., roughness factor of 1.10).[18,20,130-132]

An organothiolate monolayer is divided into three functional regions as shown by the idealized representation of a monolayer-liquid interface in Figure 6. The terminal group, located at the outmost few angstroms of the monolayer film, strongly affects interfacial properties. The terminal functional group can be varied to create a monolayer having specific interfacial properties (i.e., hydrophobic/hydrophilic, acidic/basic, etc.).[133-135] The chain/spacer region, most commonly comprised of alkyl chains or aromatic groups, dictates to a large degree the ordering, packing density and permeability of the monolayer. It is the cohesive interactions between the chains that directly affect the barrier properties of the film to electron transfer[118,129,135] and desorption.[130,136] Finally, the head group region, lying at the monolayer-substrate interface, includes all aspects of the sulfur-gold binding chemistry. The chemisorption of organothiols precursors at gold surfaces is driven by the formation of a gold-sulfur bond having a strength of 40~50 kcal/mol[3,129,137] which accounts to a large

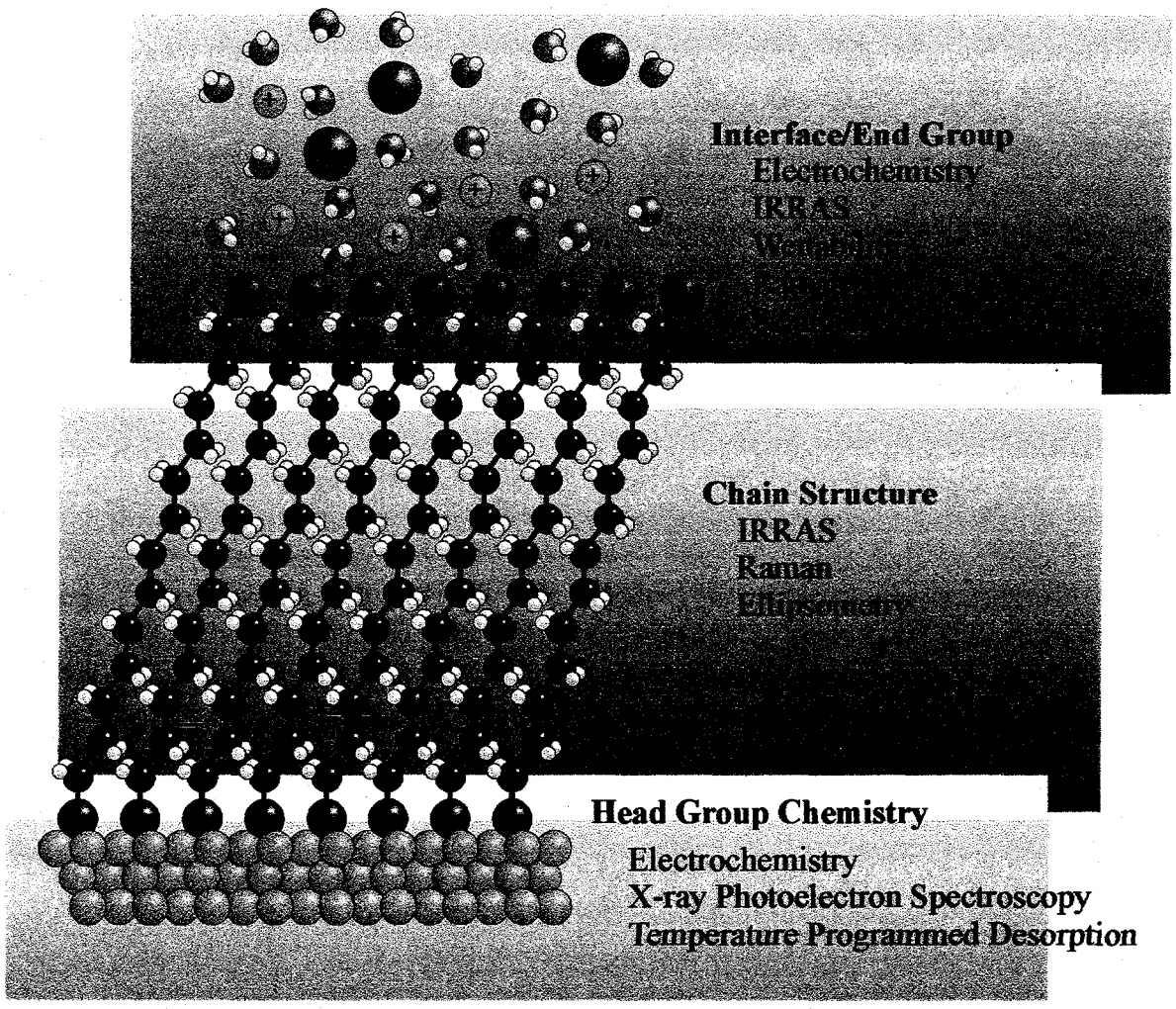

Figure 6. Idealized structure of alkanethiolate monolayer at Au(111) along with some key characterization techniques and the properties which they probe.

degree for the stabilization and robustness of these monolayers. The high affinity of gold and other metal towards sulfur adsorption allows a diverse range of functional groups to be incorporated into the monolayer. This fact, combined with the ease of synthesizing new organothiols and their use in studies of electron transfer events,[138] chemical sensors,[139-142] wetting,[3,115,122,124,128] and molecular architecture,[78,97,143] have led to a wide range of investigations with these systems.

When the three functional regions act together, interfaces with well-defined composition, thickness, and spatial arrangement can be created. In addition to the single component monolayer systems mentioned, the surface structure and interfacial properties can be tailored by changing the composition of the assembly solution (i.e., the combination of different precursors for the formation of a multi-component monolayer). The precursors could vary in the chain length or the chemical identity of the terminal group. The ability to incorporate several components in a monolayer[69,93,144-148] is crucial to the development of these films as two dimensional templates for the nanofabrication of molecular devices and microelectrodes, creation of molecular sensors, and advances in electroanalysis and electrocatalysis.

As mentioned, another reason that organothiol monolayers are so widely studied is the large number of analytical techniques available to interrogate different aspects of each functional region. Figure 6 illustrates an idealized picture of the three regions for alkanethiolate monolayers chemisorbed on gold, along with some characterization techniques that can be used to obtain a wealth of information regarding their structure and composition, which has a direct impact on their overall chemical and physical properties. For example,

infrared reflection absorption spectroscopy (IRRAS) probes the orientation of the methylene chain and terminal functional group due to the surface selection rules operative on conductive substrates. The methylene chains of alkanethiols adsorbed at gold typically exist in extended, all-trans configuration sequences that are tilted at ~30° from the surface normal.[118] Aromatic organothiols, on the other hand, extend more normal to the surface [100,149-151]. IRRAS has also been used extensively to assess the monolayer's packing density (liquid- vs. solid-like)[152] or local environment (protonated vs. deprotonated)[153] (order or disorder).[154,155] With such versatility, IRRAS is regarded as one of the most valuable techniques in the investigation of monolayer systems.

Contact angle measurements, using a goniometer, probe surface free energy, as well as interfacial free energies with respect to probe liquids like water and hexadecane.[108,115,122,125,127,133,134] Contact angles have a demonstrated depth sensitivity of ~0.5 nm,[125] a value that suggests its ability to be used to study the structure (e.g., orientation) and chemical identity of the terminal groups. For example, contact angle measurements have been used to characterize the acid/base properties of surface-immobilized molecular species, including their effective pK_a.[134,156,157]

All three regions of monolayers have been characterized by X-ray photoelectron spectroscopy (XPS). It provides information on the elemental composition of the surface, the nature of the head group, the binding chemistry between the adlayer and the substrate, and the coverage. The location of the $S(2p_{1/2})$ and $S(2p_{3/2})$ couplet at ~161.9 and ~163.2 eV for both thiol- and disulfide-derived monolayers on gold indicates that these precursors are adsorbed as thiolates.

Monolayers have also been studied extensively by various electrochemical techniques[129] such as capacitance measurements,[118,130,158] electrochemical reductive desorption,[130,136,159-165] underpotential deposition, and cyclic voltammetry of electroactive species present in solution.[138,144,160,166-168] Taken together, these techniques provide information about substrate roughness, adlayer coverage, gold-sulfur bond strength, chain-chain interactions, and electron barrier properties. Of particular importance to the studies reported in this dissertation is the technique of electrochemical reductive desorption and oxidation redeposition of the adsorbates in strong base. Previous work from our group has shown that organothiolate monolayers are desorbed from the electrode surface in alkaline electrolytic solutions by the application of a sufficiently negative potential.[116,130,131,136,159,160,162,169] The potential for the reductive desorption of thiolates was found to be dependent on surface morphology.[131,162] We also determined that the potential for the desorption was a function of the length of the alkyl chain.[130,136] In addition, the surface coverage of thiolate monolayers adsorbed at gold can be found from the charge for reductive desorption, calculated from a cyclic voltammetric scan by integrating the area under the cathodic wave, and the electron stoichiometry of the desorption reaction assuming a one-electron process.[130,159,160] After accounting for the surface roughness and estimating the net capacitive charge, the coverage of 8.4×10^{-10} mol/cm^2 [130] and 6.4×10^{-10} mol/cm^2.[170] were calculated for alkanethiolate and aromatic thiolate (4-mercaptobenzoic acid) monolayers, respectively.

SPM has also been applied extensively to the study of organothiolates adsorbed at gold. Both STM and SFM can generate images with molecular resolution of thiolates on

Au(111) terraces, yielding images of spots with hexagonal symmetry and spacing consistent with the $(\sqrt{3} \times \sqrt{3})$ R30° structure which is also demonstrated by electron diffraction[122] and low temperature helium diffraction[135,171] experiments. Although the actual site of the adsorbed thiolate on the gold lattice has not been determined, theoretical calculations indicate that alkanethiolates reside in the three-fold hollow sites.[95]

Microcontact Printing

Although the solution deposition of thiols on gold or silver is a common method of preparing single-component monolayers, microcontact printing[63,76,78,79,143,172-175] has become a popular technique to use when a patterned monolayer surface is needed. The methodology is attractive because of the relative ease of stamp preparation and the close correspondence of the features of the stamp to those of the master made from lithographic fabrication. This method employs an exposed and developed photoresist pattern on a silicon wafer as a master. A custom-made polymer "stamp", prepared from polymerized polydimethylsiloxane (PDMS) on the master, is then used to deposit precursor molecules onto localized area of a surface determined by the pattern on the "stamp". Figure 7 shows the microcontact printing process and a surface constructed by exposing a PDMS stamp to an ethanolic organothiol solution (1-10 mM) followed by drying under nitrogen and applying to a metal surface, generally gold or silver. Upon contact, the thiol is transferred to the gold surface, creating a monolayer only in the regions of contact with a pattern determined by the shape and size of the stamp. If desired, the uncoated portion of the gold surface can be either back-filled with another thiol by immersion[76,143] or "doubled-stamped"[76] by another PDMS

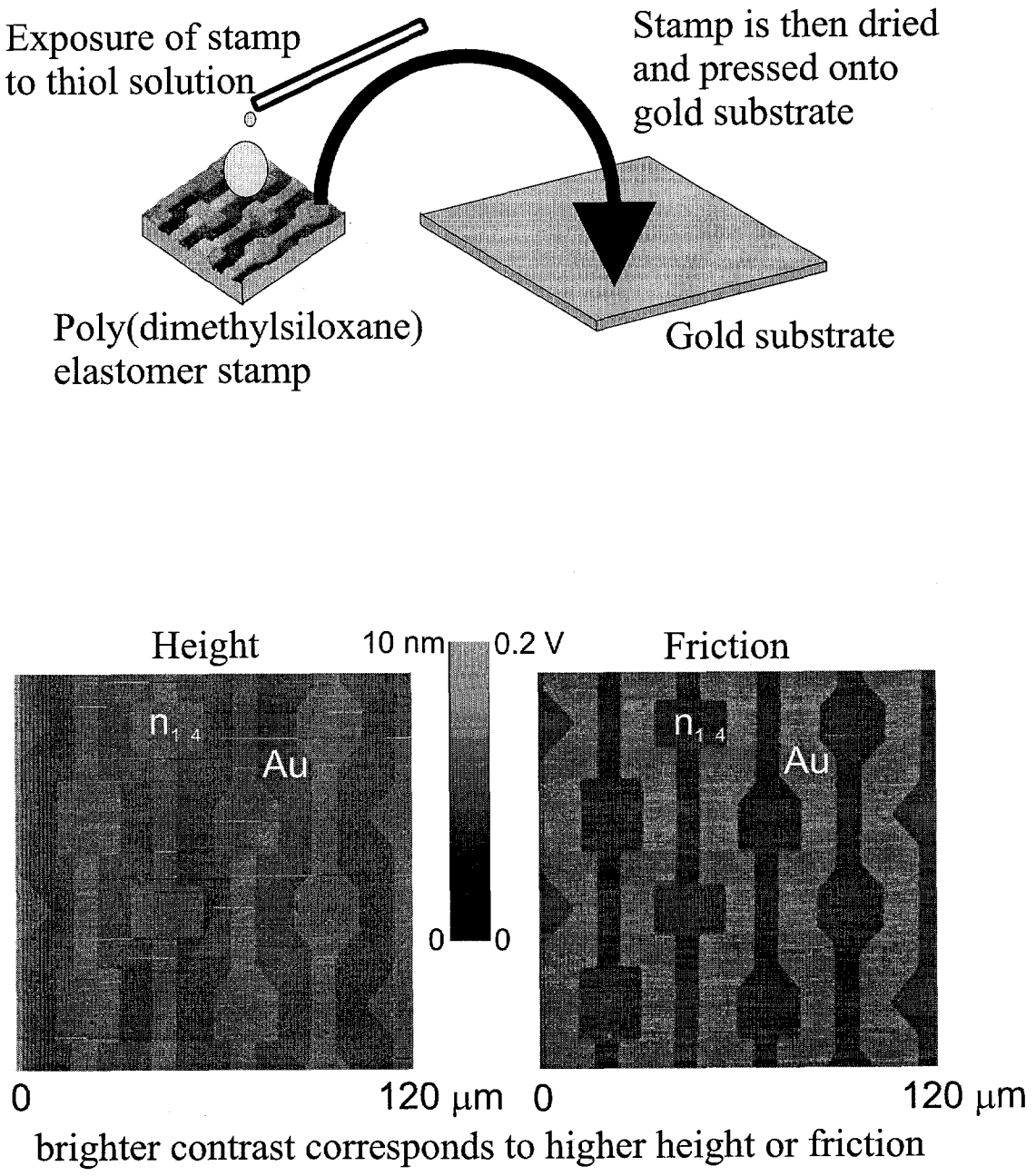

Figure 7. Top: Formation of patterned monolayer by microcontact printing. Bottom: SFM images (120 μm x 120 μm) of pentadecanethiolate monolayer microcontact printed on gold.

stamp with another thiol. Although the mechanism of adsorption and the quality of the monolayers formed from microcontact printing have not been investigated extensively,[175,176] one report[175] has suggested that the monolayer quality is comparable to those formed by solution deposition.

Dissertation Organization

The body of this dissertation is divided into four chapters following the general introduction. Each chapter is presented as a separate manuscript. Chapter 1 examines the surface reconstruction of as-evaporated gold during the formation of spontaneously adsorbed monolayers. Electrochemical reductive desorption, STM and GFAAS were used to probe the possibility of gold step sites evolving into terrace sites, resulting in a smoother surface. My contribution to this chapter includes the results from electrochemical reductive desorption of methyl-terminated alkanethiolates chemisorbed at gold, the GFAAS measurements on gold dissolution, the STM imaging of the various gold substrates, and a majority of the writing. Chapter 2 investigates the origin of the multiple voltammetric desorption waves of long chain alkanethiolate monolayers chemisorbed at annealed gold electrodes. Chapter 3 describes the multi-technique characterizations of mixed monolayers formed from spontaneously adsorbed organothiolates assemblies at Au(111) surface. The study provides insight into the factors important for controlling the spatial distribution of different organothiolate species on the surfaces. Chapter 4 demonstrates the mapping of orientation differences of terminal functional groups by friction force microscopy. Following these chapters is the final section that provides some general conclusions and a prospectus for future studies.

References

(1) Mallouk, T. E.; Harrison, D. J. *ACS Symposium Series 561: Interfacial Design and Chemical Sensing*; American Chemical Society: Washington, DC, 1994.

(2) Israelachvili, J. N. *Intermolecular and Surface Forces: With Applications to Colloidal and Biological Systems*; Academic Press: San Diego, CA, 1985.

(3) Ulman, A. *An Introduction to Ultrathin Organic Films: From Langmuir-Blodgett to Self-Assembly*; Academic Press: San Diego, 1991.

(4) Winograd, N. *Anal. Chem.* **1993**, *65*, 622A.

(5) Benninghoven, A.; Hagenhoff, B.; Niehuis, E. *Anal. Chem.* **1993**, *65*, 630A.

(6) Tarlov, M. J.; Newman, J. G. *Langmuir* **1992**, *8*, 1398.

(7) Lopez, G. P.; Biebuyck, H. A.; Whitesides, G. M. *Langmuir* **1993**, *9*, 1513.

(8) Wollman, E. W.; Frisbie, C. D.; Wrighton, M. S. *Langmuir* **1993**, *9*, 1517.

(9) Katon, J. E.; Sommer, A. J. *Anal. Chem.* **1992**, *64*, 931A.

(10) Katon, J. E. *Micron* **1996**, *27*, 303.

(11) Sahlin, J. J.; Peppas, N. S. *J. Appl. Polym. Sci.* **1997**, *63*, 103.

(12) Hubbard, A. T. *The Handbook of Surface Imaging and Visualization*; CRC Press: New York, 1995.

(13) Binnig, G.; Rohrer, H. *Helv. Phys. Acta* **1982**, *55*, 726.

(14) Binnig, G.; Rohrer, H.; Gerber, C.; Weibel, E. *Appl. Phys. Lett.* **1982**, *40*, 178.

(15) Binnig, G.; Quate, C. F.; Gerber, C. *Phys. Rev. Lett.* **1986**, *56*, 930.

(16) Binnig, G.; Fuchs, H.; Gerber, C.; Rohrer, H.; Stoll, E.; Tosatti, E. *Europhys. Lett.* **1986**, *1*, 31.

(17) Park, S. I.; Quate, C. F. *Appl. Phys. Lett.* **1986**, *48*, 112.

(18) Hallmark, V. N.; Chiang, S.; Rabolt, J. F.; Swalen, J. D.; Wilson, R. J. *Phys. Rev. Lett.* **1987**, *59*, 2879.

(19) Ohtani, H.; Wilson, R. J.; Chiang, S.; Mate, C. M. *Phys. Rev. Lett.* **1988**, *60*, 2398.

(20) Widrig, C. A.; Alves, C. A.; Porter, M. D. *J. Am. Chem. Soc.* **1991**, *113*, 2805.

(21) Poirier, G. E. *Chem. Rev.* **1997**, *97*, 1117.

(22) Clemmer, C. R.; T.P. Beebe, Jr. *Science* **1991**, *251*, 640.

(23) Weisenhorn, A. L.; Gaub, H. E.; Hansma, H. G.; Sinsheimer, R. L.; Kelderman, G. L.; Hansma, P. K. *Scanning Microsc.* **1990**, *4*, 511.

(24) Hansma, H. G.; Sinsheimer, R. L.; Gould, S. A. C.; Weisenhorn, A. L.; Gaub, H. E.; Hansma, P. K. AIP Conference Proceedings, Santa Barbara, CA, 1991.

(25) Hansma, H. G.; Vesenka, J.; Siegerist, C.; Kelderman, G.; Morrett, H.; Sinsheimer, R. L.; Elings, V.; Bustamante, C.; Hansma, P. K. *Science* **1992**, *256*, 1180.

(26) Bonnell, D. A. In *Scanning Tunneling Microscopy and Spectroscopy: Theory, Techniques, and Applications*; Bonnell, D. A., Ed.; VCH: New York, N. Y., 1993.

(27) Young, R.; Ward, J.; Scire, F. *Rev. Sci. Instrument* **1972**, *43*, 999.

(28) Teague, E. C.; Scire, F. E.; Bacher, S. M.; Jensen, S. W. *Wear* **1982**, *83*, 1.

(29) Wiesendanger, R.; Guentherodt, H.-J.; Editors. *Scanning Tunneling Microscopy III. Theory of STM and Related Scanning Probe Methods.*; Springer, Berlin, Germany, 1996.

(30) Wiesendanger, R.; Guentherodt, H. J.; Editors. *Scanning Tunneling Microscopy II: Further Applications and Related Scanning Techniques.*; Springer, Berlin, Germany, 1992.

(31) Guentherodt, H.-J.; Wiesendanger, R.; Editors. *Scanning Tunneling Microscopy I: General Principles and Applications to Clean and Absorbate-Covered Surfaces*; Springer, Berlin, Germany, 1994.

(32) Chen, C. J. *Introduction to Scanning Tunneling Microscopy*; Oxford Univ. Press, New York, 1993.

(33) Burnham, N. A.; Colton, R. J. In *Scanning Tunneling Microscopy and Spectroscopy: Theory, Techniques, and Applications*; Bonnell, D. A., Ed.; VCH: New York, NY, 1993.

(34) Rohrer, H. *Surf. Sci.* **1994**, *299-300*, 956.

(35) Hamers, R. J. *J. Phys. Chem.* **1996**, *100*, 13103.

(36) Delamarche, E.; Michel, B.; Biebuyck, H. A.; Gerber, C. *Adv. Mater.* **1996**, *8*, 719.

(37) Magonov, S. N.; Whangbo, M. H.; Editors. *Surface Analysis with STM and AFM: Experimental and Theoretical Aspects of Image Analysis.*; VCH, Weinheim, Germany, 1995.

(38) Hansma, P. K.; Tersoff, J. *J. Appl. Phys.* **1987**, *61*, R1.

(39) Tersoff, J.; Hamann, D. R. *Phys. Rev. B: Condens. Matter* **1985**, *31*, 805.

(40) *Procedures in Scanning Probe Microscopies*; Colton, R. J.; Engel, A.; Frommer, J. E.; Gaub, H. E.; Gewirth, A. A.; Guckenberger, R.; Rabe, J.; Heckl, W. M.; Parkinson, B., Eds.; John Wiley & Sons, Inc.: New York, 1998.

(41) Bhushan, B. In *Handbook of Micro/Nano Tribology*; Bhushan, B., Ed.; CRC: Boca Raton, FL, 1995.

(42) Frommer, J. E. *Thin Solid Films* **1996**, *273*, 112.

(43) Carpick, R. W.; Salmeron, M. *Chem. Rev.* **1997**, *97*, 1163.

(44) Bottomley, L. A. *Anal. Chem.* **1998**, *70*, 425R.

(45) Neubauer, G.; Cohen, S. R.; McClelland, G. M.; Horne, D.; Mate, C. M. *Rev. Sci. Instrum.* **1990**, *61*, 2296.

(46) Schoenenberger, C.; Alvarado, S. F. *Rev. Sci. Instrum.* **1989**, *60*, 3131.

(47) Meyer, G.; Amer, N. M. *Appl. Phys. Lett.* **1988**, *53*, 1045.

(48) Radmacher, M.; Tillmann, R. W.; Fritz, M.; Gaub, H. E. *Science* **1992**, *257*, 1900.

(49) Salmeron, M. *MRS Bull.* **1993**, *18*, 20.

(50) Zhong, Q.; Inniss, D.; Kjoller, K.; Elings, V. B. *Surf. Sci.* **1993**, *290*, L688.

(51) Martin, Y.; Abraham, D. W.; Wickramasinghe, H. K. *Appl. Phys. Lett.* **1988**, *52*, 1103.

(52) Hu, J.; Xiao, X.-D.; Ogletree, D. F.; Salmeron, M. *Science* **1995**, *268*, 267.

(53) Thomas, R. C.; Tangyunyong, P.; Houston, J. E.; Michalske, T. A.; Crooks, R. M. *J. Phys. Chem.* **1994**, *98*, 4493.

(54) Saenz, J. J.; Garcia, N.; Grutter, P.; Meyer, E.; Heinzelmann, H.; Wiesendanger, R.; Rosenthaler, L.; Hidber, H. R.; Guntherodt, H.-J. *J. Appl. Phys.* **1987**, *62*, 4293.

(55) Martin, Y.; Wickramasinghe, H. K. *Appl. Phys. Lett.* **1987**, *50*, 1455.

(56) Noy, A.; Vezenov, D. V.; Kayyem, J. F.; Meade, T. J.; Lieber, C. M. *Chem. Biol.* **1997**, *4*, 519.

(57) Mitsui, K.; Hara, M.; Ikai, A. *FEBS Lett.* **1996**, *385*, 29.

(58) Chen, X.; Davies, M. C.; Roberts, C. J.; Tendler, S. J. B.; Williams, P. M.; Davies, J.; Dawkes, A. C.; Edwards, J. C. *Langmuir* **1997**, *13*, 4106.

(59) Allen, S.; Chen, X.; Davies, J.; Davies, M. C.; Dawkes, A. C.; Edwards, J. C.; Roberts, C. J.; Sefton, J.; Tendler, S. J. B.; Williams, P. M. *Biochemistry* **1997**, *36*, 7457.

(60) McDermott, M. T.; Green, J.-B. D.; Porter, M. D. *Langmuir* **1997**, *13*, 2504.

(61) Graupe, M.; Koini, T.; Kim, H. I.; Garg, N.; Miura, Y. F.; Takenaga, M.; Perry, S. S.; Lee, T. R. *Colloids Surf., A* **1999**, *154*, 239.

(62) Ogletree, D. F.; Carpick, R. W.; Salmeron, M. *Rev. Sci. Instrum.* **1996**, *67*, 3298.

(63) Wong, S.-S.; Takano, H.; Porter, M. D. *Anal. Chem.* **1998**, *70*, 5209.

(64) Hayes, W. A.; Kim, H.; Yue, X.; Perry, S.; Shannon, C. *Langmuir* **1997**, *13*, *2511*.

(65) Lio, A.; Charych, D. H.; Salmeron, M. *J. Phy. Chem. B* **1997**, *101*, 3800.

(66) Green, J.-B. D.; McDermott, M. T.; Porter, M. D.; Siperko, L. M. *J. Phys. Chem.* **1995**, *99*, 10960.

(67) Koutso, V.; van der Vegte, E. W.; Grim, P. C. M.; Hadziioannou, G. *Macromolecule* **1998**, *31*, 116.

(68) Werts, M. P. L.; van der Vegte, E. W.; Grayer, V.; Esselink, E.; Tsitsilanis, C.; Hadziioannou, G. *Adv. Mater.* **1998**, *10*, 452.

(69) Kim, H. I.; Graupe, M.; Oloba, O.; Koini, T.; Imaduddin, S.; Lee, T. R.; Perry, S. S. *Langmuir* **1999**, *15*, 3179.

(70) Kendall, K. *Nature* **1986**, *319*, 203.

(71) Pollock, H. M. *Fundamentals of Friction: Macroscopic and Microscopic Processes*; Kluwer Academic Press: The Netherlands, 1992.

(72) Israelachvili, J. N. In *Handbook of Micro/Nanotribology*; Bhushan, B., Ed.; CRC Press: Boca Raton, FL, 1995.

(73) Overney, R. M.; Meyer, E.; Frommer, J.; Brodbeck, D.; Luthi, R.; Howald, L.; Guntherodt, H.-J.; Fujihira, M.; Takano, H.; Gotoh, Y. *Nature* **1992**, *359*, 133.

(74) Overney, R. M.; Meyer, E.; J., F.; Güntherodt, H.-J.; M., F.; Takano, H.; Gotoh, Y. *Langmuir* **1994**, *10*, 1281.

(75) Frisbie, C. D.; Rozsnyai, L. F.; Noy, A.; Wrighton, M. S.; Lieber, C. M. *Science* **1994**, *265*, 2071.

(76) Wilbur, J. L.; Biebuyck, H. A.; MacDonald, J. C.; Whitesides, G. M. *Langmuir* **1995**, *11*, 825.

(77) Vezenov, D. V.; Noy, A.; Lieber, C. M. In *Proceedings of the Scanning Probe Microscopy in Polymers Symposium*; American Chemical Society: Washington, D.C., 1998.

(78) Kumar, A.; Whitesides, G. M. *Appl. Phys. Lett.* **1993**, *63*, 2002.

(79) Werts, M. P. L.; van der Vegte, E. W.; Hadziioannou, G. *Langmuir* **1997**, *13*, 4939.

(80) Vezenov, D. V.; Noy, A.; Rozsnyai, L. F.; Lieber, C. M. *J. Am. Chem. Soc.* **1997**, *119*, 2006.

(81) van der Vegte, E. W.; Hadziioannou, G. *J. Phys. Chem. B.* **1997**, *101*, 9563.

(82) Wang, J.; Kenseth, J. R.; Jones, V. W.; Green, J.-B.; McDermott, M. T.; Porter, M. P. *J. Am. Chem. Soc.* **1997**, *119*, 12796.

(83) Myhrs, S. In *Handbook of Surface and Interface Analysis: Methods for Problem-Solving.*; Riviere, J. C., Myhra, S., Editors., Eds.; Dekker, New York, 1997.

(84) Burnham, N. A.; Colton, R. J.; Pollock, H. M. *J. Vac. Sci. Technol., A* **1991**, *9*, 2548.

(85) Binnig, G. *Ultramicroscopy* **1992**, *42-44*, 7.

(86) Giessibl, F. J. *Science* **1995**, *267*, 68.

(87) Ohnesorge, F.; Binnig, G. *Science* **1993**, *260*, 1451.

(88) Sugawara, Y.; Ueyama, H.; Uchihashi, T.; Ohta, M.; Yanase, Y.; Shigematsu, T.; Suzuki, M.; Morita, S. *Mater. Res. Soc. Symp. Proc.* **1997**, *442*, 15.

(89) Kitamura, S.; Suzuki, K.; Iwatsuki, M. *Jpn. J. Appl. Phys.* **1998**, *37*, 3765.

(90) Oden, P. I.; Tao, N. J.; Lindsay, S. M. *J. Vac. Sci. Technol. B* **1993**, *11*, 137.

(91) Xu, S.; Laibinis, P. E.; Liu, G.-Y. *J. Am. Chem. Soc.* **1998**, *120*, 9356.

(92) Chau, L.-K.; Porter, M. D. *Chem. Phys. Lett.* **1990**, *167*, 198.

(93) Laibinis, P. E.; Fox, M. A.; Folkers, J. P.; Whitesides, G. M. *Langmuir* **1991**, *7*, 3167.

(94) Laibinis, P. E.; Whitesides, G. M. *J. Am. Chem. Soc.* **1992**, *114*, 1990.

(95) Sellers, H.; Ulman, A.; Shnidman, Y.; Eilers, J. E. *J. Am. Chem. Soc.* **1993**, *115*, 9389.

(96) Smith, E. L.; Porter, M. D. *J. Phy. Chem.* **1993**, *97*, 8032.

(97) Tarlov, M. J.; Burgess, D. R. F., Jr; Gillen, G. *J. Am. Chem. Soc.* **1993**, *115*, 5305.

(98) Walczak, M. M.; Chung, C.; Stole, S. M.; Widrig, C. A.; Porter, M. D. *J. Am. Chem. Soc.* **1991**, *113*, 2370.

(99) Curtin, L. S.; Peck, S. R.; Tender, L. M.; Murray, R. W.; Rowe, G. K.; Creager, S. E. *Anal. Chem.* **1993**, *65*, 386.

(100) Osawa, M.; Matsuda, N.; Yoshii, K.; Uchida, I. *J. Phys. Chem.* **1994**, *98*, 12702.

(101) Laibinis, P. E.; Whitesides, G. M.; Allara, D. L.; Tao, Y.-T.; Parikh, A. N.; Nuzzo, R. G. *J. Am. Chem.* **1991**, *113*, 7152.

(102) Laibinis, P. E.; Whitesides, G. M. *J. Am. Chem. Soc.* **1992**, *114*, 9022.

(103) Ihs, A.; Liedberg, B. *J. Colloid Interface Sci.* **1991**, *144*, 282.

(104) Soriaga, M. P.; Hubbard, A. T. *J. Am. Chem. Soc.* **1982**, *104*, 3937.

(105) Vieira, K. L.; Zapien, D. C.; Soriaga, M. P.; Hubbard, A. T.; Low, K. P.; Adenson, S. E. *Anal. Chem.* **1986**, *1986*, 2964.

(106) Bravo, B. G.; Michelhaugh, S. L.; Soriaga, M. P. *J. Electroanal. Chem.* **1988**, *241*, 199.

(107) Nuzzo, R. G.; Allara, D. A. *J. Am. Chem. Soc.* **1983**, *105*, 4481.

(108) Biebuyck, H. A.; Whitesides, G. M. *Langmuir* **1993**, *9*, 1766.

(109) Castner, D. G.; Hinds, K.; Grainger, D. W. *Langmuir* **1996**, *12*, 5083.

(110) Hagenhoff, B.; Benninghoven, A.; Spinke, J.; Liley, M.; Knoll, W. *Langmuir* **1993**, *9*, 1622.

(111) He, Z.; Bhattacharyya, S.; Cleland Jr., W. E.; Hussey, C. L. *J. Electroanal. Chem.* **1995**, *397*, 305.

(112) Nuzzo, R. G.; Fusco, F. A.; Allara, D. L. *J. Am. Chem. Soc.* **1987**, *109*, 2358.

(113) Schonherr, H.; Ringsdorf, H. *Langmuir* **1996**, *12*, 3891.

(114) Ron, H.; Rubinstein, I. *J. Am. Chem. Soc.* **1998**, *120*, 13444.

(115) Troughton, E. B.; Bain, C. D.; Whitesides, G. M.; Nuzzo, R. G.; Allara, D. L.; Porter, M. D. *Langmuir* **1988**, *4*, 365.

(116) Zhong, C.-J.; Porter, M. D. *J. Am. Chem. Soc.* **1994**, *116*, 11616.

(117) Beulen, M. W. J.; Huisman, B.-H.; van der Heijden, P. A.; van Veggel, F. C. J. M.; Simons, M. G.; Biemond, E. M. E. F.; de Lange, P. J.; Reinhoudt, D. N. *Langmuir* **1996**, *12*, 6170.

(118) Porter, M. D.; Bright, T. B.; Allara, D. L.; Chidsey, C. E. D. *J. Am. Chem. Soc.* **1987**, *109*, 3559.

(119) Finklea, H. O.; Avery, S.; Lynch, M.; Furtsch, T. *Langmuir* **1987**, *3*, 409.

(120) Sabatani, E.; Rubinstein, I.; Maoz, R.; Sagiv, J. *J. Electroanal. Chem.* **1987**, *219*, 365.

(121) Sabatani, E.; Rubinstein, I. *J. Phys. Chem.* **1987**, *91*, 6663.

(122) Strong, L.; Whitesides, G. M. *Langmuir* **1988**, *4*, 546.

(123) Bain, C. D.; Whitesides, G. M. *J. Am. Chem. Soc.* **1988**, *110*, 6560.

(124) Bain, C. D.; Whitesides, G. M. *J. Am. Chem. Soc.* **1988**, *110*, 3665.

(125) Bain, C. D.; Whitesides, G. M. *J. Am. Chem. Soc.* **1988**, *110*, 5897.

(126) Bain, C. D.; Whitesides, G. M. *Science* **1988**, *240*, 62.

(127) Whitesides, G. M.; Laibinis, P. E. *Langmuir* **1990**, *6*, 87.

(128) Dubois, L. H.; Nuzzo, R. G. *Ann. Rev. Phys. Chem.* **1992**, *43*, 437.

(129) Finklea, H. O. In *Electroanal. Chem.*; Bard, A. J., Ed.; Marcel Dekker Inc.: New York:, 1996; Vol. 19.

(130) Widrig, C. A.; Chung, C.; Porter, M. D. *J. Electroanal. Chem.* **1991**, *310*, 335.

(131) Walczak, M. M.; Alves, C. A.; Lamp, B. D.; Porter, M. D. *J. Electroanal. Chem.* **1995**, *396*, 103.

(132) Chidsey, C. E. D.; Loiacono, D. N.; Sleator, T.; Nakahara, S. *Surf. Sci.* **1988**, *200*, 45.

(133) Bain, C. D.; Evall, J.; Whitesides, G. M. *J. Am. Chem. Soc.* **1989**, *111*, 7155.

(134) Bain, C. D.; Whitesides, G. M. *Langmuir* **1989**, *5*, 1370.

(135) Chidsey, C. E. D.; Loiacono, D. N. *Langmuir* **1990**, *6*, 682.

(136) Zhong, C.-J.; Porter, M. D. *J. Electroanal. Chem.* **1997**, *425*, 147.

(137) Nuzzo, R. G.; Zegarski, B. R.; Dubois, L. H. *J. Am. Chem. Soc.* **1987**, *109*, 733.

(138) Creager, S. E.; Rowe, G. K. *J. Electroanal. Chem.* **1994**, *370*, 203.

(139) Ricco, A. J.; Butler, M. A.; Vanysek, P.; Horvai, G.; Silva, A. F. Electrochem. Soc Conference Proceedings, Paris, France. 1997.

(140) Xiao, Y.; Ju, H.-X.; Chen, H.-Y. *Anal. Chim. Acta* **1999**, *391*, 73.

(141) Everhart, D. S. *CHEMTECH* **1999**, *29*, 30.

(142) Duan, C.; Meyerhoff, M. E. *Anal. Chem.* **1994**, *66*, 1369.

(143) Kumar, A.; Biebuyck, H. A.; Whitesides, G. M. *Langmuir* **1994**, *10*, 1498.

(144) Chidsey, C. E. D.; Bertozzi, C. R.; Putvinski, T. M.; Mujsce, A. M. *J. Am. Chem. Soc.* **1990**, *112*, 4301.

(145) Imabayashi, S.-I.; Hobara, D.; Kakiuchi, T.; Knoll, W. *Langmuir* **1997**, *13*, 4502.

(146) Sato, Y.; Mizutani, F. *Electroanalysis* **1998**, *10*, 633.

(147) Tokuhisa, H.; Zhao, M.; Baker, L. A.; Phan, V. T.; Dermody, D. L.; Garcia, M. E.; Peez, R. F.; Crooks, R. M.; Mayer, T. M. *J. Am. Chem. Soc.* **1998**, *120*, 4492.

(148) Cotton, C.; Glidle, A.; Beamson, G.; Cooper, J. M. *Langmuir* **1998**, *14*, 5139.

(149) Yang, H. C.; Dermody, D. L.; Xu, C.; Ricco, A. J.; Crooks, R. M. *Langmuir* **1996**, *12*, 726.

(150) Hayes, W. A.; Shannon, C. *Langmuir* **1996**, *12*, 3688.

(151) Zehner, R. W.; Hsung, R. P.; Sita, L. R. *ACS Symp. Ser.* **1999**, *727*, 169.

(152) Porter, M. D. *Anal. Chem.* **1988**, *60*, 1143A.

(153) Creager, S. E.; Steiger, C. M. *Langmuir* **1995**, *11*, 1852.

(154) Stole, S. M.; Porter, M. D. *Langmuir* **1990**, *6*, 1199.

(155) Laibinis, P. E.; Nuzzo, R. G.; Whitesides, G. M. *J. Phys. Chem.* **1992**, *96*, 5097.

(156) Lee, T. R.; Carey, R. I.; Biebuyck, H. A.; Whitesides, G. M. *Langmuir* **1994**, *10*, 741.

(157) Creager, S. E.; Clarke, J. *Langmuir* **1994**, *10*, 3675.

(158) Plant, A. L. *Langmuir* **1993**, *9*, 2764.

(159) Weisshaar, D. E.; Walczak, M. M.; Porter, M. D. *Langmuir* **1993**, *9*, 323.

(160) Walczak, M. M.; Popenoe, D. D.; Deinhammer, R. S.; Lamp, B. D.; Chung, C.; Porter, M. D. *Langmuir* **1991**, *7*, 2687.

(161) Zhong, C.-J.; Lamp, B. D.; Tani, N.; Porter, M. D. Book of Abstracts, 210th ACS National Meeting, Chicago, IL, August 20-24, 1995; 351.

(162) Zhong, C.-J.; Zak, J.; Porter, M. D. *J. Electroanal. Chem.* **1997**, *421*, 9.

(163) Schneider, T. W.; Buttry, D. A. *J. Am. Chem. Soc.* **1993**, *115*, 12391.

(164) Imabayashi, S.-I.; Iida, M.; Hobara, D.; Feng, Z. Q.; Niki, K.; Kakiuchi, T. *J. Electroanal. Chem.* **1997**, *428*, 33.

(165) Azehara, H.; Yoshimoto, S.; Hokari, H.; Akiba, U.; Taniguchi, I.; Fujihira, M. *J. Electroanal. Chem.* **1999**, *473*, 68.

(166) Creager, S. E.; Rowe, G. K. *J. Electroanal. Chem.* **1997**, *420*, 291.

(167) Chidsey, C. E. D.; Bertozzi, C. R.; Putvinski, T. M.; Mujsce, A. M.; Thorp, H. H. *Chemtracts: Inorg. Chem.* **1991**, *3*, 27.

(168) Popenoe, D. D.; Deinhammer, R. S.; Porter, M. D. *Langmuir* **1992**, *8*, 2521.

(169) Weisshaar, D. E.; Lamp, B. D.; Porter, M. D. *J. Am. Chem. Soc.* **1992**, *114*, 5860.

(170) Simmons, N. J. Ph.D. Thesis, Iowa State University, 1997.

(171) Chidsey, C. E. D.; Liu, G.-Y.; Rowntree, P.; Scoles, G. *J. Chem. Phys.* **1989**, *91*, 4421.

(172) Xia, Y.; Kim, E.; Zhao, X.-M.; Rogers, J. A.; Prentiss, M.; Whitesides, G. M. *Science* **1996**, *273*, 347.

(173) Xia, Y.; Whitesides, G. M. *Langmuir* **1997**, *13*, 2059.

(174) Xia, Y.; Venkateswaran, N.; Qin, D.; Tien, J.; Whitesides, G. M. *Langmuir* **1998**, *14*, 363.

(175) Larsen, N. B.; Biebuyck, H.; Delamarche, E.; Mitchel, B. *J. Am. Chem. Soc.* **1997**, *119*, 3017.

(176) Bar, G.; Rubin, S.; Parikh, A. N.; Swanson, B. I.; Zawodzinski, T. A., Jr.; Whangbo, M.-H. *Langmuir* **1997**, *13*, 373.

CHAPTER 1. GOLD SURFACE RECONSTRUCTION DURING THE FORMATION OF ORGANOTHIOLATE MONOLAYERS

A paper to be submitted to *Langmuir*

Chuan-Jian Zhong, Sze-Shun Wong, and Marc D. Porter

Abstract

Evidence for the surface reconstruction of the substrate during the formation of organothiolate monolayers at strongly (111) terraced gold is presented. Results based on electrochemical reductive desorption, infrared reflection absorption spectroscopy (IRRAS), graphite furnace atomic absorption spectroscopy (GFAAS), and scanning tunneling microscopy (STM) provide both macroscopic and microscopic insights into the information on the structural evolution of the gold surface during adlayer formation. Surface reconstruction is revealed by electrochemical reductive desorption studies, which suggest that at sub-monolayer coverage, thiolates preferentially adsorb at step sites. With the formation of gold-thiolate bonds, the gold-gold interaction weakens and gold atoms at step sites can evolve into terrace sites, making the surface smoother at a local level. Supporting evidence is provided by GFAAS measurement of gold dissolution from the substrate and by STM characterization of the surface morphology. The reconstruction is concluded to be a cooperative process induced by thiolate binding to gold, in which the structural interactions among chains and end groups contributes energetically to the substrate reconstruction. How these cooperative processes relate to surface diffusion and thermodynamic driving forces are

discussed.

Introduction

In recent years, several intensive studies have focused on characterizations of structure and properties of spontaneously adsorbed organothiolate monolayers at metal surfaces such as gold and silver.[1-5] This interest is largely because their well-ordered, close-packed nature provides opportunities for creating model interfaces. Less attention, however, has been paid to the dynamic nature of the substrate surface involving metal-thiolate and thiolate-thiolate interactions[6-19]. This aspect is important for both the fundamental understanding and the control of interfacial structures and therefore their potential applications in electronic[20,21], biosensing[22] and chemical sensing devices[23-27].

In addition to the traditional methods like contact angle measurements[2,28-33] and ellipsometry [8,14,34-40], many surface characterization techniques (e.g., scanning probe microscopies[41], vibrational spectroscopies[14,19,42-44], diffraction methods) have been employed to unravel the molecular level details of this class of interfacial structures. Bain et al.[8] have used ellipsometric measurements of thickness to show that the spontaneous adsorption of alkanethiols on Au involves an initial fast adsorption followed by a slow ordering of the film. Woell et al.[45] suggested that the slower process after initial adsorption reflected an ordering process of the alkyl chains, as demonstrated by the narrowing of the X-ray diffraction (XRD) peaks as the formation of the monolayer progressed. Recently, the kinetics of monolayer formation from both the vapor[46,47] and liquid[48,49] phases have been

investigated. Further, the mechanism of organothiolate monolayers formation on gold has been studied by both scanning tunneling microscopy (STM)[46,50] and in-situ scanning force microscopy (SFM)[49,51].

Surface reconstruction is a well-known phenomenon that can be induced at many metal surfaces by an adsorbate[52-56]. Also, substrate roughness was found to play an important role in determining defects in the resulting monolayers[16,57]. Based on STM observation of pit movement, McCarley et al.[10] proposed that Au-S bonds are labile and Au surface atoms diffuse. Stranick et al.[7] also reported in a STM study that the steps at an alkanethiolate-coated Au surface undergo changes in shape and position as a function of time. Motion of substrate-adsorbate complexes was described by using a surface diffusion mechanism. Other complex processes, such as surface pit formation, have also attracted attention[15,58-63].

As an effort to understand the importance of various binding sites (e.g., step and terrace sites) on the formation of gold-bound thiolates, we have investigated correlation between the microscopic roughness and electrochemical reductive[34,64-68]. By comparing the electrochemical desorption characteristics from as-evaporated and subsequently thermally annealed Au films, different binding sites have been proposed and confirmed by other comparative techniques such as X-ray photoelectron spectroscopy[66,67]. Studies on different single crystal face substrates have most recently appeared in an effort to further insights into substrate effects[66]. Using low energy helium x-ray diffraction[19], others have found that the chemisorption of thiols on Au(110) removes the "missing row" reconstruction, and

differences in the ordering of alkyl chains were noticed on Au(111) and (100) by low energy electron diffraction and IRRAS spectroscopies[69].

To date, the dynamic nature of monolayer formation is recognized and related to a simple first-order Langmuir adsorption kinetics process[18,70,71] and the ordering of the structure[8,18,43,45,70,72], yet the structural details concerning the dynamic processes involving both monolayer and substrate have yet to be offered. In this paper, we report investigations of the monolayer formation processes through immersion time studies in order to understand the evolution of gold substrate surfaces during adlayer formation. The correlation of the substrate surface roughness and the extent of the evolution was examined by using as-evaporated mica-supported gold films (i.e., a more stepped morphology) and those subsequently annealed at higher temperatures (i.e., a more terraced morphology) as substrates [67]. We will first present substrate-sensitive electrochemical reductive desorption data, from which the changes in the sizes of desorption waves involving different binding sites are discussed. We will then describe the monolayer structure-sensitive infrared reflection absorption spectroscopy (IRRAS) data, from which we discuss the evolution of monolayer, packing and ordering. We also present graphite furnace atomic absorption spectroscopy (GFAAS) and STM data, which provide additional information on the mobility of surface gold atoms through the measurements of gold dissolution in the thiol solutions and surface morphology, respectively.

Experimental

Sample Preparation. Gold substrates were prepared by resistive evaporation of 300 nm of gold onto glass slides (Fisher Scientific) or fleshly cleaved mica (B & M Trading Inc.) at ambient temperatures, as previously described[34,67]. The deposition rate was ~0.3 nm/s. The pressure in the cryopumped Edwards E306A coating system during evaporation was less than 1 x 10^{-4} Pa. The glass slides were cleaned in hot chromic acid, rinsed with copious amounts of methanol, dried under a stream of nitrogen, and pre-coated with a 15 nm chromium film to enhance the adhesion of the gold film. These substrates are termed "as-evaporated" Au(111) films. Substrates subsequently annealed in a muffle furnace at 300°C for 3 hr represent the "annealed" Au(111) films.

Monolayer Film Preparation. Ethanol (Quantum, punctilious grade), mercaptopropionoic acid (MPA) (Aldrich), hexadecanethiol (HDT) (Aldrich), and ethanethiol (ET) (Aldrich) were used as received. Mercaptohexadecanoic acid (MHA) and mercaptoundecanoic acid (MUA) were synthesized as described in the literature[8]. Monolayers were prepared by immersing the gold substrates into ethanolic thiol solutions. In most cases, concentrations ranged between 0.01 mM to 0.05 mM. After removal from solution, samples were rinsed with copious amounts of ethanol and dried under a stream of N_2.

Infrared Reflection Adsorption Spectroscopy (IRRAS). IRRAS spectra were acquired with a Nicolet MAGNA 750 FT-IR spectrometer using a liquid nitrogen-cooled mercury cadmium telluride detector. Reflectance spectra were collected with

p-polarized light incident at 80° with respect to the surface normal. All spectra were recorded with 2-cm^{-1} resolution and are the average of 512 sample and reference scans. Monolayer spectra are reported as -log(R/R_0), where R is the reflectance of the sample and R_0 is the reflectance of a octadecanethiolate-d_{37} monolayer on Au. Details of this instrumental set-up are given elsewhere[36].

Electrochemical Measurements. Electrodes were mounted in a conventional three-electrode cell with an exposed geometric area, defined by an O-ring, of 0.58 cm^2. All potential measurements are reported with respect to a Ag/AgCl /saturated KCl electrode. Deionized water, which was purified by passage through a Milli-Q filtration system, was used for all solution preparations. Electrolyte solutions were prepared with semiconductor grade KOH (99.99%, Aldrich) and were deoxygenated with argon. Voltammetric reductive desorption experiments were performed by scanning the applied potential at 50 mV/s between -0.00 and -1.35V using a CV-27 potentiostat (Bioanalytical Systems). These experiments were conducted within 5 min after removal of the sample from the assembly solution in order to minimize any time-dependent changes in the samples.

Graphite Furnace Atomic Absorption Spectroscopy (GFAAS). The amount of gold present in the different thiol solutions after monolayer formation was quantitatively determined by a Perkin Elmer 5000 graphite furnace atomic absorption spectrometer. The temperatures for pretreatment, atomization, and cleaning were 600°C, 1600°C, and 2700°C, respectively. The results are average values after immersion of ten separate pieces of 3 x 1 in. Au/mica substrates immersed in a glass container containing 65 mL of an ethanolic thiol

solution. As-evaporated and Au/mica substrates annealed at different temperatures (100°C and 300°C) for 5 hr were used to investigate the effect of substrate topography on gold dissolution. Control experiments were carried out with an "as prepared" thiol solution and with gold substrates immersed into neat ethanol.

Scanning Tunneling Microscopy (STM). STM images were obtained under ambient conditions using a Digital Instruments multimode microscope interfaced with a Nanoscope III controller. The instrument was equipment with a 0.7 μm scanner. The height mode, which maintains a constant current between tip and sample, was utilized for all imaging. The probe tips were fabricated by electrochemical etching a 0.025 cm diameter tungsten wire in 0.5M KOH (99.99%, Aldrich). The typical range of bias potential and set point current used for imaging were 500-1000 mV and 500-1000 pA, respectively, with the sign of the bias voltage given with respect to the grounded substrate. To minimize variations in the roughness assessment because of differences in the size and shape of tips, a single STM tip was used to collect all of the images in each set of experiments.

Results and Discussion

The electrochemical reductive desorption of spontaneously adsorbed gold-bound thiolates from thiol precursors in alkaline solutions can be effectively described by Equation (1)[34,64-66,73-77]

$$RS\text{-}Au + e^- \rightarrow Au + {}^-SR \qquad (1)$$

One of the particular intriguing observations from some of these electrochemical reductive

desorption investigations for short chain length systems ($N_c < 11$) is the difference in characteristics of the voltammetric desorption waves between as-evaporated Au(111) films and annealed Au(111)[67]. At annealed Au(111) films, the voltammetric curves display one dominant desorption wave, whereas at least one additional wave 200-300 mV more negative were detected at as-evaporated Au(111) films[67]. Based on comparisons of microscopic roughness, we proposed that the origin of the substrate dependence reflects differences in both the type and surface concentration of binding sites present at the two different surfaces[67]. That is, as-evaporated Au(111) films have a "rolling hill" surface topography with higher step density; however, annealed Au(111) films are composed of large (>150 nm) atomically flat (111)-terraces with a much lower step density. Therefore, the reductive desorption for the annealed Au(111) films reflects the presence of alkanethiolates bound primarily at the terrace sites of a more homogeneous Au(111) surface and that for the as-evaporated Au(111) films results from the presence of alkanethiolates bound at both the terrace and step sites of a more heterogeneous Au(111) surface.

This assertion is supported by a comparative study of the reductive desorption characteristics of alkanethiolate monolayers at single crystal Au(111) and Au(110) electrodes[66]. The positions of the dominant waves for the desorption of thiolates at the Au(111) and Au(110) single crystals are qualitatively comparable to those observed in the curves for same adlayer at the annealed Au(111) films and as-evaporated Au(111) films, respectively. This result confirmed that the reductive desorption potential is dependent on the surface crystallinity and showed that the binding strength of the gold-sulfur interaction is

larger at the Au(110) than at the Au(111) single crystal[66].

In this study, we report the immersion time-dependence of voltammetric curves from the reductive desorption of monolayers. The results will not only provide further support for the difference in binding sites, but also give new evidence suggesting that the gold atoms at step sites are more mobile than that at the terrace sites. As a result, the step sites can evolve into terrace sites during monolayer formation due to the molecular interactions in the monolayers and increased gold mobility due to the strong Au-S bonding and the concomitant decrease in the strength of Au-Au bonding.

Voltammetric Characteristics as a Function of Immersion Time. A typical set of voltammetric curves for the reductive desorption of MHA from as-evaporated Au/glass as a function of immersion time in a 0.06 mM ethanolic precursor solution is presented in Figure 1. The reductive desorption potentials (E_p, V) and integrated charges (Q_d, $\mu C/cm^2$) under each wave after deconvolution, and the total integrated charges of the waves (Q_t, $\mu C/cm^2$) are summarized in Table 1.

As expected, Table 1 shows that the total coverage (Q_t) in general, increases with immersion time. At an immersion time longer than 6 min, the thiolate surface coverage calculated from the averaged value of Q_t (75.0 ±2.5 $\mu C/cm^2$, if a roughness factor of 1.3 is used) according to Eq. (1) corresponds to a surface concentration of ~$7.8 \pm 2.6 \times 10^{-10}$ mole/cm^2; this value is in good agreement with the surface concentration expected for a ($\sqrt{3} \times \sqrt{3}$)$R30°$ adlayer on Au(111) (7.7×10^{-10} mole/cm^2).[30] For shorter immersion times, surface concentrations at submonolayer levels were obtained.

Apart from the general growth of reductive desorption waves as a function of time, detail examination of the voltammetric curves shows that the relative size of the waves change over time. The amount of thiolate at each type of binding site is therefore immersion-time dependent, as shown by a plot of the integrated charge under each wave vs. the immersion time in Figure 2. At very short immersion times (e.g., 0.03 min), the wave at ~-1.2 V (denoted hereafter as S wave) accounts for the majority of the reductive desorption charge. The wave located near ~-0.97 V (denoted hereafter as T wave), however, is very small. From 0.03 to 60 min, the charge under T wave ($Q_{d,T}$)increases progressively (from 12.9 to 40.6 $\mu C/cm^2$) while that under S wave ($Q_{d,S}$) has a significantly smaller increase (from 48.2 to 56.9 $\mu C/cm^2$). In addition, T wave shifts negatively by 60-70 mV, while S wave remains at about the same potential. Up to 60 min of immersion, $Q_{d,S}$ is still larger than $Q_{d,T}$. Beyond 60 min of immersion, $Q_{d,S}$ decreases while $Q_{d,T}$ continues to grow. At 120 min and longer, $Q_{d,T}$ becomes larger than $Q_{d,S}$. These changes are also accompanied by the movement of T wave from 0.97 to 1.05 ; there are no detectable changes in the position of S wave.

There are two possible explanations for the evolution of the desorption waves. The first possible explanation, though viewed as very unlikely, is that the solvent, in this case ethanol, triggers the evolution of step sites to terrace sites. The second explanation is that the evolution is induced as a consequence of adlayer formation. The former possibility was ruled out by immersing a set of as-evaporated Au/glass substrates into pure ethanol for 8 hr prior to placement into the ethanolic MHA solution. The voltammetric results effectively followed the same time evolution as shown in Figure 1. It is, therefore, evident that the adlayer

formation is responsible for the observed evolution of the voltammetric curves.

Having concluded that the monolayer formation triggers the observed evolution of the voltammetric data, we next focused on how the spontaneous adsorption process causes the evolution of the voltammetric curves. There are two likely possibilities: improvements in the packing/ordering of alkyl chains over time and changes in the ratio of terrace sites vs. step sites. The following sections examine each of the possibilities.

IRRAS Characterization as a Function of Immersion Time. The structure of the MHA monolayers during the formation from a 0.04 mM ethanolic solution was characterized by a time-dependent IRRAS study. The resulting spectra of the C-H stretching region (2700-3100 cm^{-1}) are presented in Figure 3. In the C-H stretching region, both $\nu_a(CH_2)$ (~2920 cm^{-1}) and $\nu_s(CH_2)$ (~2850 cm^{-1}) bands become narrower, lower in intensity and shift to lower frequency as immersion time increases. For example, a reproducible and consistent shift of ~8 cm^{-1} is evident (i.e., a decrease from 2926 to 2918 cm^{-1}) for at least five replica samples between immersion times of 1 min and 1000 min. These changes are indicative of an increase in the packing density and therefore ordering of the chain[14,69,78]. More importantly, the change with ~12 min of immersion accounts for most of the shift. Thus, the time-scale of the dominant changes in the IRRAS data is notably shorter than that observed for reductive desorption data.

If an enhanced packing/ordering could lead to observed evolution of the voltammetric curves, we would expect that the capacitance of the MHA monolayers during the immersion time study to be significantly different in order to account for the voltammetric

differences[16,34,78-81]. We measured the capacitance of the monolayers by calculating the charging currents at 0.0 V in cyclic voltammograms recorded in 0.5 M KOH at 100 mV/s. These measurements did not detect significant differences in capacitance during the time window that the evolution of voltammetric curves occurs. These results also argue against changes in chain packing as the origin of the evolution of the voltammetric curves.

The chain length effects on smoothing of gold. The evolution of the voltammetry for acid-terminated alkanethiolate monolayers on as-evaporated Au/glass with shorter chain lengths (i.e., MUA and MPA) were also examined. The results are shown in Figures 4 (MUA) and 5 (MPA). Comparison of the voltammetric curves shows that the waves of MPA evolve differently from those of the longer chain MHA and MUA. T wave for MPA is very narrow and is markedly larger than S wave at long immersion times. This difference suggests that chain length may play a role in the extent of the surface reconstruction. Further inspection of the voltammetric curves of MHA and MPA shows that T wave becomes dominant while S wave remains relatively small for all immersion times and that there is little of the cross-over observed for MHA in Figure 1.

Since the substrates for the three precursors are microscopically indistinguishable, one might expect that the voltammetric waves for all three adsorbates would be similar, at least at the early stages of the formation process. The results in Figures 1, 4, and 5 are contrary to this expectation. We therefore believe that the adsorbate-induced alteration of the substrate occurs at a much faster rate with the shorter chain MPA and MUA. More importantly, based on the voltammetric curves from long immersion times, T wave from MPA is much more dominant than those from MUA and MHA, suggesting that spontaneous adsorption of shorter

chain thiol leads to a faster and more significant evolution of binding sites.

The chain length effect on the evolution of step sites to terrace sites can also be observed with voltammetric reductive desorption of an alkanethiolate monolayer. Shown in Figure 6 are voltammetric curves from reductive desorption of hexadecanethiolate (top) and ethanethiolate monolayers (bottom) from as-evaporated Au/mica. The voltammetric curves for the same adlayers on annealed Au/mica are shown in Figure 6 for comparison. All electrodes were immersed for ~12 hr in their respective ethanolic thiol (1 mM) solution. With as-evaporated Au/mica as the substrate, the voltammetric waves show that both T and S waves are observable for ET. However, T wave for HDT is not observed and S wave overlaps with the current derived from solvent reduction.

Based on the relative size of T wave for the reductive desorption of the two adlayers, we suspect that the shorter length adsorbate preferentially "smoothes" the surface by transforming step sites to terrace. This assertion is consistent with our conclusion drawn from the data for the carboxylic acid-terminated alkanethiols. The extent of the evolution can be further dissected when the voltammetric waves from as-evaporated and annealed Au/mica are compared. In the case of HDT, little evolution occurs at the as-evaporated Au/mica as shown by the small size of the wave for desorption of such long chain thiolates at terrace sites. To the contrary, the waves for the desorption of ET from as-evaporated gold show a much larger wave from terrace sites, suggesting a significant evolution of step sites to terrace site.

Table 2 lists STM-determined roughness factors (RFs) of as-evaporated Au/mica and of the ET and HDT coated as-evaporated Au/mica. These experiments were conducted to

determine whether the evolution in surface morphology could be detected microscopically. While only subtly different, the lower RF for the ET covered surface indicates that adsorption of shorter chain alkanethiolates on as-evaporated Au/mica results in a slightly smoother surface.

The above chain length comparison suggests that the smoothing of the substrates by short chain thiols is closely linked to intermolecular interactions. The difference in cohesive interactions between alkyl chains is 1.6 to 3.3 kJ/mole per methylene group[82] and is evident in the structural insight gained in characterizing these systems with infrared[3] and Raman[42] spectroscopies, both of which indicate that long chain monolayers are more densely packed than short chain monolayers.

Since the above argues that intermolecular interactions may play a role in the extent of the observed smoothing, we next focused on developing a dynamic description of the process. Surface dynamics often arise from surface diffusion, and can affect both substrate and adsorbate structures[52-56]. The reported values of surface diffusion activation energy for gold range from 5.7 to 17 k cal/mole[83,84]. The activation energy of gold diffusion, however, is lower than the Au-S bond energy (~44 kcal/mol[85]). In other words, the migrating surface species is probably not an individual gold atom, but rather a gold thiolate complex (Au-SR). The possibility of a Au-thiolate complex being the mobile species is more likely if adsorption of thiolates weaken neighboring Au-Au bonds[83,86]. Reports have shown that Au-Au bonding is weakened by the formation of adsorbate-Au bonding (i.e., Cl and S[52,83]). Furthermore, the Au-thiolate species will be more mobile for the short chain thiolates where

intermolecular interactions are less. This conclusion is supported by the results of experiments in the next section which determined the amount of gold in the thiol solution after adsorption. At present, we are not able to estimate quantitatively how much the Au-Au bonds are weakened, but we believe that the barrier is lowered significantly by Au-SR bonding. This decrease, in turn, lowers the barrier to surface diffusion at steps, becoming accessible under ambient conditions.

Supporting Evidence from GFAAS and STM. To assess further the possibility of the above assertion, experiments were performed to illustrate the mobility of the surface gold in the presence of thiolates. The higher the mobility, the more likely that some of the surface gold will be able to leave the surface and become dissolved in the precursor solution. In addition, the surface morphology changes should be tractable using STM. The amount of gold in the thiol solution after adsorption[15,75,87] on Au/mica was determined with GFAAS, and the results are shown in Table 3. These results are for Au/mica substrates annealed at different temperatures for 3 hr and immersed in different ethanolic (1mM) solutions for 12 hr before characterization. The equivalent gold monolayer coverage was also calculated and is listed in Table 3. The goal of annealing the Au/mica at different temperatures is to prepare gold surfaces with different extend of roughness and terrace sizes (i.e., higher annealing temperature brings smoother gold surfaces microscopically). The effects of substrate morphology on the dissolution of gold in thiol solutions therefore can be studied. The control experiments show that there was no detectable gold in the precursor solutions before the immersion of gold or in neat ethanol; in the latter, as-evaporated Au/mica were immersed in ethanol for 12 hr. Comparing the amount of gold detected in solutions of HT and DT, at least

twice as much gold was lost from the substrates in the HT solutions. This trend suggests that gold atoms are more labile when complexed with shorter chain adsorbates and a more extensive evolution of step sites to terrace site would be expected. This perspective is supported by the voltammetric data in Figures 1, 3 and 4 which shows MPA yields a larger T wave at long immersion times than MUA and MHA. Based on the small amount (less than the equivalent of 2% of a monolayer in the case of HT on as-evaporated Au/mica) of Au determined in solution, it is unlikely that etching of gold can lead to such extent of evolution in the voltammetric curves. We believe that surface diffusion, rather than etching, is the main process that is responsible for the evolution.

The gold dissolution experiment also found higher gold concentrations in solutions with acid-terminated thiols (MUA) than in those with methyl-terminated thiols (DT), even though both have similar chain length. Since acid-terminated thiols are likely to be more soluble in ethanol than those with less polar methyl end group, we speculate that the dissolved gold is in the form of Au-SR and the solubility of the carboxylic acid end group enhances the mobility and dissolution. This proposal is supported by comparing the voltammetric curves from the reductive desorption of monolayers from acid-terminated and methyl-terminated thiolate having equal number of carbons in the chain. With the same substrates, curves from acid-terminated monolayers are characterized by a larger T wave and a much smaller S wave. In short, the extent of gold dissolution in ethanolic solutions reflects the enhanced mobility of gold on the surfaces arising from the formation of Au-SR bonds. The mobility of the Au-SR is, however, hindered by the cohesive interactions between the

alkyl chains but increased by the solubility of the Au-SR complex which is affected by the polarity of the terminal functional groups.

Table 3 also shows that amount of gold dissolved from as-evaporated Au/mica is consistently higher than that from annealed (smoother) Au/mica. The correlation that as-evaporated gold has more step sites and loses more gold during monolayer formation supports our claim that the gold atoms at step sites is more mobile after the formation of Au-SR bonds. Interestingly, this mobility can be correlated through differences in the metal-metal coordination numbers at terraces and steps as illustrated in Figure 7. On the terrace of a flat (111) face, the coordination number of the exposed atoms is 9. At a step between the terraces, the atoms have coordination numbers of 7 or 8. If the step is kinked, coordination numbers as low as of 5 or even 6 are possible. Thus, gold atoms at step sites are more mobile due to a lower number of neighboring atoms, consistent with our belief that gold atoms at step sites are mobile enough to reconstruct into terrace site and some of them were lost to the solutions.

The mobility of surface gold atoms in the present of thiolates is also manifested by STM topographic images showing the effects of annealing the as-evaporated Au/mica in the presence of an adlayer. Figure 8 are STM images (800 nm x 800 nm) of the sample surfaces after annealing the as-evaporated Au/mica without (Figure 8A) and with the HDT (Figure 8B) adlayer at 100°C for 12 hr. The difference in surface roughness clearly evident. The Au/mica annealed without the HDT adlayer resembles that of as-evaporated Au/mica which has a "rolling hill" morphology and small sized crystallites[67]. To the contrary, Au/mica coated with an HDT adlayer and annealed under the same conditions has a more terraced

morphology and larger crystallites. The surface roughness factors (RFs) for samples that received different treatments are determined from STM images of 800 nm x 800 nm and are listed in Table 4. By annealing HDT-coated as-evaporated Au/mica at 100°C for 12 hr, a RF of 1.10 is obtained. The RFs of uncoated Au/mica annealed under the same conditions and as-evaporated Au/mica are 1.13 and 1.14, respectively. The smoothing of the as-evaporated Au by annealing after the spontaneous adsorption of thiolates indicates that the Au-AuSR bond is comparatively weaker than the Au-Au.

Conclusions

In summary, we have presented evidence for the surface reconstruction of the substrate during the formation of organothiolate monolayer at as-evaporated gold. This evidence which is based on multi-techniques such as electrochemical reductive desorption, IRRAS, GFAAS, and STM has provided both macroscopic and microscopic information on the structural evolution of the surface. The evidence all points to the direction that at submonolayer coverage, thiolates preferentially occupy step sites. The formation of Au-SR bonds then weakens the bonds between neighboring gold atoms. This weakening of the surface gold atoms enhances the mobility of the Au-SR complexes, particularly at the low coordination boundary regions such as steps and kinks. As a result of such enhanced mobility, the Au-complexes move from the step sites to terrace sites, creating a smoother surface as suggested by the electrochemical reductive desorption data and confirmed by the STM images and subsequent roughness analysis. Our results suggest that the extend of smoothing can be increased by using substrates of higher roughness, organothiol precursor of

shorter chain or with more polar terminal group (e.g., carboxylic acid). Although we currently do not know the details of the Au-SR complex movements, we speculate that the movements required to achieve the evolution as indicated by the voltammetric reductive desorption curves are not extensive. To this end, in situ scanning probe microscopic experiments aimed at studying the substrate smoothing mechanism are underway.

Acknowledgements

We acknowledge Bob Hofer of the Analytical Services of the Ames laboratory Materials Preparation Center with the GFAAS measurements. This work was supported by the Office of Basic Energy Research, Chemical Sciences Division of the US Department of Energy. Ames Laboratory is operated for the US Department of Energy by Iowa State University under Contract No. W-7405-eng-82.

References

(1) Poirier, G. E. *Chem. Rev.* **1997**, *97*, 1117.

(2) Whitesides, G. M.; Laibinis, P. E. *Langmuir* **1990**, *6*, 87.

(3) Ulman, A. *An Introduction to Ultrathin Organic Films: From Langmuir-Blodgett to Self-Assembly*; Academic Press: San Diego, 1991.

(4) Dubois, L. H.; Nuzzo, R. G. *Ann. Rev. Phys. Chem.* **1992**, *43*, 437.

(5) Finklea, H. O. In *Electroanal. Chem.*; Bard, A. J., Ed.; Marcel Dekker Inc.: New York:, 1996; Vol. 19.

(6) Nuzzo, R. G.; Fusco, F. A.; Allara, D. L. *J. Am. Chem. Soc.* **1987**, *109*, 2358.

(7) Stranick, S. J.; Parikh, A. N.; Allara, D. L.; Weiss, P. S. *J. Phys. Chem.* **1994**, *98*, 11136.

(8) Bain, C. D.; Troughton, E. B.; Tao, Y.-T.; Evall, J.; Whitesides, G. M.; Nuzzo, R. G. *J. Am. chem. Soc.* **1989**, *111*, 321.

(9) Tirado, J. D.; Acevedo, D.; Bretz, R. L.; Abruna, H. D. *Langmuir* **1994**, *10*, 1971.

(10) McCarley, R. L.; Dunaway, D. J.; Willicut, R. J. *Langmuir* **1993**, *9*, 2775.

(11) McCarley, R. L.; Kim, Y.-T.; Bard, A. J. *J. Phys. Chem.* **1993**, *97*, 211.

(12) Zhong, C.-J.; Woods, N. T.; Dawson, G. B.; Porter, M. D. *Electrochem. Commun.* **1999**, *1*, 17.

(13) Stranick, S. J.; Parikh, A. N.; Tao, Y. T.; Allara, D. L.; Weiss, P. S. *J. Phys. Chem.* **1994**, *98*, 7636.

(14) Porter, M. D.; Bright, T. B.; Allara, D. L.; Chidsey, C. E. D. *J. Am. Chem. Soc.* **1987**, *109*, 3559.

(15) Edinger, K.; Goelzhaeuser, A.; Demota, K.; Woell, C.; Grunze, M. *Langmuir* **1993**, *9*, 4.

(16) Creager, S. E.; Hockett, L. A.; Rowe, G. K. *Langmuir* **1992**, *8*, 854.

(17) Buck, M.; Eisert, F.; Fischer, J.; Grunze, M.; Traeger, F. *Appl. Phys. A* **1991**, *A53*, 552.

(18) Buck, M.; Grunze, M.; Eisert, F.; Fischer, J.; Traeger, F. *J. Vac. Sci. Technol., A* **1992**, *10*, 926.

(19) Camillone, N., III; Chidsey, C. E. D.; Liu, G. Y.; Scoles, G. *J. Chem. Phys.* **1993**, *98*, 4234.

(20) Liu, Q.; Frutos, A. G.; Thiel, A. J.; Corn, R. M.; Smith, L. M. *J. Comput. Biol.* **1998**, *5*, 269.

(21) Smith, L. M.; Corn, R. M.; Condon, A. E.; Lagally, M. G.; Frutos, A. G.; Liu, Q.; Thiel, A. J. *J. Comput. Biol.* **1998**, *5*, 255.

(22) Frutos, A. G.; Thiel, A. J.; Condon, A. E.; Smith, L. M.; Corn, R. M. Book of Abstracts, 214th ACS National Meeting, Las Vegas, NV, September 7-11, 1997; p MTLS.

(23) Kepley, L. J.; Crooks, R. M.; Ricco, A. J. *Anal. Chem.* **1992**, *64*, 3191.

(24) Duan, C.; Meyerhoff, M. E. *Anal. Chem.* **1994**, *66*, 1369.

(25) Ricco, A. J.; Butler, M. A.; Vanysek, P.; Horvai, G.; Silva, A. F.; Editors. , 1997; p 1100.

(26) Xiao, Y.; Ju, H.-X.; Chen, H.-Y. *Anal. Chim. Acta* **1999**, *391*, 73.

(27) MacKay, S. G.; Bakir, M.; Musselman, I. H.; Meyer, T. J.; Linton, R. W. *Anal. Chem.* **1991**, *63*, 60.

(28) Troughton, E. B.; Bain, C. D.; Whitesides, G. M.; Nuzzo, R. G.; Allara, D. L.; Porter, M. D. *Langmuir* **1988**, *4*, 365.

(29) Bain, C. D.; Whitesides, G. M. *J. Am. Chem. Soc.* **1988**, *110*, 5897.

(30) Strong, L.; Whitesides, G. M. *Langmuir* **1988**, *4*, 546.

(31) Bain, C. D.; Whitesides, G. M. *Langmuir* **1989**, *5*, 1370.

(32) Bain, C. D.; Evall, J.; Whitesides, G. M. *J. Am. Chem. Soc.* **1989**, *111*, 7155.

(33) Biebuyck, H. A.; Whitesides, G. M. *Langmuir* **1993**, *9*, 1766.

(34) Widrig, C. A.; Chung, C.; Porter, M. D. *J. Electroanal. Chem.* **1991**, *310*, 335.

(35) Evans, S. D.; Urankar, E.; Ulman, A.; Ferris, N. *J. Am. Chem. Soc.* **1991**, *113*, 4121.

(36) Walczak, M. M.; Chung, C.; Stole, S. M.; Widrig, C. A.; Porter, M. D. *J. Am. Chem. Soc.* **1991**, *113*, 2370.

(37) Miller, C.; Cuendet, P.; Graetzel, M. *J. Phys. Chem.* **1991**, *95*, 877.

(38) Chau, L.-K.; Porter, M. D. *Chem. Phys. Lett.* **1990**, *167*, 198.

(39) Evans, S. D.; Ulman, A. *Chem. Phys. Lett.* **1990**, *170*, 462.

(40) Biebuyck, H. A.; Bain, C. D.; Whitesides, G. M. *Langmuir* **1994**, *10*, 1825.

(41) Wong, S.-S.; Takano, H.; Porter, M. D. *Anal. Chem.* **1998**, *70*, 5209.

(42) Bryant, M. A.; Pemberton, J. E. *J. Am. Chem. Soc.* **1991**, *113*, 8284.

(43) Chidsey, C. E. D.; Liu, G.-Y.; Rowntree, P.; Scoles, G. *J. Chem. Phys.* **1989**, *91*, 4421.

(44) Fenter, P.; Eisenberger, P.; Liang, K. S. *Phys. Rev. Lett.* **1993**, *70*, 2447.

(45) Haehner, G.; Woell, C.; Buck, M.; Grunze, M. *Langmuir* **1993**, *9*, 1955.

(46) Poirier, G. E.; Pylant, E. D. *Science* **1996**, *272*, 1145.

(47) Touzov, I.; Gorman, C. B. *Langmuir* **1997**, *13*, 4850.

(48) Tamada, K.; Hara, M.; Sasabe, H.; Knoll, W. *Langmuir* **1997**, *13*, 1558.

(49) Xu, S.; Laibinis, P. E.; Liu, G.-Y. *J. Am. Chem. Soc.* **1998**, *120*, 9356.

(50) Yamada, R.; Uosaki, K. *Langmuir* **1998**, *14*, 855.

(51) Xu, X.; Cruchon-Dupeyrat, S. J. N.; Garno, J. C.; Liu, G.-Y.; Jennings, G. K.; Yong, T.-H.; Laibinis, P. E. *J. Chem. Phys.* **1998**, *108*, 5002.

(52) Wiechers, J.; Twomey, T.; Kolb, D. M.; Behm, R. J. *J. Electroanal. Chem.* **1988**, *248*, 451.

(53) Chidsey, C. E. D.; Loiacono, D. N.; Sleator, T.; Nakahara, S. *Surf. Sci.* **1988**, *200*, 45.

(54) Gao, X.; Zhang, Y.; Weaver, M. J. *J. Phys. Chem.* **1992**, *96*, 4156.

(55) Alonso, C.; Salvarezza, R. C.; Vara, J. M.; Arvia, A. J. *Electrochim. Acta* **1990**, *35*, 1331.

(56) Zubimendi, J. L.; Vela, M. E.; Salvarezza, R. C.; Vazquez, L.; Vara, J. M.; Arvia, A. J. *Langmuir* **1996**, *12*, 12.

(57) Green, J.-B. D. , Ph.D Thesis, Iowa State University, Ames, 1996.

(58) McDermott, C. A.; McDermott, M. T.; Green, J.-B.; Porter, M. D. *J. Phys. Chem.* **1995**, *99*, 13257.

(59) Sondag-Huethorst, J. A. M.; Schonenberger, C.; Fokkink, L. G. J. *J. Phys. Chem.* **1994**, *98*, 6826.

(60) Kim, Y.-T.; Bard, A. J. *Langmuir* **1992**, *8*, 1096.

(61) Kim, Y. T.; McCarley, R. L.; Bard, A. J. *Langmuir* **1993**, *9*, 1941.

(62) Sun, L.; Crooks, R. M. *J. Electrochem. Soc.* **1991**, *138*, L23.

(63) Ross, C. B.; Sun, L.; Crooks, R. M. *Langmuir* **1993**, *9*, 632.

(64) Zhong, C.-J.; Porter, M. D. *J. Electroanal. Chem.* **1997**, *425*, 147.

(65) Zhong, C. J.; Lamp, B. D.; Tani, N.; Porter, M. D. Book of Abstracts, 210th ACS National Meeting, Chicago, IL, August 20-24, 1995.

(66) Zhong, C.-J.; Zak, J.; Porter, M. D. *J. Electroanal. Chem.* **1997**, *421*, 9.

(67) Walczak, M. M.; Alves, C. A.; Lamp, B. D.; Porter, M. D. *J. Electroanal. Chem.* **1995**, *396*, 103.

(68) Walczak, M. M.; Popenoe, D. D.; Deinhammer, R. S.; Lamp, B. D.; Chung, C.; Porter, M. D. *Langmuir* **1991**, *7*, 2687.

(69) Dubois, L. H.; Zegarski, B. R.; Nuzzo, R. G. *J. Chem. Phys.* **1993**, *98*, 678.

(70) Thomas, R. C.; Sun, L.; Crooks, R. M.; Ricco, A. J. *Langmuir* **1991**, *7*, 620.

(71) Karpovich, D. S.; Blanchard, G. J. *Langmuir* **1994**, *10*, 3315.

(72) Haehner, G.; Kinzler, M.; Thuemmler, C.; Woell, C.; Grunze, M. *J. Vac. Sci. Technol., A* **1992**, *10*, 2758.

(73) Weisshaar, D. E.; Walczak, M. M.; Porter, M. D. *Langmuir* **1993**, *9*, 323.

(74) Widrig, C. A.; Alves, C. A.; Porter, M. D. *J. Am. Chem. Soc.* **1991**, *113*, 2805.

(75) Schneider, T. W.; Buttry, D. A. *J. Am. Chem. Soc.* **1993**, *115*, 12391.

(76) Imabayashi, S.-I.; Iida, M.; Hobara, D.; Feng, Z. Q.; Niki, K.; Kakiuchi, T. *J. Electroanal. Chem.* **1997**, *428*, 33.

(77) Snyder, S. R.; White, H. S. *J. Phys. Chem.* **1995**, *99*, 5626.

(78) Chidsey, C. E. D.; Loiacono, D. N. *Langmuir* **1990**, *6*, 682.

(79) Sondag-Huethorst, J. A. M.; Fokkink, L. G. J. *Langmuir* **1995**, *11*, 2237.

(80) Guo, L.-H.; Facci, J. S.; McLendon, G.; Mosher, R. *Langmuir* **1994**, *10*, 4588.

(81) Schweiss, R.; Mirsky, V. M.; Wolfbeis, O. S. *Mater. Sci. Forum* **1998**, *287-288*, 427.

(82) Nuzzo, R. G.; Dubois, L. H.; Allara, D. L. *J. Am. Chem. Soc.* **1990**, *112, number 2*, 558.

(83) Trevor, D. J.; Chidsey, C. E. D. *J. Vac. Sci. Technol., B* **1991**, *9*, 964.

(84) Geguzin, Y. E.; Kovalev, G. N.; Ovcharenko, N. N. *Sov. Physics-Solid States* **1964**, *5*, 2627.

(85) Nuzzo, R. G.; Zegarski, B. R.; Dubois, L. H. *J. Am. Chem. Soc.* **1987**, *109*, 733.

(86) Trevor, D. J.; Chidsey, C. E. D.; Loiacono, D. N. *Phys. Rev. Lett.* **1989**, *62*, 929.

(87) Tudos, A. J.; Johnson, D. C. *Anal. Chem.* **1995**, *67*, 557.

Table 1. Reductive desorption peak potentials (E_p, V), the integrated charges (Q_d, μC /cm^2) under T and S waves, and total integrated charges (Q_t, μC/cm^2) for mercaptohexdecanoic acid (MHA) at different immersion times.

Immersion time (min)	$E_{p,T}$ (V)	$E_{p,S}$ (V)	$Q_{d,T}$ [a] (μC/cm^2)	$Q_{d,S}$ [a] (μC/cm^2)	Q_t [b] (μC/cm^2)
0.03	-0.97	-1.23	12.9	48.2	61.1
0.2	-0.97	-1.22	13.8	51.7	65.5
0.5	-0.99	-1.23	32.4	56.0	88.4
1	-1.00	-1.24	30.2	58.6	88.8
6	-1.01	-1.23	33.6	59.5	93.1
30	-1.02	-1.23	39.8	60.3	101.1
60	-1.04	-1.22	40.6	56.9	97.5
120	-1.05	-1.22	55.1	40.6	95.7
583	-1.05	-1.22	64.6	37.8	102.4
888	-1.05	-1.22	68.1	28.5	96.6

[a] The values of Q_d are calculated from the area under each of the wave after compensating for charging current, and are divided by the area of the O-ring. The area of a wave is obtained by deconvolution of the waves. The current flow for double layer charging was estimated by using a straight capacitive baseline.

[b] $Q_t = Q_{d,T} + Q_{d,S}$

Table 2. STM determined roughness factors (RFs) for as-evaporated Au/mica and for the HDT and ET coated as-evaporated Au/mica.

Sample	RFs [a,]
uncoated as-evaporated Au/mica	1.17 ±0.01
HDT coated as-evaporated Au/mica	1.17 ±0.03
ET coated as-evaporated Au/mica	1.13 ±0.01

[a] The STM RFs were determined by dividing the actual surface area of an image by its geometric surface area. These results reflect the characterizations of samples for at least five separate 250 nm x 250 nm areas on each sample and the uncertainties are given as standard deviations.

Table 3. The gold dissolution in thiol solutions as determined by graphite furnace atomic absorption spectroscopy (GFAAS).

Precursor solution	Substrate treatment	[Au] (ppb)[a]	Equivalent Au monolayers coverage (%)[b]
Hexanethiol (no Au)	25°C	0	0
Neat ethanol	25°C	0	0
Hexanethiol	25°C	19	1.56
	300°C (2)[c]	<2	N/A
Decanethiol	25°C (2)	6.1	0.50
	200°C	4.6	0.38
	300°C (3)	<2	N/A
Mercaptoundecanoic Acid	25°C (2)	13.8	1.1
	200°C	9.3	0.76
	300°C (2)	<2	N/A

[a] Detection limit with a 10 μL sample: 2 parts per billion (ppb).
[b] Surface concentration of gold atoms: 1.4×10^{15} atoms/cm^2.
[c] Number of samples.

Table 4. STM-determined roughness factors on samples with different treatments.

Sample treatment	STM RFs [a, b]
As-evaporated Au/mica, no annealing	1.14 ±0.01
Au/mica annealed at 100°C for 12 hr	1.13 ±0.01
Hexadecanethiolate (HDT) coated Au/mica annealed at 100°C for 12 hr	1.10 ±0.01

[a] The STM roughnesses were determined by dividing the actual surface area of an image with its geometric surface area. RFs are calculated based on 3 sampled areas. The RF for as-evaporated Au/mica without annealing (1.14) is slightly less than that listed in Table 1 (1.17) because a different STM tip and larger scanning areas were used to collect this set of data.
[b] The STM images are 800 nm x 800 nm.

Figure Captions

Figure 1. Voltammetric curves for the reductive desorption of mercaptohexadecanoic acid monolayers chemisorbed at as-evaporated Au/glass at different immersion times. Concentration of precursor solution: 0.06 mM. Electrolyte: 0.5 M KOH. Scan rate: 50 mV/s.

Figure 2. Plot of the integrated charges of the electrochemical reductive desorption waves from Figure 1 vs. immersion time.

Figure 3. C-H stretching region of the ex-situ infrared reflection absorption spectra of mercaptohexadecanoic acid monolayers chemisorbed at as-evaporated Au/glass at different immersion times. The dashed line shows the peak position of the $\nu_a(CH_2)$ stretch at 0.033 min immersion.

Figure 4. Voltammetric curves for the reductive desorption of mercaptoundecanoic acid monolayers chemisorbed at as-evaporated Au/glass at different immersion times. Concentration of precursor solution: 0.03 mM. Electrolyte: 0.5 M KOH. Scan rate: 50 mV/s.

Figure 5. Voltammetric curves for the reductive desorption of mercaptopropionic acid monolayers chemisorbed at as-evaporated Au/glass at different immersion times. Concentration of precursor solution: 0.03 mM. Electrolyte: 0.5 M KOH. Scan rate: 50 mV/s.

Figure 6. Voltammetric curves for the reductive desorption of (A) mercaptohexadecane thiolate and (B) ethanethiolate monolayers chemisorbed at as-evaporated Au/mica (thick line) and annealed Au/mica (thin line). Concentration of precursor solution: 1 mM. Electrolyte: 0.5 M KOH. Scan rate: 50 mV/s. Immersion time: overnight.

Figure 7. Scheme showing a Au(111) surface with a terrace and a step. Coordination numbers of at terrace, step, and kink are listed.

Figure 8. STM images of (A) Au/mica annealed at 100°C for 12 hr and (B) HDT coated Au/mica annealed in conditions same as (A). The scan size is 800 nm x 800 nm.

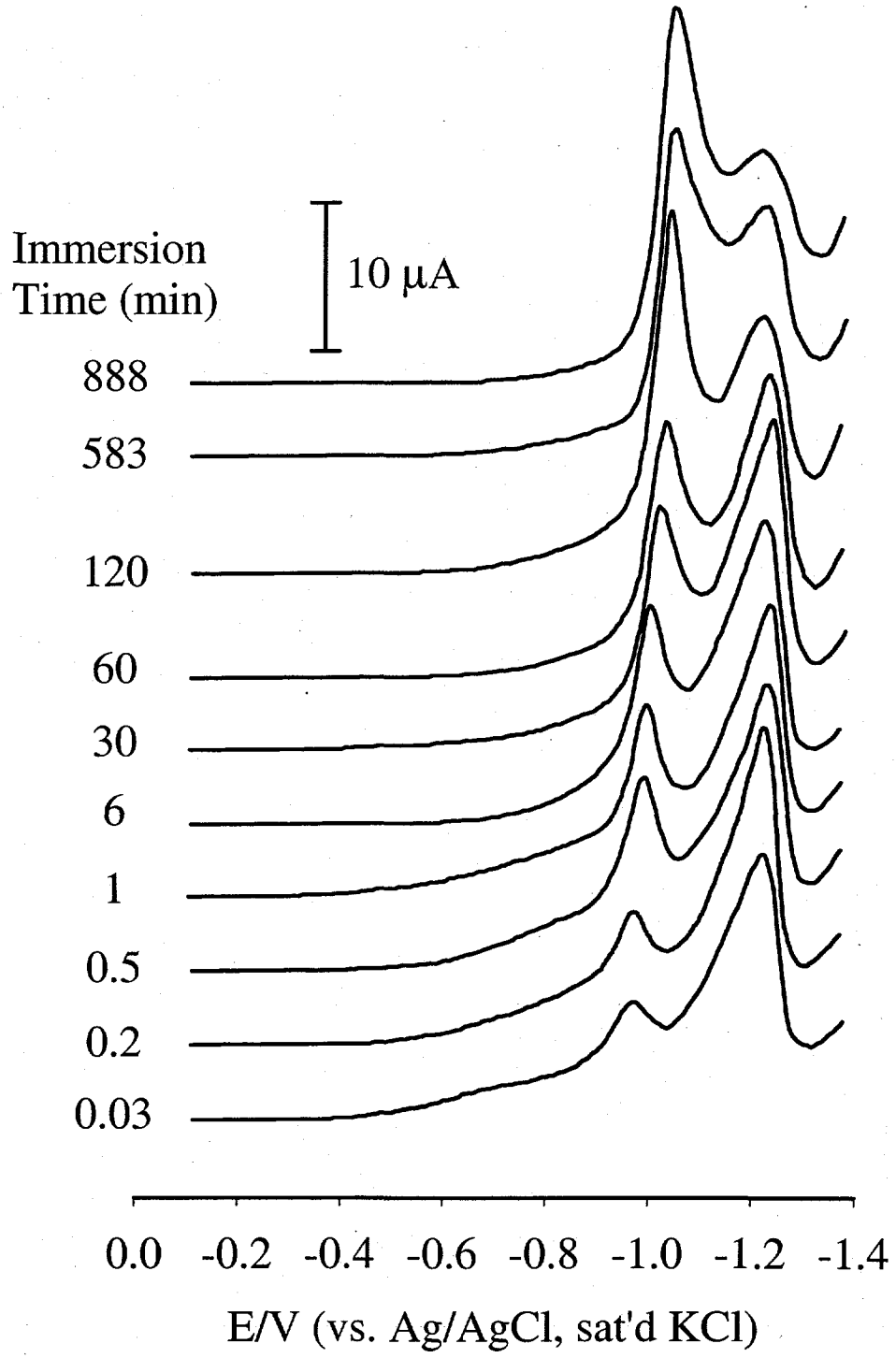
Immersion
Time (min)
10 μA
888
583
120
60
30
6
1
0.5
0.2
0.03
0.0 -0.2 -0.4 -0.6 -0.8 -1.0 -1.2 -1.4
E/V (vs. Ag/AgCl, sat'd KCl)

Figure 1

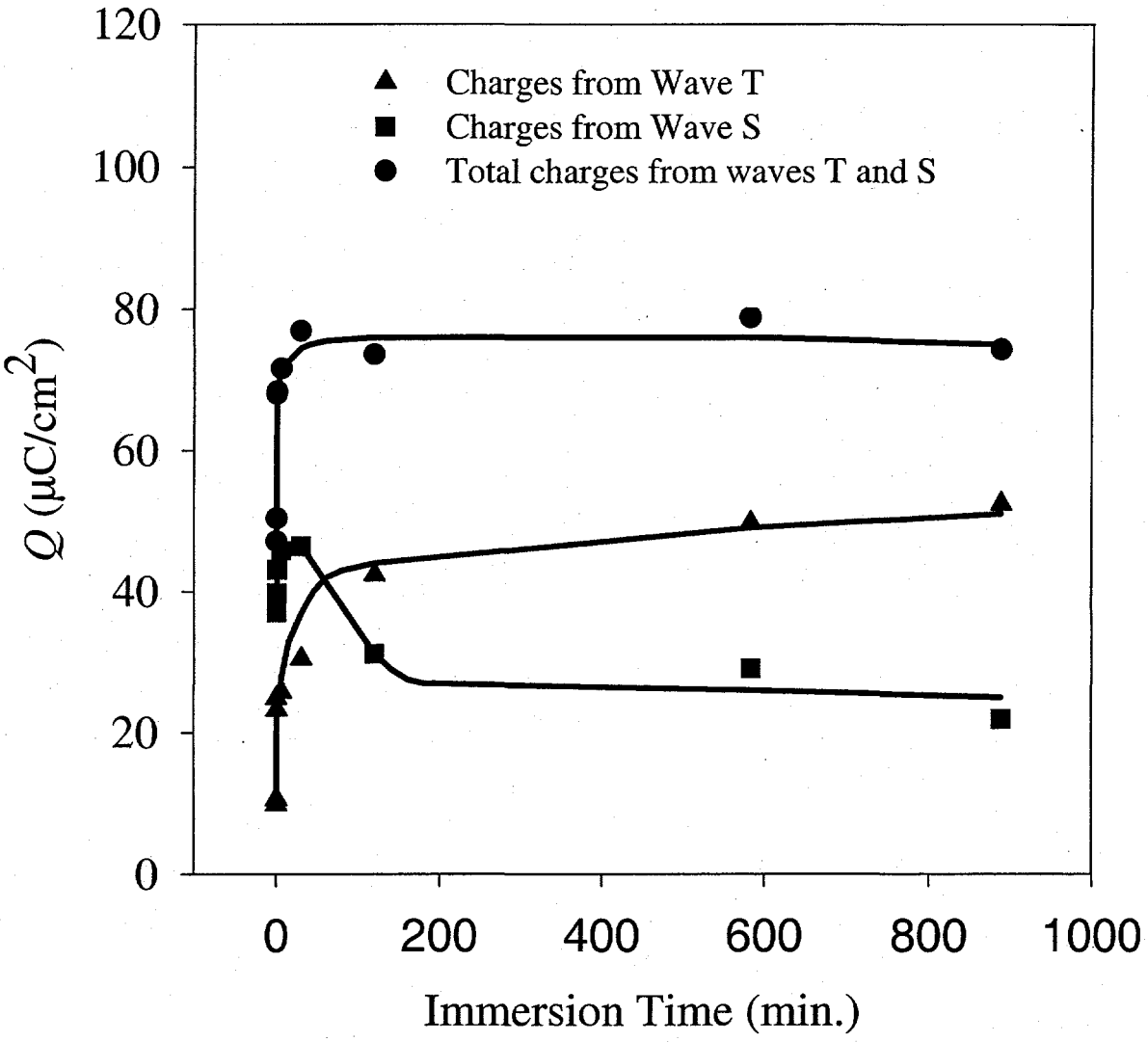
120
100
80
60
40
20
0
Q (μC/cm2)
Charges from Wave T
Charges from Wave S
Total charges from waves T and S
0
200
400
600
800
1000
Immersion Time (min.)

Figure 2

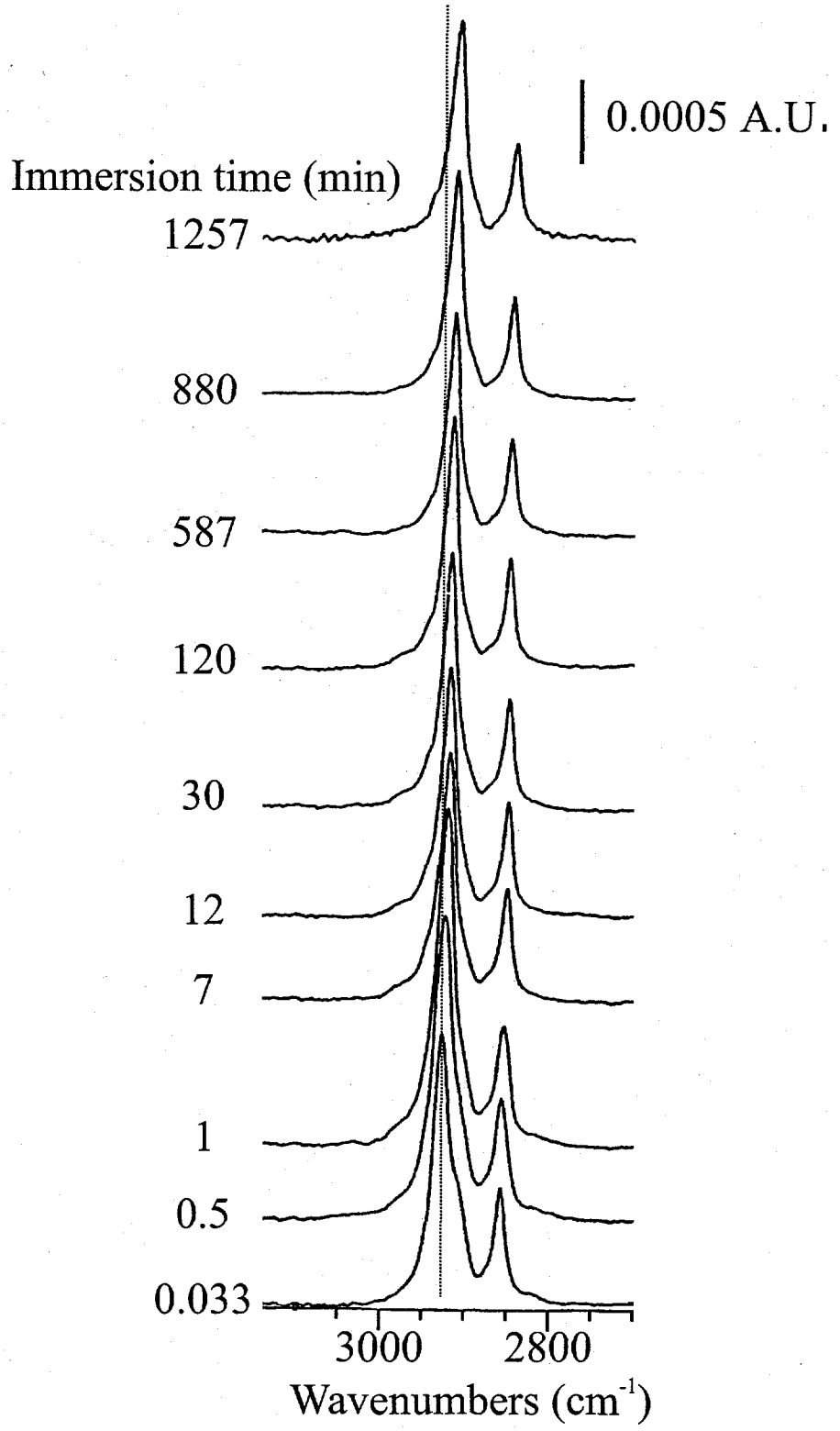
0.0005 A.U.
Immersion time (min)
1257
880
587
120
30
12
7
1
0.5
0.033
3000
2800
Wavenumbers (cm-1)

Figure 3

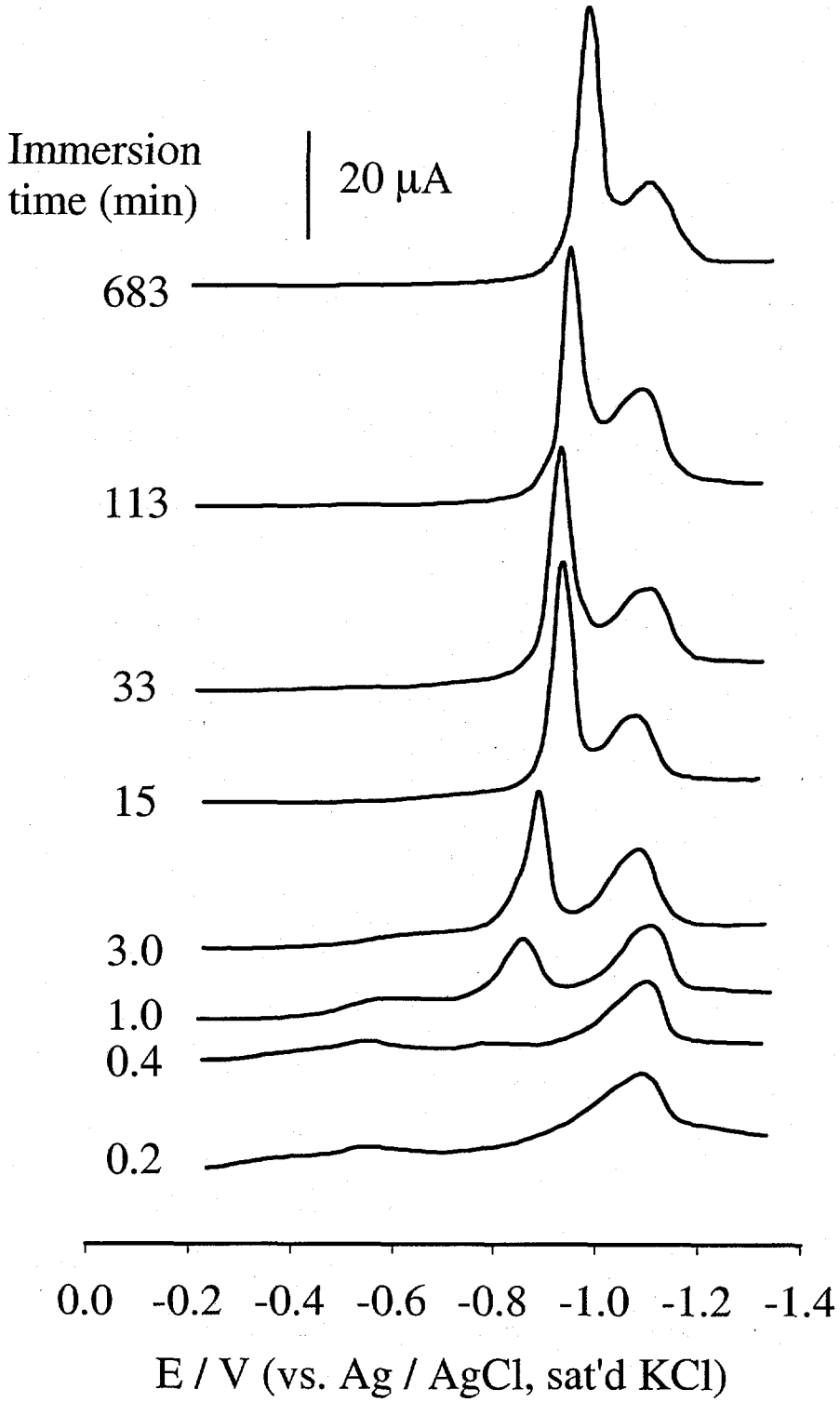
Immersion
time (min)
20 μA
683
113
33
15
3.0
1.0
0.4
0.2
0.0 -0.2 -0.4 -0.6 -0.8 -1.0 -1.2 -1.4
E / V (vs. Ag / AgCl, sat'd KCl)

Figure 4

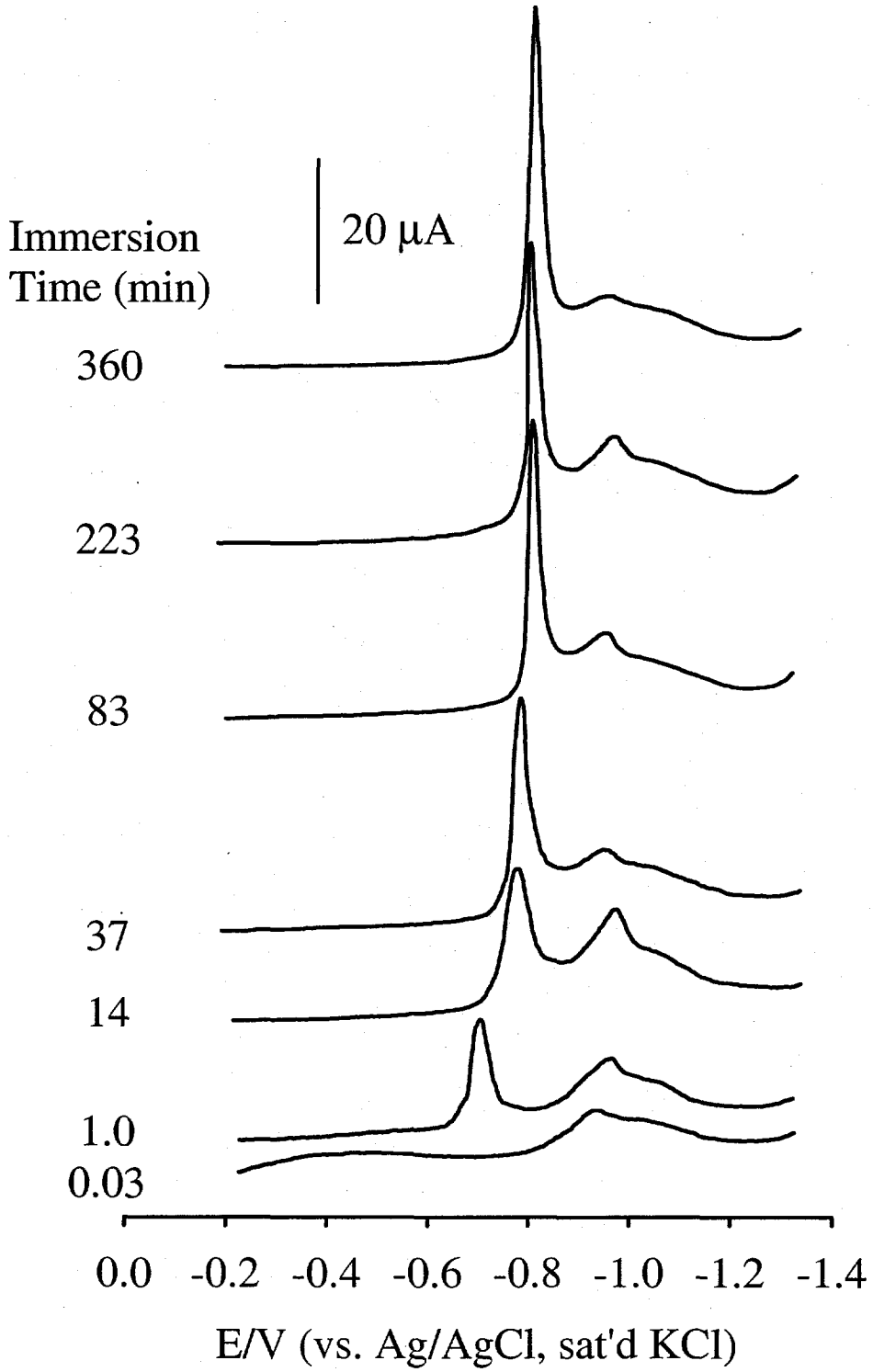
Immersion
Time (min)
20 μA
360
223
83
37
14
1.0
0.03
0.0 -0.2 -0.4 -0.6 -0.8 -1.0 -1.2 -1.4
E/V (vs. Ag/AgCl, sat'd KCl)

Figure 5

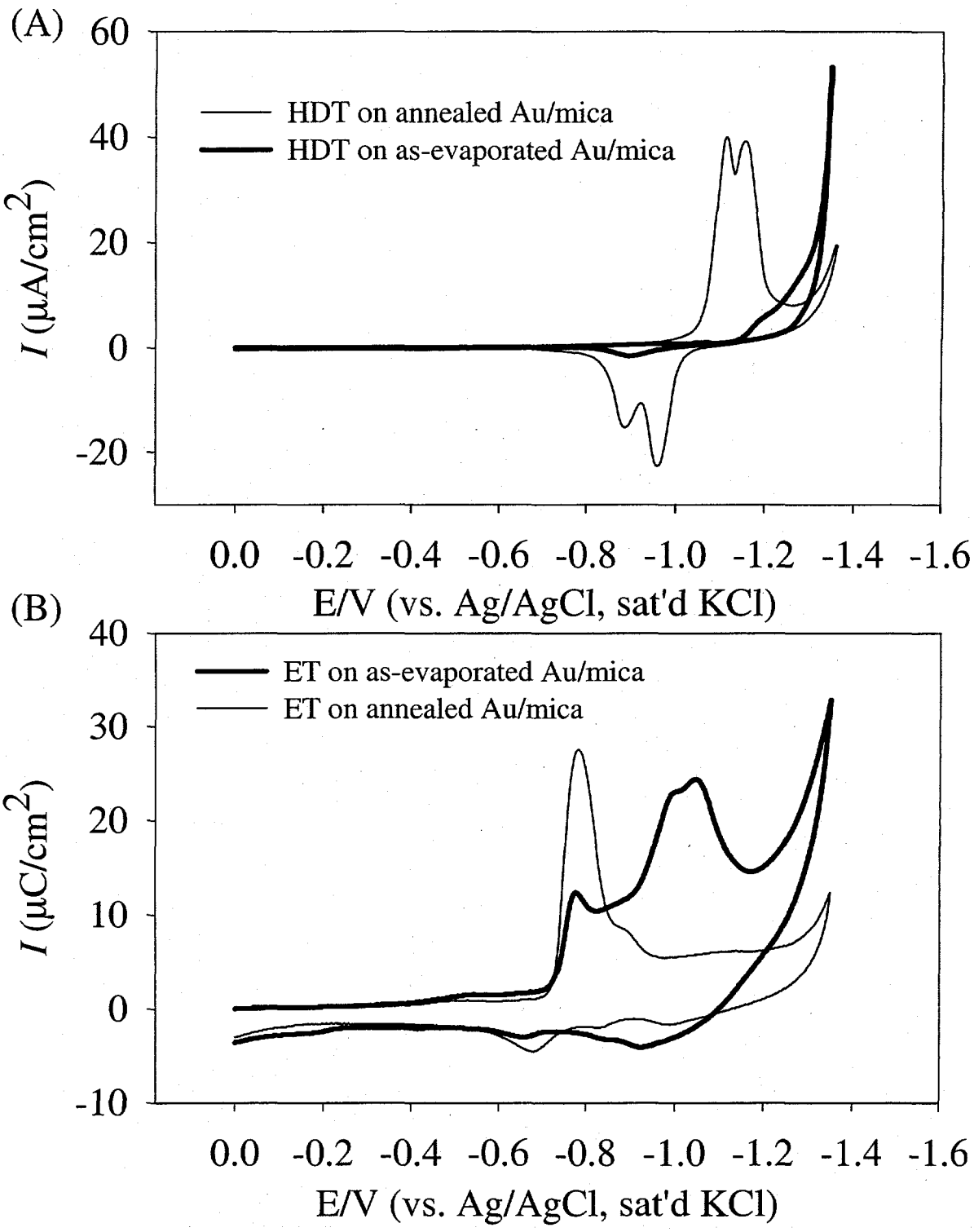
(A)
60
40
20
0
-20
I (μA/cm2)
HDT on annealed Au/mica
HDT on as-evaporated Au/mica
0.0 -0.2 -0.4 -0.6 -0.8 -1.0 -1.2 -1.4 -1.6
E/V (vs. Ag/AgCl, sat'd KCl)
(B)
40
30
20
10
0
-10
I (μC/cm2)
ET on as-evaporated Au/mica
ET on annealed Au/mica
0.0 -0.2 -0.4 -0.6 -0.8 -1.0 -1.2 -1.4 -1.6
E/V (vs. Ag/AgCl, sat'd KCl)

Figure 6

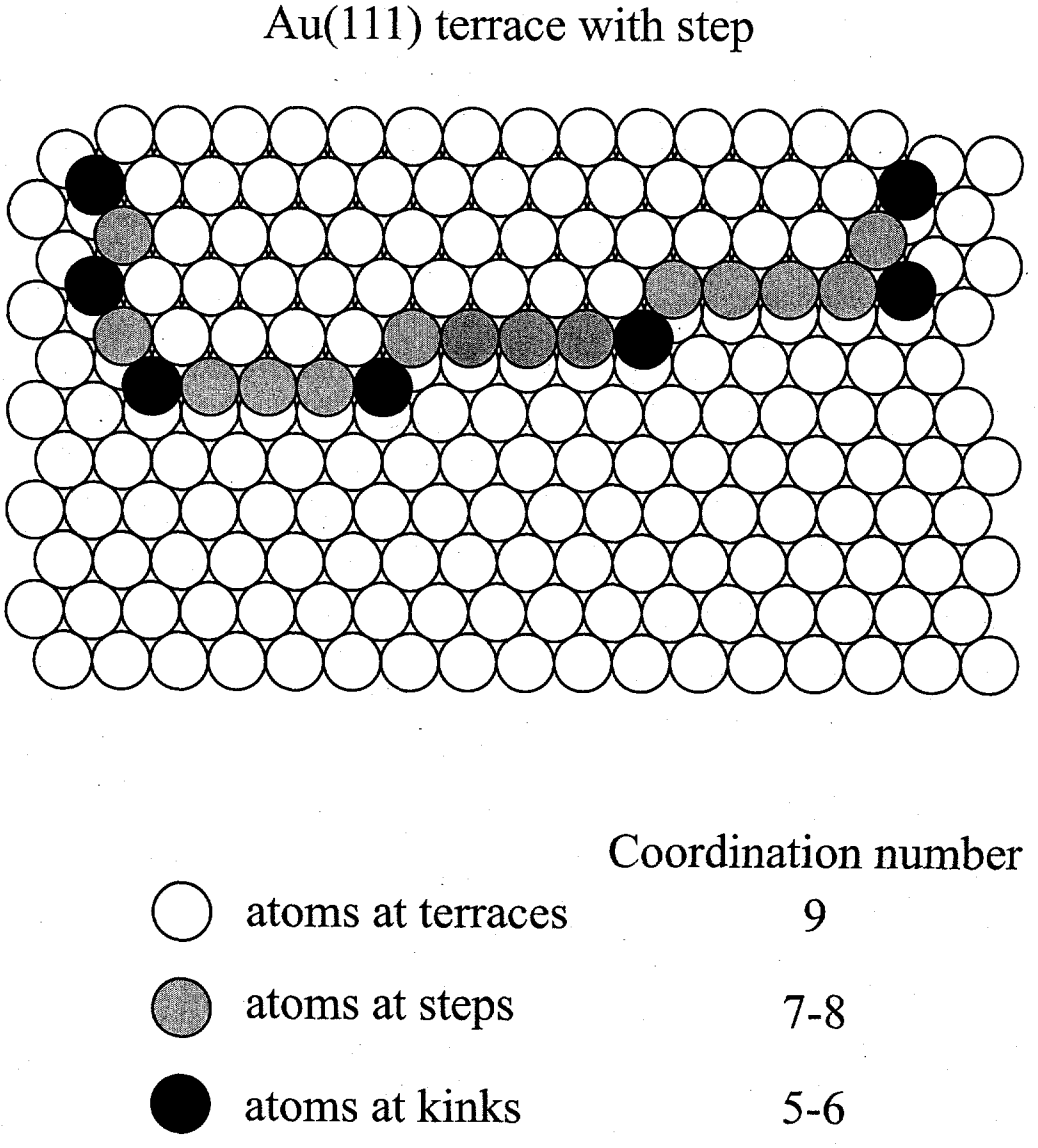
Au(111) terrace with step
Coordination number
atoms at terraces
9
atoms at steps
7-8
atoms at kinks
5-6

Figure 7

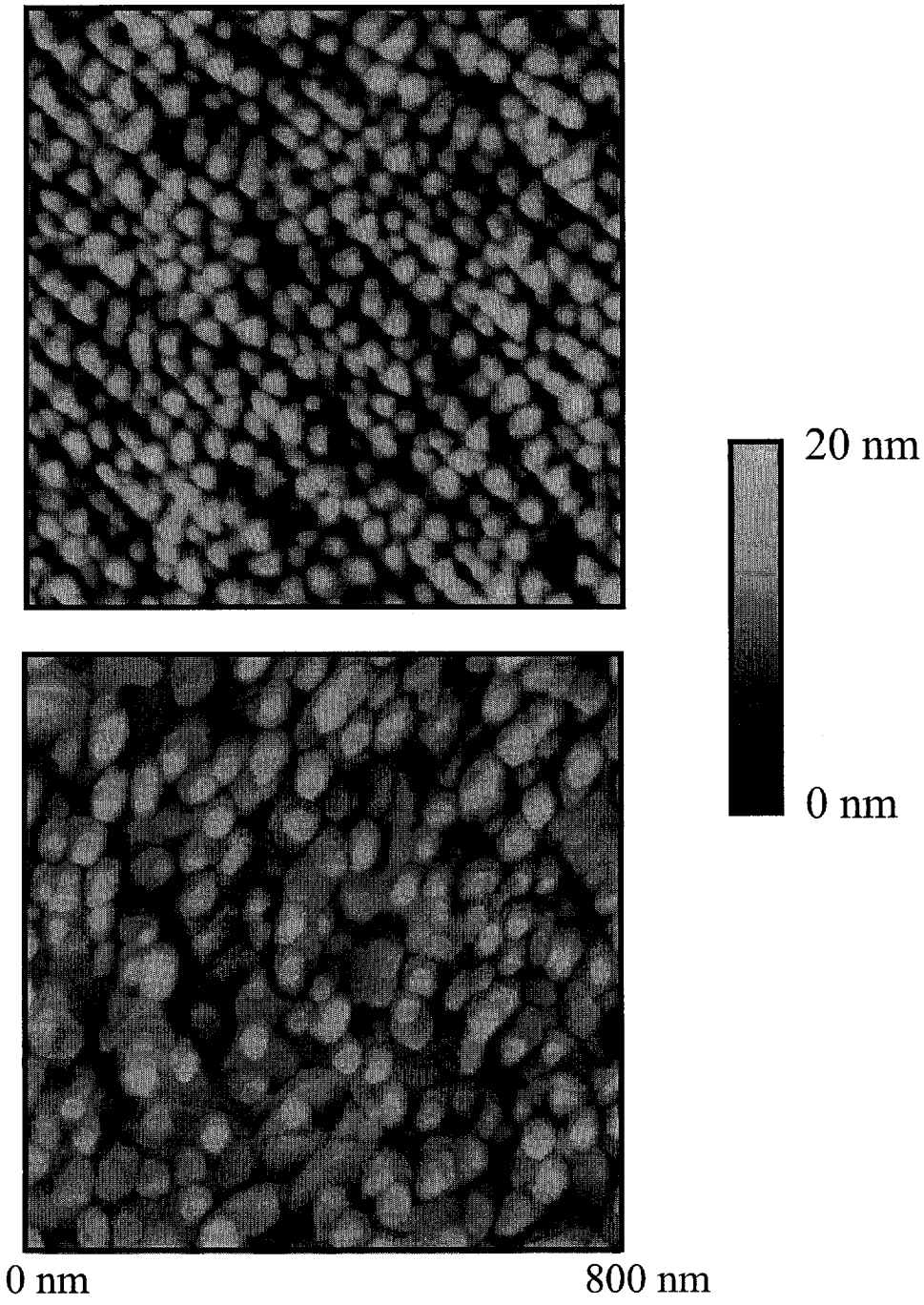

Figure 8

CHAPTER 2. ORIGIN OF THE MULTIPLE VOLTAMMETRIC DESORPTION WAVES OF LONG CHAIN ALKANETHIOLATE MONOLAYERS CHEMISORBED ON ANNEALED GOLD ELECTRODES

A paper to be submitted to *Journal of Electroanalytical Chemistry*

Sze-Shun Wong and Marc D. Porter

Abstract

This paper examines possible factors responsible for the voltammetric fine structure exhibited from the reductive desorption and oxidative redeposition of long chain alkanethiolate monolayers on smooth gold electrodes. Results reveal that the fine structure is connected to the local order of the adlayer. This conclusion is based on a series of characterizations of monolayers formed from hexadecanethiol (HDT) and octadecanethiol (ODT) on annealed mica-supported gold (annealed Au/mica) and on template-stripped gold (TSG). For annealed Au/mica, a pair of overlapping waves separated by 20 to 100 mV are found for both the desorption and the redeposition process. In contrast, the voltammetry of the TSG system exhibits a single wave for the two processes. Findings from morphological assessments (oxidative stripping of iodine, scanning tunneling microscopy, and underpotential metal deposition of lead) of the underlying substrates reveal that the differences in the voltammetry are connected to a subtle difference in the microscopic roughness of the two substrates. The morphological data indicate that the surfaces of annealed Au/mica and of TSG are strongly (111)-terraced, but that the sizes of the (111) terraces at TSG are significantly smaller. As a consequence, the TSG surface has a higher

density of steps. Since the adlayer domain size is ultimately limited by the microscopic topography of the substrate, the voltammetric differences observed for the two types of substrates are attributed to differences in the ordering of the adlayer. A description of the differences in the processes for the desorption and redeposition is proposed and is examined within the context of recent interpretations.

1. Introduction

Several laboratories [1-17], including our own [18-22], have described a variety of interesting aspects about the reductive desorption and oxidative deposition for alkanethiolates chemisorbed at gold electrodes (i.e., Equation 1). We have found, for example, that the

$$X(CH_2)_nS\text{-}Au + e^- \leftrightarrow X(CH_2)_nS^- + Au \quad (1)$$

desorption process at smooth electrodes (i.e., annealed mica-supported gold) reflects the presence of thiolates bound on the terrace sites of Au(111) [21]. At rougher surfaces (e.g., as-evaporated mica-supported gold), however, the desorption process exhibits characteristics for thiolates bound on both terrace and step sites [21]. In general, the voltammetric waves for desorption from step sites are a few hundred millivolts negative of those for desorption from terrace sites [21].

We have also recently reported an unexpected dependence of the voltammetric reductive desorption curves on the number of carbons in the alkyl chain (N_c) for *n*-alkanethiolates chemisorbed at smooth gold [18]. This study found that the reductive desorption and oxidative redeposition processes for $N_c>10$ displayed multiple voltammetric waves that were separated in total by ~100 mV or less. In contrast, only a single wave was

detected for monolayers with $N_c \leq 10$. We proposed that this "fine structure" originated from the existence of different sized domains in the longer chain monolayers. Morin and co-workers have presented similar findings and interpretations [7].

This paper describes the results from a series of experiments designed to test the viability of the above assertion by assessing the effect of substrate roughness on the domain size of the adlayer. We show that roughness, which affects the local order of the adlayer, can ultimately be correlated to the presence or absence of the voltammetric fine structure. These findings are examined within the context of other possible explanations, including a recent two-step mechanism involving the formation of physisorbed micelles of long chain thiolates after desorption [8, 9, 13, 23].

2. Experimental

2.1 Gold Substrate Preparation

Two types of substrates were used, both of which were prepared by the vapor deposition of 300 nm (0.3 nm/s deposition rate) of gold onto fleshly cleaved mica (Au/mica) (B & M Trading Inc.) at ambient temperature. One type of substrate was then annealed at 300°C for 5 hr in a muffle furnace (annealed Au/mica). The other type of substrate was prepared by template stripping [24, 25]. Template-stripping is a lift-off technique that involves affixing the exposed side of annealed Au/mica onto a glass support with epoxy. The assembly is subsequently cured to form a mica/gold/epoxy/glass sandwich. The samples are then immersed in tetrahydrofuran, which causes the delamination of the gold film from mica.

This process exposes the underlying gold surface that was originally in contact with mica. These substrates will be referred to as template-stripped gold or TSG.

2.2 Monolayer Preparation

Ethanol (Quantum, punctilious grade), hexadecanethiol (HDT), and octadecanethiol (ODT) (Aldrich) were used as received. The electrodes were coated by immersion into 1 mM HDT or ODT ethanolic solutions for at least 2 hr. After removal from solution, the modified electrodes were rinsed with copious amounts of ethanol and dried under a stream of high purity argon.

2.3 Instrumentation and Procedures

2.3.1. Electrochemistry

The electrodes were mounted in a conventional three-electrode cell with an exposed geometric area, defined by the size of an O-ring, of 0.58 cm^2. A Ag/AgCl/saturated KCl electrode was used as the reference electrode, and all values of applied potential are reported with respect to this electrode. The auxiliary electrode was a coiled Pt wire. Deionized water, which was purified by passage through a Milli-Q filtration system, was used for all solution preparations. Data were collected using a CV-27 potentiostat (Bioanalytical Systems). Solutions were deoxygenated with argon. Cyclic voltammetric experiments were performed using 0.5 M KOH (99.99%, Aldrich) electrolyte solutions.

The microscopic surface areas for each of the uncoated gold substrates were assessed by the oxidative stripping of chemisorbed iodine [26-28]. Samples were prepared by immersion into an aqueous solution of 1 mM KI and 1 M H_2SO_4 for 1 min. The samples were then removed, rinsed with 1 M H_2SO_4, and characterized voltammetrically in 1 M H_2SO_4. The amount of chemisorbed iodine was determined by the charge passed for the oxidative stripping to aqueous IO_3^-. Roughness factors were then calculated by dividing the microscopic surface area by the geometric surface area.

The stripping of underpotentially deposited (upd) lead was used for the characterization of the surface crystallinity of each substrate by comparisons to the voltammetric curves for single and stepped crystal gold electrodes [29-34]. Lead was deposited from a solution of 1 mM PbO in 1 M $HClO_4$ by scanning the applied voltage at 20 mV s^{-1} from +0.30 to -0.30 V. Stripping curves were obtained upon reversal of the scan direction.

2.3.2. Scanning Tunneling Microscopy (STM)

Images (515 x 512 pixels) acquired by STM were obtained in ambient conditions using a Digital Instruments Nanoscope III STM. The instrument was equipped with a 0.7 μm scanner head. The height mode, which maintains a constant current between the tip and sample, was utilized for all imaging. The STM probe tips were fabricated by etching electrochemically a 0.025 cm diameter tungsten wire in 0.5 M KOH. Typical tunneling

currents and bias voltages used for these images were 500-1000 pA and 500-1000 mV, respectively.

3. Results and discussion

3.1. General voltammetric characteristics of long chain alkanethiolate monolayers on annealed Au/mica and TSG

Cyclic voltammograms for the reductive desorption and partial oxidative redeposition of HDT and ODT at the two different gold substrates are presented in Figures 1 and 2, respectively. These curves were collected in 0.5 M KOH(aq) at a scan rate of 50 mV s^{-1}. The scans were initiated at 0.00 V and reversed at –1.35 V. Curve A in each figure is for monolayers on annealed Au/mica and curve B is for monolayers on TSG. Table 1 summarizes several features of these data, including the peak potentials for the reductive (E_{rd}) and oxidative (E_{od}) waves and the total charge passed under the waves in the cathodic (Q_{rd}) and anodic (Q_{od}) scans.

The voltammetric data for HDT on annealed Au/mica (Figure 1A) are characterized by the presence of two overlapping waves for both the cathodic and anodic scans. The values for E_{rd} are -1.11 V and -1.15 V and for E_{od} are -0.90 V and -0.96 V, with a sample-to-sample variability in peak potential of ±10 mV. The peak separation between the two waves in the cathodic scan is therefore 40 mV whereas the separation is 60 mV for the two waves in anodic scan. The voltammetric curves for ODT on annealed Au/mica (Figure 2A) are also characterized by the presence of two overlapping waves in each scan direction. The values of

E_{rd} are -1.12 V and -1.19 V and of E_{od} are -0.90 V and -1.01 V. The peak separations are 70 and 110 mV for the cathodic and anodic scans, respectively. For both adlayers, the values of Q_{od} are smaller than those of Q_{rd}. This difference is a result of the partial depletion of desorbed thiolate to bulk solution. A more quantitative analysis of these data (e.g., determination of the charge under each wave) is, however, complicated by the extensive overlap of the waves.

In contrast to the curves at annealed Au/mica, those for HDT (Figure 1B) and ODT on TSG (Figure 2B) consist of only one wave in the cathodic scan and one wave in the anodic scan. The curve for HDT has a E_{rd} of -1.12 V and a E_{od} of -0.94 V, whereas that for ODT has a E_{rd} of -1.15 V and a E_{od} of -0.98 V. This single-peak characteristic is similar to the reductive desorption curves for $N_c<11$ at annealed Au/mica [18]. We note that the peak potentials for TSG are located between those for the two waves for annealed Au/mica in both scan directions.

What then is the origin of the difference in the voltammetric curves for the two different substrates? As noted, our earlier investigation [18] and that of Morin and co-workers [7] found that long chain ($N_c>10$) adlayers formed on atomically smooth Au(111) exhibit the fine structure shown in Figures 1A and 2A. These findings led to speculation that the differences arise from the dependence of the cohesive interactions between neighboring adsorbates on the length of the alkyl chain [18]. Short chain adlayers, based on STM observations [35-38], have smaller ordered domains than longer chain adlayers. Thus, desorption would be more facile for short chain adlayers because of a greater number of

defects. This insight suggests that the differences between the curves in both Figures 1 and 2 may be connected to differences in the two types of substrate, which may in turn affect adlayer domain size. As a starting point in examining this possibility, the next section presents the findings from a multi-technique characterization of the surface morphology of the different substrates.

3.2. Characterizations of the uncoated gold substrates

3.2.1. Electrochemical roughness factor determinations

The oxidation of adsorbed iodine [26-28] was used as a starting point in assessments of the roughness for the two types of substrates. Roughness factors (RFs) were determined by comparing the experimentally determined surface concentration of iodine [26-28] with the theoretically limiting surface concentration of iodine (1.02×10^{-9} mol cm^{-2}) at atomically smooth Au(111) (the maximum surface concentration of adsorbed iodine is 0.44 times the number of surface atoms at Au(111) (2.3×10^{-9} mol cm^{-2}) [39]).

The results from these assessments are listed in Table 2. As is evident, the electrochemical RF for annealed Au/mica is less than that for TSG. Recent characterizations of the surface of various Au substrates [24, 25] have found that TSG is morphologically more similar to annealed Au/mica than is suggested by the electrochemical RF data. However, these earlier literature reports heated the mica substrate to 300°C during gold deposition; this part of the procedure, which leads to enlargement of the grain sizes of the gold film, was not

used in our preparation. As such, the electrochemical RF values in Table 2 begin to delineate a potentially important microscopic difference between the surfaces of the two substrates.

3.2.2. STM characterizations

The results from STM characterizations of the uncoated substrates are shown in Figures 3 and 4. Figure 3 presents 5 μm x 5 μm images, and Figure 4 presents 500 nm x 500 nm images. In each figure, part A is an image for annealed Au/mica and part B is an image for TSG. All images are accompanied by cross-section plots that provide topographical insights into the microscopic roughnesses of the two different substrates. Figure 3A shows that annealed Au/mica has crystalline diameters as large as 150-200 nm that are separated by grain boundaries of varied width and depth. Though unclear how the finite size and shape of the tip influences an accurate assessment of the depths of the grain boundaries [40-43], the grain boundaries in some of the observed images (data not shown) are at least 15 nm deep.

The 5 μm x 5 μm image of TSG is markedly different from that of annealed Au/mica. At this length scale, the TSG surface appears to be much smoother, with fewer identifiable grain boundaries. There are, however, some fairly deep pinholes in TSG. We suspect that these pinholes, which are at least 3 to10 nm deep in some images, originate from the presence of aggregated contaminants or microparticulates strongly adsorbed on the mica surface. The presence of these microstructures translates into small, localized protrusions on the mica surface that are imprinted on the gold film during deposition. We have found that the numbers and sizes of the holes can be reduced when the mica is heated at higher temperature,

e.g., 300°C for 30 min., before the Au deposition, a finding consistent with the proposed origin of these holes.

The 500 nm x 500 nm images in Figure 4 provide a perspective of the surface topography at a greater level of detail. Comparing Figure 4A and 4B shows that many of the terraces (150-200 nm wide) on annealed Au/mica are significantly larger than those for TSG (50-80 nm wide). Since characterizations (i.e., X-ray diffraction) [21] of evaporated gold films demonstrate that the bulk of such films has a (111) crystallinity, these images argue that TSG has a significantly larger number of steps than annealed Au/mica. Therefore, TSG can be roughly described as a smooth but more stepped surface, whereas that at annealed Au/mica is a smooth surface composed of larger terraces with a lower number of step sites.

Table 2 lists RFs developed from typical STM images of the substrates at several different locations. These RFs were determined from dividing the surface area calculated from the topography of the images by the geometric area of the images using the roughness determination function of the STM software. These results, which are qualitatively consistent with those from the electrochemical characterizations, reveal that the surface of annealed Au/mica is smoother at a microscopic level than that of TSG. We note, however, that the electrochemical RF values are consistently higher than the STM RF values. This difference is attributed largely to the finite number of data points that are used to construct an STM image. That is, the images in both Figures 3 and 4 are composed of 512 x 512 pixels. This pixel density roughly corresponds to a data point per 100 nm^2 (~1 data point for every 1000 gold atoms) in Figure 3 and 1 nm^2 (~1 data point for every 10 gold atoms) in Figure 4.

As a consequence, the true topographies of the surfaces are undersampled (i.e., smoothed) by the limited data density. This situation is compounded by the possibility that the finite size of the tip may preclude accurate sampling of features with large local changes in contour.

To this point, we have determined that the surface of annealed Au/mica is morphologically distinct from that of TSG. These results indicate that the surface of annealed Au/mica has larger terraces and is less extensively stepped at an atomic scale than that of TSG. Coupled with the surface morphological insights from the upd of lead that are described in the next section, the STM data point to the differences in surface topography, and more specifically, the impact on the terrace sizes of the adlayer, as a key contributor to the differences in the voltammetric curves.

3.2.3. Characterization of the surface crystallinities by stripping of underpotentially deposited lead

The surface crystallinities of the two gold substrates were characterized using the oxidative stripping of underpotentially deposited lead. This characterization exploits the findings from several systematic studies which have shown that the stripping curves are dependent on the crystal face, terrace length, and step density of the gold surface [29-32, 44]. These experiments therefore potentially provide an important additional assessment of the surface microstructure for the two types of substrates.

Figure 5 shows the voltammograms for stripping lead from the two types of gold substrates. At annealed Au/mica (Figure 5A), the stripping curve consists largely of a sharp

wave located at -0.16 V. There are also two smaller waves. One of the waves appears at -0.20 V and overlaps with the wave at -0.16 V; the other is located at +0.17 V. This voltammogram is diagnostic for the desorption of lead from the (111) crystalline plane of a gold surface, which is in agreement with results from earlier characterizations of annealed gold films [29-34]. Furthermore, the wave at -0.16 V is indicative of the presence of (111) terraces with extended lengths (i.e., 11 atoms or larger) [30, 31]. In contrast, the wave at -0.20 V reveals the existence of terraces with smaller lengths. A rough approximation of the areas under each of the overlapping waves suggests that the large and small (111) terraces constitute ~80 and 20% of the surface, respectively. In addition, the absence of waves diagnostic of the (100) and (110) crystalline planes, which are located between those at +0.17 V and -0.16 V, demonstrates that the Au(111) surface is devoid of detectable step sites [34] (5% estimated detection limit).

The voltammetric curve for the stripping of underpotentially deposited lead from TSG (Figure 5B) has some of the same characteristics of that for annealed Au/mica as well as some differences. Like annealed Au/mica, the curve for TSG is composed of the two overlapping waves (-0.17 V and -0.21 V); however, the relative magnitudes of the two waves are reversed, with the wave at -0.21 V larger than that at -0.17 V. There is also a broad wave present at +0.02 V for TSG that is absent at annealed Au/mica. This wave is indicative of (110) and (100) surface crystalline planes of gold, demonstrating that TSG has a more complex surface crystallinity than annealed Au/mica [30, 31]. An analysis of the charge under the waves suggests that the TSG surface is ~75% (111) and ~25% (110)-(100),

and that the (111) terraces with extended lengths comprise only ~20% of the (111) surface crystallinity.

We conclude from the characterization data in this section that the surface of annealed Au/mica exhibits a pronounced (111) crystallinity with large atomically smooth terraces. In contrast, the TSG surface is composed of smaller (111) terraces with a significantly large and more detectable fraction of steps. It is also important to note that the surfaces of both annealed Au/mica and TSG have a much lower number of step sites than the surface of as-evaporated gold-film electrodes. As-evaporated gold electrodes are devoid of extended terraces (i.e., those eleven atoms in length or larger) [21]. The surface of as-evaporated gold electrode is also much more polycrystalline, with detectable amounts of (100)-(110) step sites via the upd of lead. This higher level of step sites results in the presence of desoprtion waves that are a few hundred millivolts more negative than those observed in Figures 1 and 2. It therefore follows that the difference in the voltammetry of HDT and ODT in Figures 1 and 2 arises from a subtle difference in the surface microstructure of annealed Au/mica and TSG.

3.3. Correlation of voltammetry with surface morphology

Our findings argue that the presence of large (111) terraces on a gold electrode coincides with the observation of multiple voltammetric desorption/deposition waves for thiolate monolayers. Gold surfaces with smaller (111) terraces, like those of TSG, exhibit only one voltammetric wave. In view of this correlation, the issue is how differences in surface microstructure lead to the observed voltammetric differences. If the voltammetric

differences are a consequence of domain size, which is, in part, dictated by the substrate microstructure, it is of value to examine possible relationships between substrate terrace size and adlayer domain size. The following discusses various aspects related to this issue, building on our earlier work [18, 21] as well as that of others [5, 7, 9, 10, 12, 23]. We start by considering how the substrate roughness can influence adlayer formation and possible domain sizes.

The formation of monolayers on annealed Au/mica commences through a homogeneous nucleation process that we believe leads to aggregation of adsorbates on large, atomically smooth terraces, with aggregation occurring as a consequence of surface diffusion of the adsorbate or its precursors and, to a lesser degree, solution pre-assembly. Subsequently, domains of different sizes form on a terrace. Through surface diffusion and precursor-adsorbate exchange, some domains of smaller sizes merge to form larger ones [45, 46]. Substrates with smaller terrace sizes (i.e., TSG), by extension, have smaller domain sizes. These processes lead to a distribution of domain sizes and domain boundaries, as depicted in Figure 6, with differing resistances to desorption. We believe that it is the difference in resistance to desorption that results in the differences observed in the cathodic voltammetric curves.

Equations 2 and 3 represent the desorption process as two step mechanism, representing, in part, the combined weight of several earlier interpretations [5-12, 18-22].

$$Au\,|\,S(CH_2)_nCH_3 + e^- \rightarrow Au\,|\,^-S(CH_2)_nCH_{3\ (dl)} \qquad (2)$$

$$Au\,| + {}^{-}S(CH_2)_nCH_3\ _{(dl)} \rightarrow Au\,| + {}^{-}S(CH_2)_nCH_3 \qquad (3)$$

Equation 2 shows a faradaic one-electron process between electrode and chemisorbed thiolate where the product resides within the electrical double layer (represented by the subscript dl). Equation 3 depicts the loss of the product to bulk solution; this step is viewed as a capacitive process because of the change in the double layer structure. Depletion (i.e., Equation 3) applies more rigorously to the process involving short chain thiolates because of their higher solubility [47]. Long chain thiolates, because of their lower solubility, are less likely to diffuse into bulk solution, potentially forming micelle-like structures [8, 9, 13, 23] or other types of aggregates confined within the double layer .

In each case, reductive desorption is a convolution of the two steps. For short chain systems, desorption proceeds in a comparatively rapid two-step process. This situation is reflected by the observation of only a single desorption wave over a wide range of scan rates [18]. Because of lower solubility and greater cohesion between chains, however, longer chain systems (N_c>10) exhibit a subtle but detectable separation between the two steps [13]. It then follows, based on the topographic differences between annealed Au/mica and TSG, that the larger adlayer domains on Au/mica cause the separation between the two steps in Equations 2 and 3. In other words, the appearance of the more negative desorption wave with annealed Au/mica as the substrate arises from the rearrangement of the larger domains of the adlayer within the electrical double layer after faradaic cleavage of gold-sulfur bonds.

Evidence in support of this interpretation can be found in characterizations of the two-dimensional ordering of alkanethiolates via STM [25, 35, 37, 48-51]. These studies have

indicated that the average size of the domains increases as chain length increases [35]. Small ordered domains or disorganized domains have also been found at the boundaries between large domains. Thus, domains of different sizes have differences in stability with respect to desorption because of variations in cohesive interactions between chains and in permeability to counterions and solvent. Thus, a voltammetric fine structure arises from the desorption of thiolates from domains of different sizes. Similarly, the oxidative redeposition of the long chain thiolates shows a multiple wave response at annealed Au/mica. This response is also related to domains of different sizes. Long chain thiolates ($N_c \geq 14$) [18] desorbed from large domains are bound by cohesive interactions, and do not diffuse rapidly away from the electrode because of solubility. These thiolates are more easily redeposited on the surface (-0.96 V for HDT) than thiolates desorbed from small domains (-0.90 V for HDT) or domain boundaries.

To test our interpretation, two sets of experiments were conducted. The first investigated the reductive desorption of a "heat-treated" HDT monolayer formed on annealed Au/mica. Heat treatment refers to heating the as-formed HDT monolayer at 100°C in air for 4 hr to induce the partial desorption of the adlayer [38, 52-54]. As shown by others [52], such treatment creates large voids between domains, a greater number of voids, and a decrease in domain size. We therefore expect that the desorption voltammetry for a heat-treated sample would be qualitatively similar to that for TSG. Indeed, the voltammogram for a heat-treated sample (Figure 7A) has only one dominant wave in the cathodic scan (-1.12 V) and one dominant wave in the anodic scan (-0.94 V). The charge under the cathodic wave is

~90% of that before heat-treatment, consistent with the partial loss of adsorbates during heat-treatment.

We also tested whether the voltammetric fine structure would reappear if a "heat-treated" sample was re-immersed into the ethanolic HDT solution. The resulting voltammogram (for a 2 hr reimmersion) is shown in Figure 7B, and is characterized by the presence of two, overlapping waves in each scan direction. The values for E_{rd} are -1.11 V and -1.15 V and for E_{od} are -0.89 V and -0.95 V. The return of the fine structure is consistent with the qualitative features of our proposal.

The second test examined the reductive desorption of HDT monolayers formed at annealed Au/mica using octanol, instead of ethanol, as the solvent for assembly. The intent was to exploit the tendency of less polar solvents (e.g., hexadecane and long chain alcohols) to intercalate into the adlayer, inducing structural disorder [55, 56]. The likely result of using such solvents is a decrease in domain sizes on the large terraces [14]. The voltammetric curve of HDT formed from octanolic solution is similar to that in Figure 1B - only one desorption wave is observed in the forward and reverse scans. These results provide additional evidence that the origin of the fine structure in the voltammetric desorption waves of long chain alkanethiolate monolayers chemisorbed at annealed Au/mica arises from the degree of ordering in the adlayer.

4. Conclusions

The results in this paper demonstrate the role of cohesive interactions and adlayer ordering on the formation of domains of different sizes which contribute to the multiple voltammetric desorption waves for long chain alkanethiolates on annealed Au/mica. Importantly, the key difference between the two types of substrates is the difference in the size of atomically smooth terraces. Long chain alkanethiolate monolayers formed on surfaces with small Au(111) terraces, such as TSG, are composed of smaller domains since the ultimate size of the domains is limited by the size of the terraces. On the other hand, long chain alkanethiolate monolayers on a surface with large Au(111) terraces, such as annealed Au/mica, form larger domains than those at TSG. This difference manifested itself in the difference in the voltammetric curves in Figures 1 and 2. Perhaps the more interesting question to be addressed is how such subtle differences in surface microstructure can influence the ability of these adlayers to form aggregates that are confined for detectable periods of time within the double layer.

Acknowledgments

Discussions with Chuan-Jian Zhong are gratefully acknowledged. This work was supported by the Office of Basic Energy Sciences, Chemical Science Division of the US Department of Energy. Ames Laboratory is operated for the US Department of Energy by Iowa State University under Contract No. W-7405-eng-82.

References

[1] T. W. Schneider and D. A. Buttry, J. Am. Chem. Soc., 115 (1993) 12391.

[2] Y. Sato and F. Mizutani, Electroanalysis, 10 (1998) 633.

[3] M. Nishizawa, T. Sunagawa and H. Yoneyama, J. Electroanal. Chem., 436 (1997) 213.

[4] J. J. Calvente, Z. Kovacova, M. D. Sanchez, R. Andreu and W. R. Fawcett, Langmuir, 12 (1996) 5696.

[5] S.-I. Imabayashi, M. Iida, D. Hobara, Z. Q. Feng, K. Niki and T. Kakiuchi, J. Electroanal. Chem., 428 (1997) 33.

[6] S.-I. Imabayashi, D. Hobara, T. Kakiuchi and W. Knoll, Langmuir, 13 (1997) 4502.

[7] D.-F. Yang, C. P. Wilde and M. Morin, Langmuir, 13 (1997) 243.

[8] D.-F. Yang, H. Al-Maznai and M. Morin, J. Phys. Chem. B, 101 (1997) 1158.

[9] D. Hobara, K. Miyake, S.-I. Imabayashi, K. Niki and T. Kakiuchi, Langmuir, 14 (1998) 3590.

[10] D.-F. Yang, C. P. Wilde and M. Morin, Langmuir, 12 (1996) 6570.

[11] D.-F. Yang and M. Morin, J. Electroanal. Chem., 429 (1997) 1.

[12] D.-F. Yang and M. Morin, J. Electroanal. Chem., 441 (1998) 173.

[13] M. Byloos, H. Al-Maznai and M. Morin, J. Phys. Chem. B, 103 (1999) 6554.

[14] R. Yamada, H. Sakai and K. Uosaki, Chem. Lett. (1999) 667.

[15] H. Azehara, S. Yoshimoto, H. Hokari, U. Akiba, I. Taniguchi and M. Fujihira, J. Electroanal. Chem., 473 (1999) 68.

[16] J. Liu and A. E. Kaifer, Isr. J. Chem., 37 (1997) 235.

[17] L. Zhang, T. Lu, G. W. Gokel and A. E. Kaifer, Langmuir, 9 (1993) 786.

[18] C.-J. Zhong and M. D. Porter, J. Electroanal. Chem., 425 (1997) 147.

[19] C. A. Widrig, C. Chung and M. D. Porter, J. Electroanal. Chem., 310 (1991) 335.

[20] C.-J. Zhong, J. Zak and M. D. Porter, J. Electroanal. Chem., 421 (1997) 9.

[21] M. M. Walczak, C. A. Alves, B. D. Lamp and M. D. Porter, J. Electroanal. Chem., 396 (1995) 103.

[22] D. E. Weisshaar, M. M. Walczak and M. D. Porter, Langmuir, 9 (1993) 323.

[23] D. Hobara, M. Ota, S.-I. Imabayashi, K. Niki and T. Kakiuchi, J. Electroanal. Chem., 444 (1998) 113.

[24] M. Hegner, P. Wagner and G. Semenza, Surf. Sci., 291 (1993) 39.

[25] P. Wagner, M. Hegner, H.-J. Guntherodt and G. Semeza, Langmuir, 11 (1995) 3867.

[26] J. F. Rodriguez, T. Mebrahtu and M. P. Soriaga, J. Electroanal. Chem., 233 (1987) 283.

[27] J. F. Rodriguez and M. P. Soriaga, J. Electroanal. Chem., 135 (1988) 616.

[28] G. M. Berry, B. G. Bravo, M. E. Bothwell, G. J. Cali, J. E. Harris, T. Mebrahtu, S. L. Michelhaugh, J. F. Rodriguez and M. P. Soriaga, Langmuir, 5 (1989) 707.

[29] R. Adzic, E. Yeager and B. D. Cahan, J. Electrochem. Soc., 121 (1974) 474.

[30] A. Hamelin, J. Electroanal. Chem., 165 (1984) 167.

[31] A. Hamelin and J. Lipkoski, J. Electroanal. Chem., 171 (1984) 317.

[32] O. Melroy, K. Kanazawa, J. G. G. II and D. Buttry, Langmuir, 2 (1986) 697.

[33] R. Parsons and G. Ritzoulis, J. Electroanal. Chem., 318 (1991) 1.

[34] J. W. Schultze and D. Dickertmann, Surf. Sci., 54 (1976) 489.

[35] C. A. McDermott, M. T. McDermott, J.-B. Green and M. D. Porter, J. Phys. Chem., 99 (1995) 13257.

[36] G. E. Poirier and M. J. Tarlov, Langmuir, 10 (1994) 2853.

[37] C. Schonenberger, J. Jorritsma, J. A. M. Sondag-Huethorst and L. G. J. Fokkink, J. Phys. Chem., 99 (1995) 3259.

[38] E. Delamarche, B. Michel, H. Kang and C. Gerber, Langmuir, 10 (1994) 4103.

[39] S. A. Cochran and H. H. Farrell, Surface Chemistry, 95 (1980) 359.

[40] Y. Kuk and P. J. Silverman, Appl. Phys. Lett., 48 (1986) 1597.

[41] M. E. Taylor, B. Golen, A. W. McKinnon, G. C. Rosolen, S. M. Gray and M. E. Welland, Appl. Surf. Sci., 67 (1993) 228.

[42] Z. Nawaz, T. R. I. Cataldi, J. Knall, R. Somekh and J. B. Pethica, Surf. Sci., 265 (1992) 139.

[43] G. Reiss, J. Vancea, H. Wittmann, J. Zweck and H. Hoffmann, J. Appl. Phys., 67 (1990) 1156.

[44] D. M. Kolb, J. Vac. Sci. Technol. A, 4 (1986) 1294.

[45] G. E. Poirier and M. J. Tarlov, J. Phys. Chem., 99 (1995) 10966.

[46] G. E. Poirier, Langmuir, 15 (1999) 1167.

[47] S. H. Yalkowsky and S. Banerjee, (Eds.), Aqueous Solubility - Methods of Estimation for Organic Compounds, Marcel Dekker, New York, 1992, Chapter 3.

[48] C. A. Widrig, C. A. Alves and M. D. Porter, J. Am. Chem. Soc., 113 (1991) 2805.

[49] K. Uosaki, Y. Shen and T. Kondo, J. Phys. Chem., 99 (1995) 14117.

[50] G. E. Poirier and E. D. Pylant, Science, 272 (1996) 1145.

[51] G. E. Poirier, Chem. Rev., 97 (1997) 1117.

[52] E. Delamarche and B. Michel, Thin Solid Films, 273 (1996) 54.

[53] E. Delamarche, B. Michel, H. A. Biebuyck and C. Gerber, Adv. Mater., 8 (1996) 719.

[54] P. Fenter, P. Eisenberger and K. S. Liang, Phys. Rev. Lett., 70 (1993) 2447.

[55] C. D. Bain, E. B. Troughton, Y.-T. Tao, J. Evall, G. M. Whitesides and R. G. Nuzzo, J. Am. Chem. Soc., 111 (1989) 321.

[56] R. L. McCarley, Y.-T. Kim and A. J. Bard, J. Phys. Chem., 97 (1993) 211.

Table 1. Reductive desorption peak potentials (E_{rd}, V), oxidative redeposition peak potentials (E_{od}, V), reductive desorption charges (Q_{rd}, $\mu C/cm^2$), and oxidative redeposition charges (Q_{od}, $\mu C/cm^2$) of hexadecanethiolate (HDT) and octadecanethiolate (ODT) monolayers formed on annealed Au/mica and TSG.

Substrate	HDT				ODT			
	E_{rd}[a]	E_{od}[a]	Q_{rd}[b]	Q_{od}[b]	E_{rd}[a]	E_{od}[a]	Q_{rd}[b]	Q_{od}[b]
Annealed Au/mica	-1.11, -1.15	-0.90, -0.96	104 ±11	78 ±7	-1.12, -1.19	-0.90, -1.01	98 ±6	63 ±3
TSG	-1.12	-0.94	98 ±8	65 ±7	-1.15	-0.98	90 ±11	64 ±13

[a]Uncertainties in the peak positions of the desorption and redeposition waves are ±10 mV and are based on at least five replicate experiments with each type of substrate.

[b]The values of Q_{rd} or Q_{od} are calculated using the areas under the waves after compensation for charging current. Roughness factors are not included in the calculation. The uncertainties are based on five replicate experiments.

Table 2. Morphological characteristics of uncoated gold films at annealed Au/mica and TSG based on electrochemical surface area measurements and scanning tunneling microscopy (STM).

Substrate	Electrochemical Roughness Factors (RF)	STM	
		Terrace Size (diameter)	STM Roughness Factors[a] (RF)
Annealed Au/mica	1.1 ±0.1	150 - 200 nm	1.01 ±0.01
TSG	1.3 ±0.1	50 - 80 nm	1.02 ±0.02

[a]STM roughness for each sample was determined by ratioing the actual surface area of an image to its geometric area using the roughness analysis function of the Digital Instruments Nanoscope III software. Ten samples are used to calculate each RF.

Figure Captions

Figure 1. Current-potential curves for the reductive desorption and oxidative redeposition of monolayers formed from HDT on (A) annealed Au/mica and (B) TSG. Electrolyte: 0.5 M KOH. Scan rate: 50 mV s^{-1}.

Figure 2. Current-potential curves for the reductive desorption and oxidative redeposition of monolayers formed from ODT on (A) annealed Au/mica and (B) TSG. Electrolyte: 0.5 M KOH. Scan rate: 50 mV s^{-1}.

Figure 3. STM images (5 μm x 5 μm) of (A) annealed Au/mica and (B) TSG. The corresponding cross-sectional contours for the dashed lines are shown below each image.

Figure 4. STM images (500 nm x 500 nm) of (A) annealed Au/mica and (B) TSG. The corresponding cross-sectional contours for the dashed lines are shown below each image.

Figure 5. Voltammograms for the stripping of underpotentially deposited lead from (A) annealed Au/mica, and (B) TSG. The deposition solution is 1 mM PbO in 1 M $HClO_4$. The scan rate was 20 mV s^{-1}.

Figure 6. Schematic depiction of long-chain alkanethiolates adsorbed on the (111) terraces of (A) annealed Au/mica and (B) TSG. (A) Large terrace with large and small thiolate domains, and thiolates located at domain boundaries. (B) Smaller thiolate domains and thiolates located at the domain boundaries of three smaller terraces separated by steps.

Figure 7. Current-potential curves for the reductive desorption and oxidative redeposition of HDT monolayers on annealed Au/mica: (A) sample was heated at 100°C in air for 4 hr, and (B) same treatment as (A), but reimmersed in an ethanolic solution of HDT for 2 hr. Electrolyte: 0.5 M KOH. Scan rate: 50 mV s^{-1}.

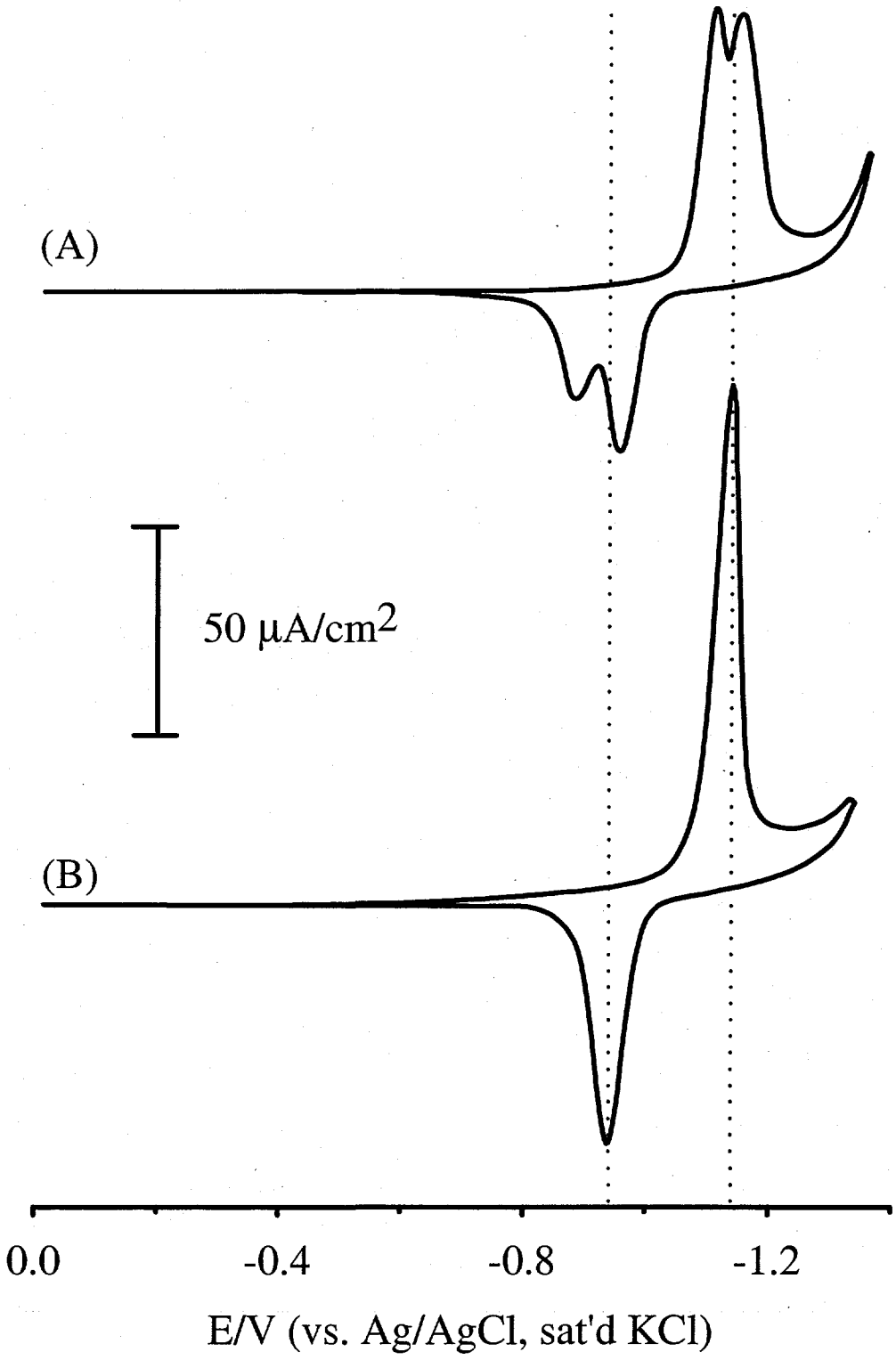

Figure 1

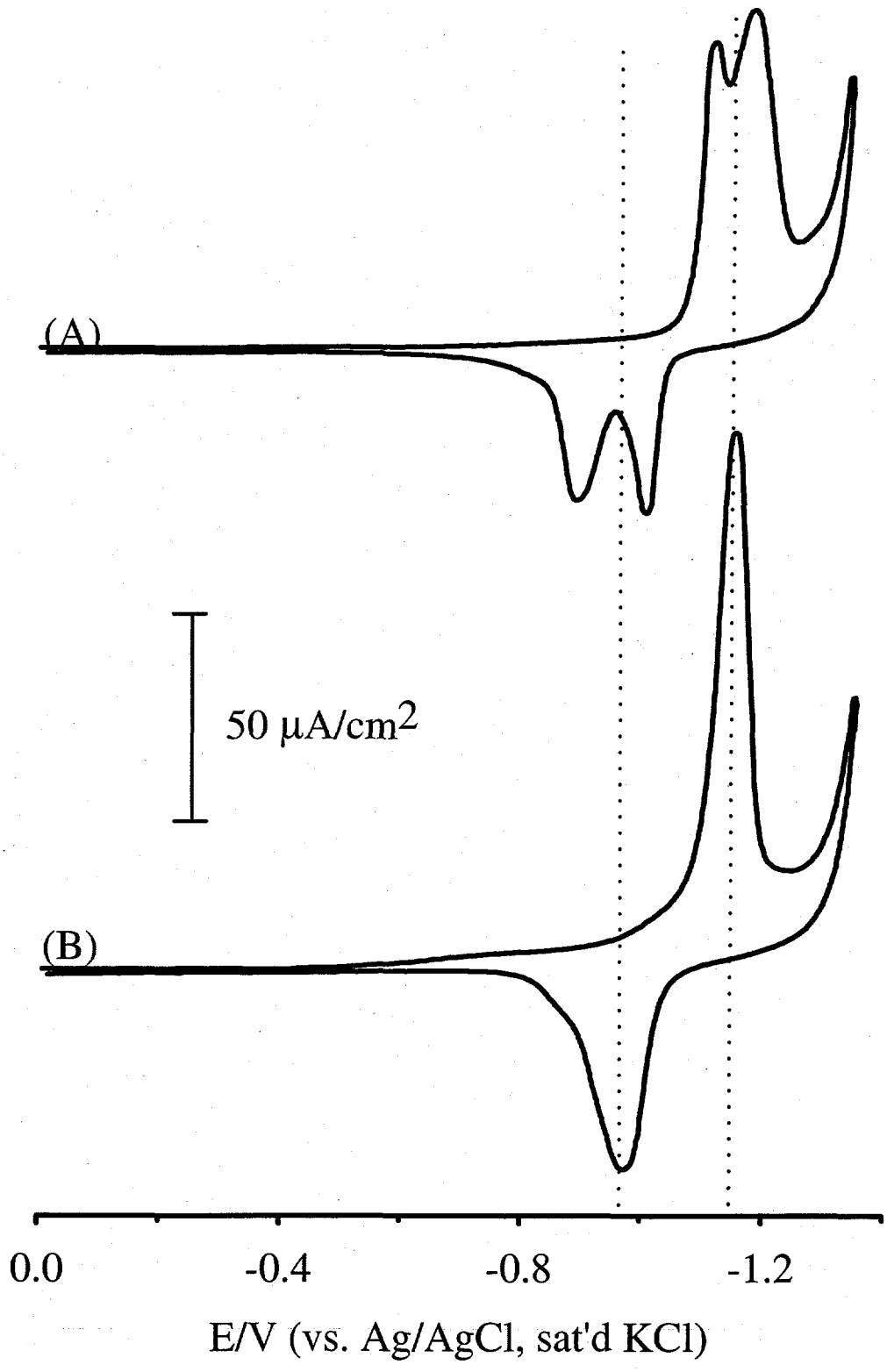

Figure 2

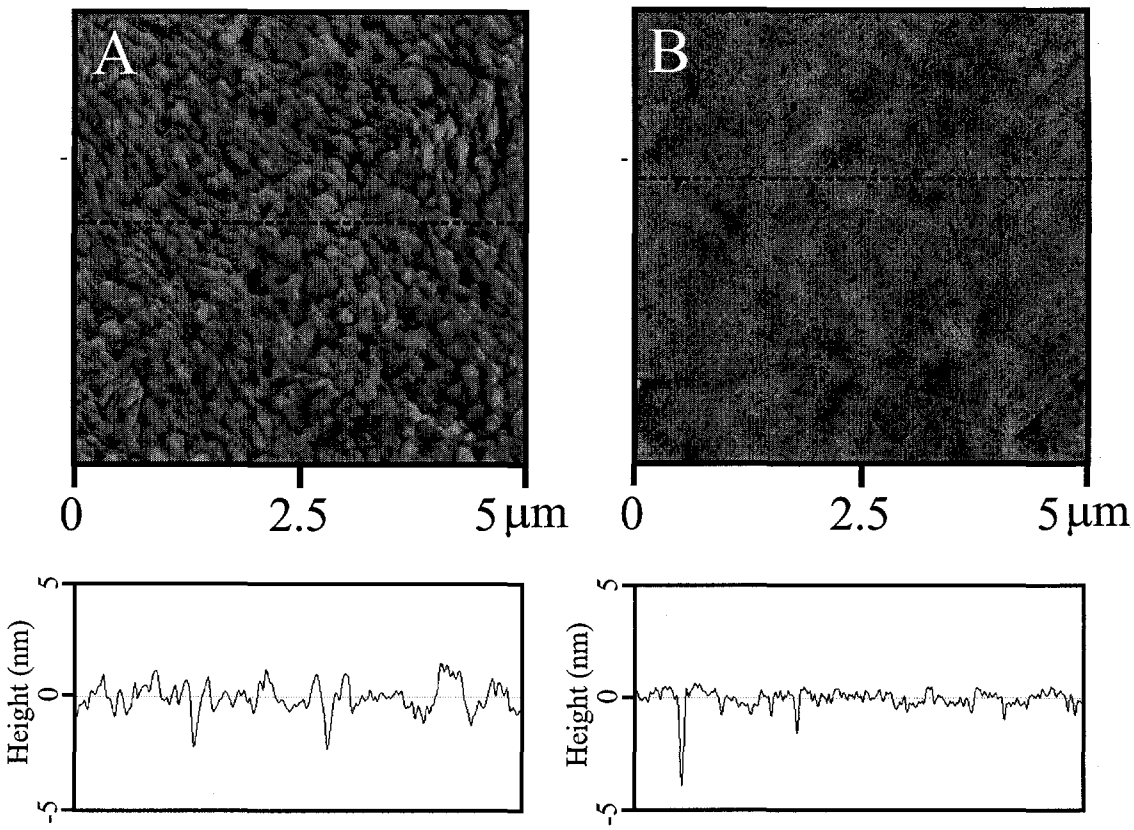

Figure 3

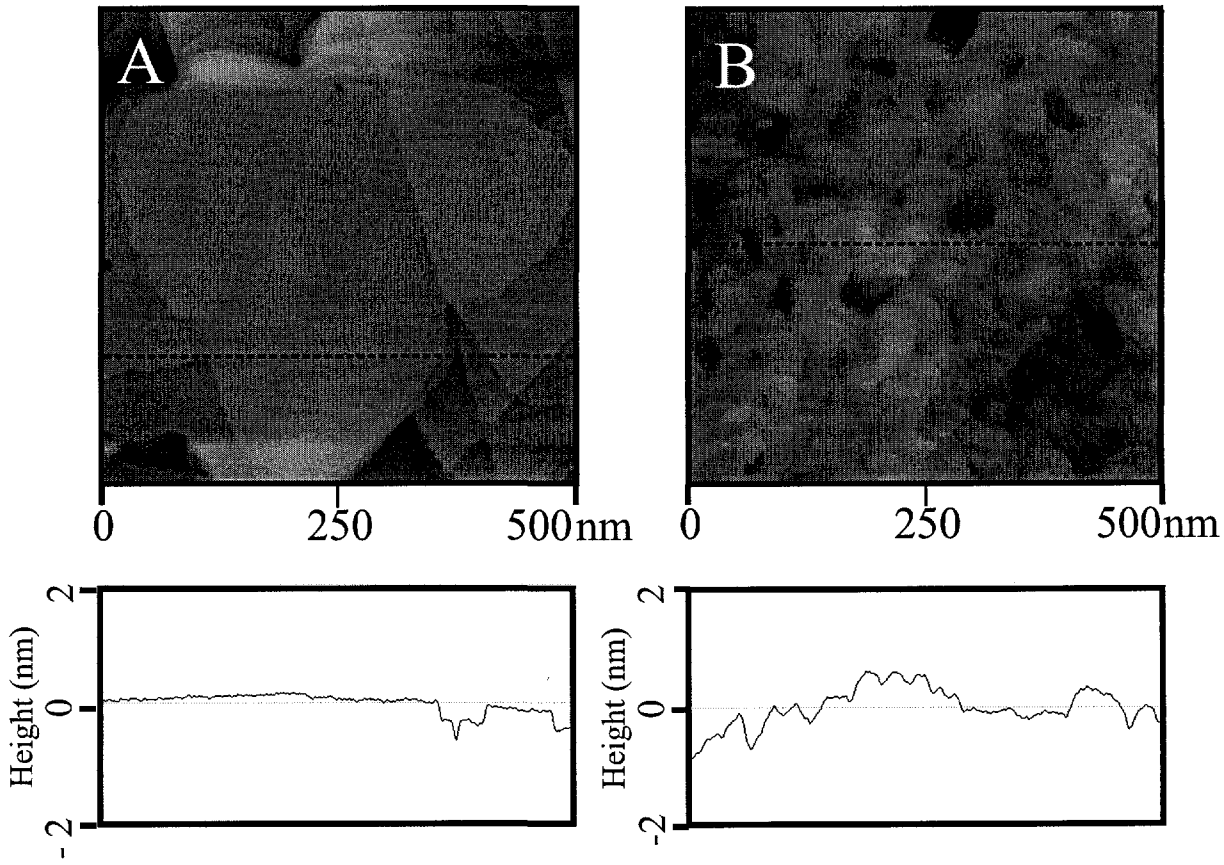

Figure 4

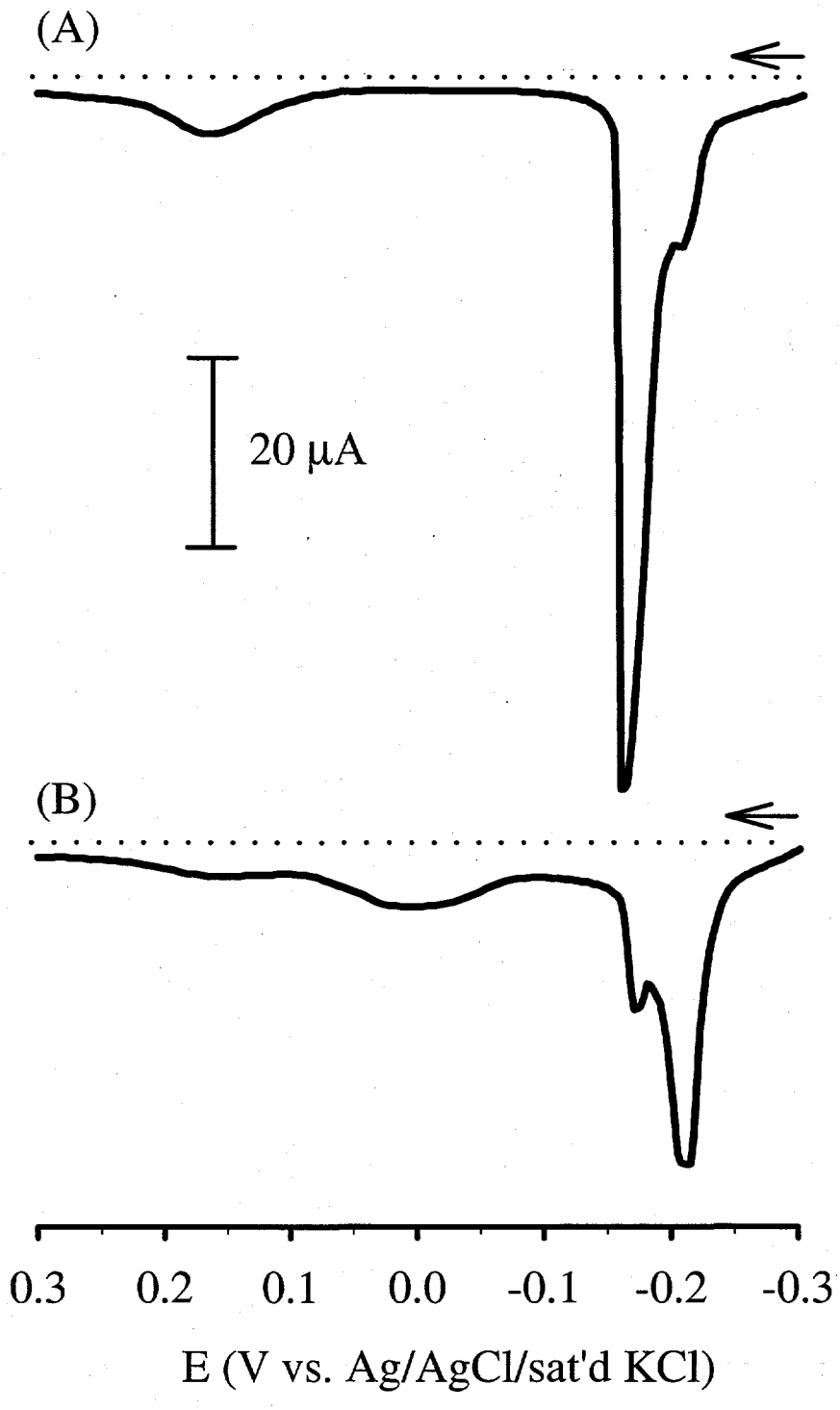

Figure 5

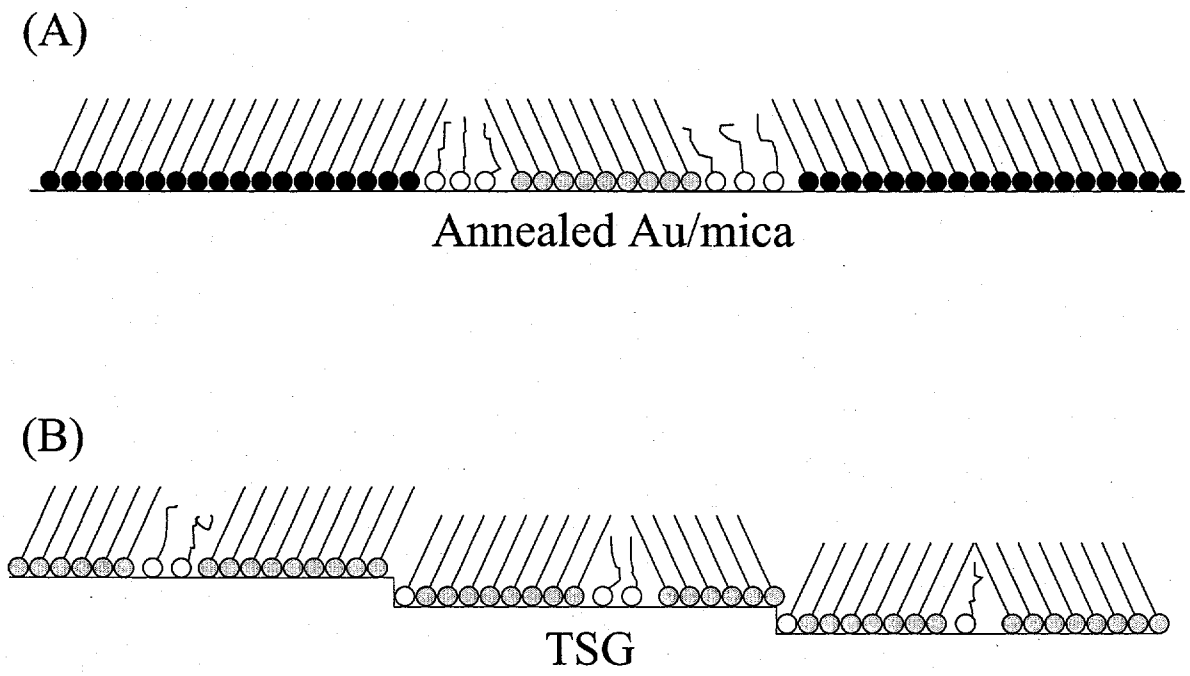
(A)
Annealed Au/mica
(B)
TSG
Thiolates at large domains
Thiolates at small domains
Thiolates at domain boundaries
Thiolates at step sites

Figure 6

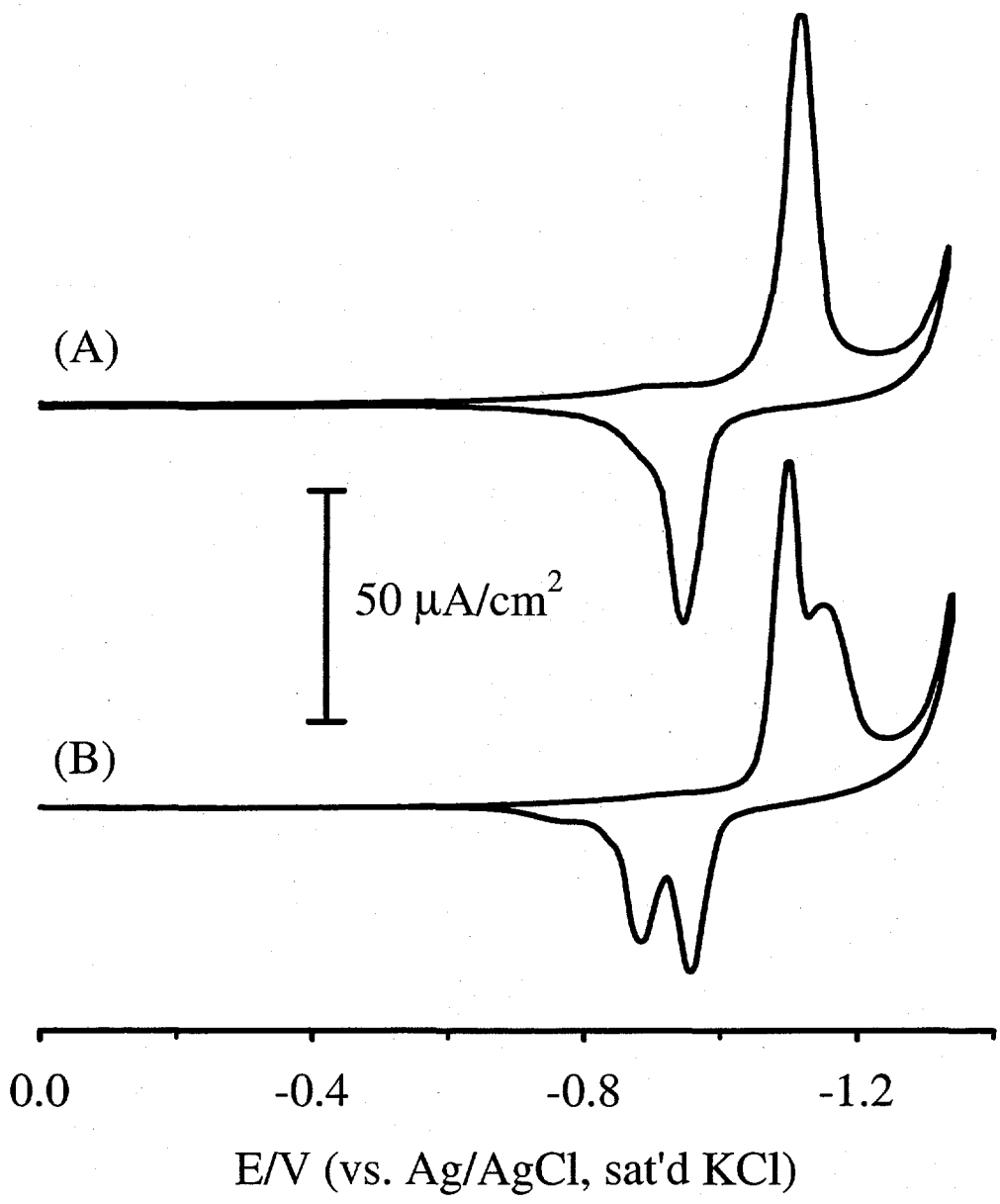

Figure 7

CHAPTER 3. MULTI-TECHNIQUE CHARACTERIZATION OF MIXED MONOLAYERS FORMED FROM SPONTANEOUSLY ADSORBED ORGANOTHIOLATE ASSEMBLIES AT Au(111)

A paper to be submitted to *Journal of Electroanalytical Chemistry*

Sze-Shun Wong, Chuan-Jian Zhong, and Marc D. Porter

Abstract

This paper presents the results from a multi-technique characterization of the mixing characteristics of two-component monolayers formed on Au(111) from dilute ethanolic solutions of both 4-mercaptobenzoic acid (MBA) and hexanethiol (HT). Infrared reflection absorption spectroscopy (IRRAS) data indicate that the surface composition gradually changes from MBA dominated to HT dominated over the immersion time. Results from voltammetric reductive desorption of the monolayers are consistent with the infrared data. By investigating the voltammetric behavior of the mixed monolayers, the negative shift in peak potential (E_p) of MBA desorption as a function of immersion time suggests that the micro environment of MBA changes from a phase separated domain structure to a more homogeneously mixed feature. This evolution was confirmed by using scanning tunneling microscopy to probe the nanoscale spatial distributions of the two surface bound components. These results reveal that the two-component adlayer evolves from a phase separated structure towards a homogeneously distributed surface structure upon extensive immersion in precursor solution. The implications of our findings to the design of architectures prepared by co-assembly are discussed.

1. Introduction

In the past few years, interest in spontaneously adsorbed monolayers formed at gold or silver electrodes from alkanethiols has grown at an explosive rate [1-5]. The driving force of such growth stems from both the ease of preparation and the comparatively well-defined structures of the resulting interfaces.

A thiol-based monolayer usually consists of a head-group of gold or silver-thiolate bond, an organic spacer, and an end-group. Many studies have been conducted to characterize the monolayers with different chemistry in the organic spacer [6] and the end-group regions[7-16]. The techniques used to probe the monolayer architectures vary widely. For example, infrared reflection absorption spectroscopy (IRRAS) probes the local environment and spatial arrangement of the monolayers [17-21]. Electrochemistry probes the strength of the gold or silver-thiolate bond and the extent of the cohesive interactions between neighboring molecules [22-27]. Scanning probe microscopy probes the two-dimensional arrangement of the adlayer molecules [28] and their physical properties (e.g., friction and wear) at a nanometer length scale [9, 10, 14, 15, 29-32]. The wealth of information on these systems that has been obtained through such variety of techniques has also allowed scientists to gain control of specificity and the extent of interactions between an analyte and a modified surface for building sensors and in other areas of application [1, 3].

Motivated by the success of single-component monolayer investigations, applications have recently explored the interfacial properties of two-component assemblies [13, 31-56] as

a means to construct modified electrode surfaces for use in molecular recognition [36] and other types of detection schemes [33, 38, 39, 57]. Central to such efforts is the question of whether such assemblies form as phase separated or homogeneously distributed architectures. Whitesides and co-workers examined two-component monolayers of alkanethiolates on gold [8, 12, 47, 58], and concluded that a single phase is preferred at equilibrium, and phase separations are not observed [7, 18, 47, 58]. Weiss and co-workers showed that two very similar thiolate molecules could phase separate under ambient conditions into nanometer scale domains with time-dependent shapes [45]. Sasabe and co-workers used scanning force microscopy (SFM) to show that domains form at the early stages of mixed monolayer growth [43]. Recently, Shannon and co-workers concluded that the size and distribution of thiolates could be controlled through a combination of precursor composition and concentration [32].

In this paper, we investigate the phase behavior of two-component monolayers derived from a mixture of 4-mercaptobenzoic acid (MBA) and hexanethiol (HT) precursors in ethanolic solutions on Au(111) surface. Illustrated in Figure 1 are two extreme cases differing in their degree of mixing for MBA/HT mixed monolayers. The first case is a phase separated monolayer where individual islands of MBA and HT exist on the Au(111) terraces. Each of the islands exhibits the characteristics of the respective single-component monolayer. The other is a case of a homogeneously mixed monolayer where the two components are randomly distributed on the surface. We have used infrared reflection adsorption spectroscopy (IRRAS), cyclic voltammetry (CV), and scanning tunneling microscopy (STM) to provide in-depth examinations of the mixed monolayer surfaces and the spatial distribution

of the MBA and HT adsorbates. The following sections describe the results of our investigation. These results provide evidence that a phase separated monolayer of MBA and HT can evolve toward a homogeneously distributed structure.

2. Experimental

2.1 Gold substrate preparation

Substrates were prepared by vapor deposition of ~300 nm of gold onto fleshly cleaved mica (B & M Trading Inc.) at ambient temperatures. The deposition rate was ~0.3 nm/s. The pressure in the cryopumped Edwards E360A coating system during evaporation was less than 9×10^{-5} Pa. Substrates were then annealed at 300°C for 5 hours in a muffle furnace; this process yields a surface composed of large (>100 nm^2), atomically smooth Au(111) crystallites [24].

2.2. Monolayer film preparation

Ethanol (Quantum, punctilious grade), HT (Aldrich), and MBA (Toronto Research Chemicals Inc.) were used as received. One-component monolayers were prepared by immersing gold substrates in 1 mM ethanolic solutions of either HT or MBA. Mixed component monolayers of MBA and HT (MBA/HT) were formed from ethanolic solutions of MBA and HT at a desired ratio R (where $R = [MBA]_{sol}/[HT]_{sol}$) while keeping the total concentration of thiols to 1 mM. Immersion times were carefully controlled and their effects

on relative coverages were studied. After removal from solution, the samples were rinsed with copious amounts of ethanol and dried under a stream of high purity argon.

2.3 Characterization with infrared reflection adsorption spectroscopy (IRRAS)

IRRAS spectra were acquired with a Nicolet 750 FT-IR spectrometer. Monolayer spectra used *p*-polarized light incident at 80° from the surface normal and liquid N_2 cooled MTC detector. All spectra were collected with 2-cm^{-1} resolution. The spectra of the surface layers are reported as -log (R / R_o), where R is the reflectance of the sample and R_o is the reflectance of a "reference" octadecanethiolate-d_{37} monolayer on Au. Further details of reference preparation and handling are given elsewhere [59].

2.4 Characterization with cyclic voltammetry

The derivatized electrodes were mounted in a conventional three-electrode cell with an exposed area, defined by an O-ring, of 0.58 cm^2. All potential measurements are reported with respect to an Ag/AgCl /saturated KCl electrode. Deionized water, which was purified by passage through a Milli-Q filtration system, was used for all solution preparations. Electrolyte solutions were prepared with semiconductor grade KOH (99.99%, Aldrich) and were deoxygenated with argon. The cyclic voltammetry of monolayer electrodes was performed by scanning the applied potential at 50 mV/s between -200 mV and -1350 mV using a CV-27 potentiostat (Bioanalytical Systems).

2.5 Characterization with scanning tunneling microscopy (STM)

STM images were obtained under ambient conditions using a Digital Instruments Nanoscope III. The instrument was equipment with a 0.7 μM scanner. The height mode, which maintains a constant current between tip and sample, was utilized for all imaging. The probe tips were fabricated by electrochemically etching a 0.025 cm diameter tungsten wire in 0.5M KOH (99.99%, Aldrich). The typical range of bias potential and set point current used for imaging were 500-100 mV and 500-1000 pA, respectively.

3. Results and discussion

The following sections describe the results of infrared spectroscopic, voltammetric, and scanning tunneling microscopic studies of MBA/HT thiolate monolayers. The primary goal is to determine if adlayers formed from mixed thiol solutions are phase separated, homogeneously distributed architectures, or a combination of both. First, IRRAS was applied to estimate the relative adsorbate coverage as a function of precursor concentrations in the formation solutions. Second, voltammetric data from the electrochemical reductive desorption of the monolayers was employed to determine the fractional surface coverage as a function of immersion time. Finally, scanning tunneling microscopy was used to probe the nanoscale two-dimensional distribution of the two components of the surface structure.

3.1. IRRAS characterization

As a starting point, IRRAS was used to probe the composition and structure of the one-component and two-component monolayers that are formed from ethanolic solutions of MBA, HT, and a mixture of MBA and HT at annealed gold substrates. A set of such spectra is presented in Figure 2, noting that all of these samples were prepared using a 5 min immersion time. Peak positions and band assignments, based on previous reports [17, 20], are listed in Table 1.

Figure 2A shows a spectrum of the monolayer formed from HT, and Figure 2D presents that of the monolayer formed from MBA. Methyl and methylene stretching modes for the alkyl chains are evident between 2800 cm^{-1} and 3000 cm^{-1} for the HT monolayer. In contrast, the spectrum of the MBA monolayer shows a sharp band diagnostic of an unassociated O-H stretch for the carboxylic acid moiety at 3580 cm^{-1}, an asymmetrically shaped band indicative of the carbonyl stretch for a carboxylic acid at 1749 cm^{-1}, whereas the ν(C=C) bands at 1588 and 1480 cm^{-1}, and the δ(C-H) bands at 1173, 1093, and 1015 cm^{-1} are indicative of an aromatic ring. The small, low-energy shoulder of the 1749 cm^{-1} band indicates that a relatively small amount of the carboxylic acid groups is hydrogen-bonded to neighboring groups. Since the ν(O-H) band at 3580 cm^{-1} and the ν(C=O) band at 1750 cm^{-1} are diagnostic of an unassociated, protonated carboxylic acid, while the strong aromatic ring mode at 1588 cm^{-1} indicates that the average alignment of the plane of the aromatic ring is along the surface normal, the MBA absorbates are expected to be oriented close to surface normal [20].

The spectra of monolayers (Figure 2B and 2C) formed from a mixture of MBA/HT have the characteristics of each component. The methyl and methylene stretches of HT between and the O-H, C=O, and C=C stretches of MBA are all present in the mixed monolayer spectra. Assuming that the orientation of each component in the adlayer is independent of relative coverage, the intensity of those peaks is proportional to the respective amount of each component on the monolayer surfaces. When spectra with R=100 and 1 are compared, a 100 times increase in the relative concentration of MBA with respect to HT results in only a 2 to 3 times increase in the free O-H stretch at 3580 cm^{-1} and the carbonyl stretch at 1750 cm^{-1}. It is therefore clear that HT is preferentially adsorbed onto the gold surface.

We next briefly investigated how the relative composition of the precursor solution and immersion time affects the relative surface coverage. Figure 3 shows the absorbance of the symmetric methyl stretch at 2877 cm^{-1} from two-component samples immersed in solutions of differing values of R and for an immersion time of either 15 or 90 min. The dashed line in the plot represents the ideal case when there is no preferential adsorption of either precursor and the concentration ratios of the two surface-bound thiolates equal their ratios in the formation solution. Comparing the three plots again shows that HT is preferentially adsorbed over MBA onto the Au(111) surface. Preferential adsorption [7, 47, 60] of one precursor over the other is possibly due to the lower solubility in ethanol, a stronger gold-thiolate bond, and higher intermolecular interactions between the tail groups for the former. In addition, the surface composition was not significantly affected by the

differences in the two immersion times selected (15 and 90 min). We note that the same type of plots, but with opposite trend were obtains when the intensity of the C=C stretch at 1588 cm^{-1} from the spectra, or the capacitance of the monolayer electrodes were plotted against R. Implications of these findings will be discussed in a subsequent section.

3.2 Determination of fractional surface coverages by cyclic voltammetry

3.2.1 General voltammetric characteristics as a function of precursors concentration

Voltammetric reductive desorption can be used to determine the relative surface coverages of these types of adlayers [61]. The amount of each component on a surface is directly proportional to the integrated charges under its respective desorption peak [56, 61]. The voltammetric curves recorded were also used to study the interaction between the two components on the surface by comparing the peak reductive desorption potentials of the components to that of the single component analogs [51, 62]. The peak potential (E_p) for the desorption waves of each component is diagnostic of the relative strength of the gold-thiolate bond [22, 24] coupled with the strength of the interactions between the neighboring molecules [23, 63].

Figure 4 is a set of voltammetric curves from these experiments. The bottom two overlapping curves are from single-component MBA and HT monolayers and are used as reference points. The dominant wave in each of the single-component monolayers represents the desorption of thiolates at the Au(111) terraces [63]. The values of E_p of MBA and HT are -580 mV and -880 mV, respectively. In addition, we often observed a much smaller wave

near -940 mV for the reductive desorption of MBA. We believe this wave is associated with the presence of gold-bound atomic and/or oligomeric sulfur species [64]. These waves, located near -940 mV, are different from those from desorption of thiolates from step sites, which are usually observed at ~200 mV more negative than the dominant desorption wave [63].

The voltammetric wave of a mixed monolayer (top) (R=19; 15 min immersion) shows that the reductive desorption waves of MBA and HT appear at potentials intermediate to the diagnostic waves of the single-component analogs. The E_p of the MBA component is negative of that of a single-component MBA monolayer, whereas the E_p of the HT component is positive of that of a single-component HT monolayer. It is therefore more difficult to reductively desorb MBA but easier to desorb HT in a mixed monolayer environment compared to their respective adsorbates in a single-component environment. This result suggests that the two components of the adlayer have mixed to an undefined extent [51]. In addition, the widths of the desorption waves of the mixed monolayer are slightly larger than those of either single-component monolayer. These increases suggest that either the strength of the cohesive interactions between the molecules of same species are less than that of a single-component monolayer or that the distribution of the cohesive interactions has increased [65].

Small waves resulting from the oxidative re-adsorption of the desorbed thiolates were also observed at the MBA and HT coated electrodes during the reverse potential scan following the reductive desorption. The deposition wave for MBA is, however, smaller than

that for HT. This difference is attributed to the higher solubility of the desorbed dianionic MBA in aqueous alkaline electrolyte, which results in the greater diffusional loss of MBA before reaching the applied potential to initiate its deposition.

Voltammetric reductive desorption was conducted on electrodes immersed for 5 min in solutions with different R values and a set of voltammetric curves for electrodes with R values of 0 (HT only), 1, 9, 19, and ∞ (MBA only) are shown in Figure 5. As expected, the size of the MBA desorption wave decreases while that of HT increases as R decreases. Two distinct and well separated desorption waves that exhibit small shifts in E_p are observed when $R > 5$ (data not shown). With $R < 5$, the voltammetric response becomes more complex. The changes show that the MBA desorption process is shifted to a more negative applied potential, and begins to merge with the HT wave when $R < 1$. The shift for MBA suggests a different local environment for MBA absorbates when its coverage becomes comparatively low [51]. The voltammetric curves also provide evidence of preferential adsorption of HT. For example, the curve with R=1 has a major desorption wave that originates from HT.

3.2.2. Voltammetric characteristics as a function of immersion time

The 5-minute immersion results with R=19 show that the two-component adlayer exhibits well-separated waves but not a component preference. We selected this R value for the following studies because other R values tended to create mixed monolayers with a dominant component, complicating a ready assessment of whether the layers mix or phase separate. In addition, as will become clearer later in the sections, immersion time is also an

important factor in determining the final composition of mixed monolayers. Mixed monolayers created with other R values in the last section produces voltammetic waves dominated by one component at very short immersion time, making the time dependent study very difficult. Also, a surface dominated by either one component makes studies, such as identifying the minor adsorbates spatially by STM, very challenging, if not impossible.

Figure 6 shows the voltammetric characteristics of the mixed monolayer as a function of immersion time in R=19 solution. The first notable difference in the voltammetric curves is that the magnitudes of the MBA and HT waves change over time. The relative amount of each component in the adlayer is therefore immersion-time dependent. Though quantitative assessment is complicated by the multiplicity and superposition of the waves, the integrated charge under each wave in Figure 6 was estimated and is presented in Table 2. We note that as with other measurements of integrated charge under reductive desorption waves, the variability is usually ~10% and the values should only be examined qualitatively.

At short immersion times, the adlayer is dominated by MBA. As immersion time increases, however, the adlayer slowly becomes HT dominated with time. This evolution suggests that monolayer formation is dynamic and exchange-replacement between absorbates and solution precursors continues to occur while the substrate is immersed in the formation solution. Based on these data, we conclude that the kinetics of adsorption and/or of transport to the electrode surface control the composition of the initially formed monolayer. The chain length-related intermolecular forces, solubility factors, and possibly the stronger gold-thiolate bonds that drive preferential adsorption of HT have relatively little effect on the composition

of the initially formed monolayer. Preferential adsorption, due to intermolecular forces, however, starts to become notable as immersion time increases and the adsorbates undergo a slow exchange with the precursors in solution. The voltammetric curves between immersion times of 210 min and 161 hr demonstrate this transformation.

Another feature obtained from the voltammetric curves of mixed monolayers is the appearance of a shoulder approximately 50 mV more negative than the main HT peak. We consistently observe such a wave in mixed monolayer reductive desorption voltammetric curves. We do not understand its origin, but suspect that the wave is also from the desorption of HT. We speculate that such distinct HT waves reflect a subtle difference in binding strength of the HT at gold or in the local environment of the mixed monolayers.

Besides an increase in relative HT coverage, the voltammetric curves show that the E_p of MBA significantly shifts to more negative values over time. As immersion time increases, the MBA wave shifts negatively until merging with the HT wave. The overall shift is more than 150 mV.

While the E_p of MBA changes dramatically, the E_p of HT (-880 mV from a single-component monolayer) shifts a much smaller amount. These shifts yield a wave at a position (~825 mV) similar to that observed in the second scan of a single-component HT monolayer which we attribute to the presence of a less densely packed HT adlayer. The following proposes a mechanism to explain these shifts.

First, at short immersion times (e.g., 1 min), the kinetics of adsorption due to high mole concentration ratio of MBA to HT (19:1) controls the surface composition. As a result,

the surface is dominated by MBA as shown by the voltammetric curves in Figure 6A and by the illustration in Figure 7A. The MBA adsorbates are surrounded mainly by neighboring MBA adsorbates, thus the individual domains of the mixed monolayer have a similar environment (e.g., electrolyte permeability) to that that of the single-component MBA monolayer. As a result, the voltammetric reductive desorption of MBA behaves as if there is only one component on the surface, and the voltammetric curve for MBA in the mixed adlayer resembles that of a single-component MBA monolayer. We note that the E_p (-540 mV) of MBA with 1 min immersion was more positive than that of the reference data in Figure 4. This difference is probably due to the fact that a well-packed monolayer has not yet formed with such a short immersion time [66] and a less negative potential is required to achieve reductive desorption.

For samples with immersions of 15 min (Figure 6B), the adlayer is now composed of both of MBA and HT at comparable amounts as suggested by the voltammetric curve. The MBA adsorbates are essentially phase-separated from and surrounded by HT domains on surface as illustrated in Figure 7B. The dramatic change in surface composition between 1-min and 15-min immersion is realized by the fact that the surface at 1 min immersion is occupied mainly by MBA is not well organized and exists as a loosely-packed monolayer. This low level of packing leaves voids for HT adsorption; exchange may also occur. These two processes take place rapidly when the adlayer is loosely packed, but slows down as coverage increases.

The voltammetric curve in Figure 6B shows that E_p of MBA with 15-min immersion (-650 mV) is now more negative than that of a single-component MBA monolayer. This shift is indicative of a change in the spatial distribution of the MBA adsorbates in the mixed monolayers [62]. While some of the MBA absorbates form island-like structure on the surface, others may be well mixed with the HT adsorbates. Therefore, the MBA local environment is now modified and becomes more HT-like. The presence of HT in MBA and vice versa changes the microenvironment and the accessibility of electrolyte ions for reductive desorption. In the case of MBA, the adsorbates in a mixed monolayer are stabilized against reductive desorption through either the affinity between the MBA and HT which results in higher packing density, and/or an increased resistance towards the permeation of electrolyte ions to the gold surface. As a result of such changes, the reductive desorption of MBA shifts negatively from -580 mV to -650 mV. Meanwhile, the reductive desorption potential of HT adsorbates shift towards more positive values at a less extent (from -880 to -830 mV), indicating a less dissolution of MBA in HT.

At longer immersion times (15-90 min immersion), the preferential adsorption of HT begins to assert itself and becomes as important as the concentration effect of MBA. The net result of these two opposing forces causes the adsorbates to undergo a slow exchange with their precursors in solution. Such exchange is likely to occur primarily at the MBA domain boundaries and, to a lesser extent, within the domains. Importantly, the integrated charges of the MBA and HT waves for the two-component monolayer do not notably change for immersions from 15 to 90 min; even though the wave for MBA continues to move negatively

(from -650 (15 min) to -725 mV (90 min)) as shown in Figures 6B-D. This trend suggests that the exchange-replacement process leads to a more homogeneous mixing of the adsorbates but without any significant change in their relative amounts (illustrated by Figures 7B and 7C). The subtle change in overall composition was confirmed by the IRRAS data shown in Figure 8 which shows that the spectra taken at these two immersion times are essentially identical.

The E_p of HT, however, seems to be unaffected by the surface composition and immersion time except the initial shift from -880 to ~-830 mV. These data suggest two intriguing interpretations. First, HT is soluble in a MBA domain, but MBA is not as soluble in a HT domain. It follows that the intermolecular HT-HT interactions are slightly larger than the HT-MBA interactions, and the MBA-MBA interactions are the weakest of the three. Second, the potential required to desorb HT is not as sensitive to the packing density as that of MBA, even upon the incorporation of MBA into a HT domain. This assertion is supported by the fact that E_p for HT during a second scan of a single-component HT monolayer is also around -830 mV. During such second-scan desorption, the HT monolayer is not well organized and packed- a situation qualitatively analogous to that for HT in the mixed monolayer.

To verify further our interpretation, samples at 15 min immersion time were removed from precursor solution and immersed into neat ethanol for 65 min. The samples were then removed and characterized with cyclic voltammetry. The E_p and integrated charges under the waves for both MBA and HT were the same as those prior to immersion into neat ethanol

(data not shown). This findings argue that the shifts of desorption peaks observed in the time-immersion study do not originate from better organization and packing of the adlayer.

With longer immersions (>2 hr), the preferential adsorption of HT strongly dominates the composition of the resulting adlayer. This situation leads to a slow but continuous replacement of adsorbed MBA by HT from solution and the composition of surfaces is slowly dominated by the presence of HT. The final surface composition is obtained when thermodynamic equilibrium between the monolayers and the adsorption solution is reached (Figure 7D). With long immersion times, the small amount of MBA becomes well-dispersed in the monolayers with HT and its resistance towards reductive desorption is greatly enhanced because of the intermolecular interactions between MBA and HT and the overall interfacial properties which becomes more like that for single-component HT. Such changes are reflected by the continuous negative shift of the MBA wave until it merges with that of the HT (Figure 6F).

3.3. Examination of morphological distribution by scanning tunneling microscopy

Since the voltammetric data has revealed the possibilities of phase-separated adsorbates turning into more homogeneously distributed over the immersion period, scanning tunneling microscopy (STM) was used to image the surface of the mixed monolayer at different immersion times to test our proposed mechanism. Samples from immersion time of 15 and 90 min were examined. These samples were chosen because the voltammetric curves and IRRAS data show that the relative composition of components did not significantly

change over such period. Therefore, the difference in the images observed can be attributed to homogenous mixing rather than a change in composition.

Before imaging noted samples, reference samples of single-component MBA, HT monolayers, and MBA/HT mixed monolayers were prepared and imaged. The mixed monolayer sample was formed by the partial exchange of a HT monolayer with MBA. We expected that the differences in the electronic structure and molecular size would result in a difference in tunneling efficiency that could be used as a contrast mechanism [31]. We note that a typical STM image of a HT monolayer shows the existence of pits near or at the domain boundaries and yields molecular resolution for the adsorbates within the domains [67-69]. At domain boundaries, HT is not as well packed as within domains and appears rougher. Compared to an alkyl chain thiolate monolayer, STM image of a MBA monolayer are usually devoid of pits and difficult to resolve at a molecular scale.

Figure 9 is a STM image of a HT monolayer that has been immersed in a 1mM MBA solution for 120 hr. The purpose of immersing the HT monolayer in a MBA solution is to partially replace the HT adsorbates with MBA precursors to create a mixed monolayer with large domains. By using voltammetric reductive desorption and IRRAS, the presence of the two components was confirmed. The image obtained from this type of mixed monolayer preparation is used as reference for images obtained from mixed monolayer sample formed from mixed precursor solutions.

There are two major features in the image of the mixed monolayer. The first one is the smooth or lower regions where molecular resolution could be obtained if zoomed in and

imaged. We believe such regions are domains of HT adsorbates. The other feature is the rougher and slightly higher areas (~0.1 nm) outside the HT domains. We assign these features to regions occupied mainly by MBA adsorbates replacing HT. Since the image shows that MBA adsorbates reside outside the HT domains, replacement initiates at the domain boundaries of HT where the adsorbates are less packed and more accessible to the precursor in solution. Because molecular resolution was not obtained in the rough regions, we cannot confirm that the areas are composed only of MBA absorbates. Nevertheless, we believe that the majority of the adsorbates in these regions are MBA because of the enhanced image contrast.

Figure 10A is a STM image of a MBA/HT mixed monolayer after 15 min immersion in a R=19 solution. Two regions are evident based on the contrast. Drawing on the STM image from Figure 9, we believe that the high contrast areas are MBA islands or at least areas of adsorbates where MBA is in the majority. The low areas are thereafter assigned as HT islands or areas where HT is in the majority.

Figure 10B is a STM image of MBA/HT mixed monolayer after 90 min of immersion in the same solution. We again see that two regions of differing contrast. Compared to the image in Figure 10A, the high contrast areas (MBA) occupy a much smaller portion of the surface. This decrease is due to homogeneous mixing between adsorbates and precursors. We also believe that the low areas, which were occupied mainly by HT adsorbates at short immersion times, are now composed of HT plus some MBA absorbates again because of the homogeneous mixing process discussed earlier when analyzing results of voltammetric

reductive desorption and IRRAS. This change in distribution of adsorbates should lead to a smaller contrast difference between the two regions. In fact, bearing analysis, which can be used to examine the distribution and relative amounts of areas with contrast differences in an image, has shown that the average height difference between the high and low regions from samples with 15 and 90 min of immersion is 0.1 nm and 0.06 nm, respectively. The decrease in height difference at longer immersion provides further evidence that inhomogeneously mixed monolayers formed at the beginning of an immersion progressively become homogeneously mixed upon extensive immersion in precursor solution.

4. Conclusions

The infrared reflection absorption spectroscopic and voltammetric data have demonstrated that the distribution of adsorbates of the initially formed mixed MBA/HT monolayers is dictated by the kinetics of spontaneous adsorption. The intermolecular forces that drive preferential adsorption of HT have relatively little effect on the composition of the initially formed monolayer. However, such preferential adsorption of HT starts to play a role when the sample is allowed to stay in the precursor solution and adsorbates undergo slow exchange and replacement with thiols in solution. This exchange eventually transforms a surface with one dominant adsorbate species with final equilibrium composition determined by the precursor composition.

While approaching equilibrium in solution, the phase separated mixed monolayer formed at the beginning of an immersion becomes more homogeneously mixed with a

continuous immersion in precursor solution, and during which there is a stage that the overall surface composition remains relatively unchanged. Such a finding, at least from the mixed monolayer system studied here, suggests that the size of islands in mixed monolayers could be controlled by the relative concentration of each component in precursor solutions and by the length of immersion. Further understanding the others factors governing the formation of mixed monolayers will no doubt help controlling the surface specificity in applications relied on the ionic charge [70, 71], hydrophobicity or hydrophilicity [72], size [1, 73-76], and other chemical properties of the adsorbates. Studies focusing on direct observation of such surface specificity (e.g., compositional mapping by SFM [10, 32] or adhesion force measurements [30, 77]) are underway.

Acknowledgment

This work was supported by the Office of Basic Energy Sciences, Chemical Science Division of the US Department of Energy. Ames Laboratory is operated for the US Department of Energy by Iowa State University under Contract No. W-7405-eng-82.

References

[1] A. Ulman, An Introduction to Ultrathin Organic Films: From Langmuir-Blodgett to Self-Assembly, Academic Press, San Diego, 1991.

[2] L. H. Dubois and R. G. Nuzzo, Ann. Rev. Phys. Chem., 43 (1992) 437.

[3] H. O. Finklea, in A. J. Bard, (Ed.) Electroanalytical Chemistry, Vol. 19, Marcel Dekker Inc.: New York, 1996, p. 109.

[4] G. M. Whitesides and P. E. Laibinis, Langmuir, 6 (1990) 87.

[5] C.-J. Zhong and M. D. Porter, Analytical Chemistry (1995) 709.

[6] C. D. Bain and G. M. Whitesides, J. Am. Chem. Soc., 110 (1988) 5897.

[7] C. D. Bain, J. Evall, and G. M. Whitesides, J. Am. Chem. Soc., 111 (1989) 7155.

[8] P. E. Laibinis, M. A. Fox, J. P. Folkers, and G. M. Whitesides, Langmuir, 7 (1991) 3167.

[9] C. D. Frisbie, L. F. Rozsnyai, A. Noy, M. S. Wrighton, and C. M. Lieber, Science, 265 (1994) 2071.

[10] J.-B. D. Green, M. T. McDermott, M. D. Porter, and L. M. Siperko, J. Phys. Chem., 99 (1995) 10960.

[11] E. Delamarche and B. Michel, Thin Solid Films, 273 (1996) 54.

[12] C. D. Bain and G. M. Whitesides, J. Am. Chem. Soc., 110 (1988) 6560.

[13] L. Bertilsson and B. Liedberg, Langmuir, 9 (1993) 141.

[14] M. T. McDermott, J.-B. D. Green, and M. D. Porter, Langmuir, 13 (1997) 2504.

[15] M. O. Finot and M. T. McDermott, J. Am. Chem. Soc., 119 (1997) 8564.

[16] S.-S. Wong, H. Takano, and M. D. Porter, Anal. Chem., 70 (1998) 5209.

[17] M. D. Porter, T. B. Bright, D. L. Allara, and C. E. D. Chidsey, J. Am. Chem. Soc., 109 (1987) 3559.

[18] P. E. Laibinis, R. G. Nuzzo, and G. M. Whitesides, J. Phys. Chem., 96 (1992) 5097.

[19] M. D. Porter, Anal. Chem., 60 (1988) 1143A.

[20] S. E. Creager and C. M. Steiger, Langmuir, 11 (1995) 1852.

[21] S. M. Stole and M. D. Porter, Langmuir, 6 (1990) 1199.

[22] C.-J. Zhong, J. Zak, and M. D. Porter, J. Electroanal. Chem., 421 (1997) 9.

[23] C.-J. Zhong and M. D. Porter, J. Electroanal. Chem., 425 (1997) 147.

[24] C. A. Widrig, C. Chung, and M. D. Porter, J. Electroanal. Chem., 310 (1991) 335.

[25] S. R. Snyder and H. S. White, J. Phys. Chem., 99 (1995) 5626.

[26] D. W. Hatchett, K. J. Stevenson, W. B. Lacy, J. M. Harris, and H. S. White, J. Am. Chem. Soc., 119 (1997) 6596.

[27] Q. Cull, K. J. Stevenson, and H. S. White, Proc. - Electrochem. Soc., 97-17 (1997) 158.

[28] G. E. Poirier, Chem. Rev., 97 (1997) 1117.

[29] R. M. Overney, E. Meyer, J. Frommer, D. Brodbeck, R. Luthi, L. Howald, H.-J. Guntherodt, M. Fujihira, H. Takano, and Y. Gotoh, Nature, 359 (1992) 133.

[30] R. C. Thomas, J. E. Houston, R. M. Crooks, T. Kim, and T. A. Michalske, J. Am. Chem. Soc., 117 (1995) 3830.

[31] T. Takami, E. Delamarche, B. Michel, C. Gerber, H. Wolf, and H. Ringsdorf, Langmuir, 11 (1995) 3876.

[32] W. A. Hayes, H. Kim, X. Yue, S. Perry, and C. Shannon, Langmuir, 13 (1997) *2511.*

[33] C. Cotton, A. Glidle, G. Beamson, and J. M. Cooper, Langmuir, 14 (1998) 5139.

[34] Z. Yang, I. Engquist, B. Liedberg, and J.-M. Kauffmann, J. Electroanal. Chem., 430 (1997) 189.

[35] Z. Yang, I. Engquist, M. Wirde, J.-M. Kauffmann, U. Gelius, and B. Liedberg, Langmuir, 13 (1997) 3210.

[36] L. A. Bumm, J. J. Arnold, M. T. Cygan, T. D. Dunbar, T. P. Burgin, L. Jones, II, D. L. Allara, J. M. Tour, and P. S. Weiss, Science, 271 (1996) 1705.

[37] B. Liedberg and P. Tengvall, Langmuir, 11 (1995) 3821.

[38] G. K. Rowe and S. E. Creager, Langmuir, 7 (1991) 2307.

[39] G. K. Rowe and S. E. Creager, Langmuir, 10 (1994) 1186.

[40] S. E. Creager and G. K. Rowe, Anal. Chim. Acta, 246 (1991) 233.

[41] S. E. Creager and G. K. Rowe, J. Electroanal. Chem., 370 (1994) 203.

[42] L. Zhang, T. Lu, G. W. Gokel, and A. E. Kaifer, Langmuir, 9 (1993) 786.

[43] K. Tamada, M. Hara, H. Sasabe, and W. Knoll, Langmuir, 13 (1997) 1558.

[44] W. A. Hayes and C. Shannon, Langmuir, 12 (1996) 3688.

[45] S. J. Stranick, A. N. Parikh, Y. T. Tao, D. L. Allara, and P. S. Weiss, J. Phys. Chem., 98 (1994) 7636.

[46] E. B. Troughton, C. D. Bain, G. M. Whitesides, R. G. Nuzzo, D. L. Allara, and M. D. Porter, Langmuir, 4 (1988) 365.

[47] J. P. Folkers, P. E. Laibinis, G. M. Whitesides, and J. Deutch, J. Phys. Chem., 98 (1994) 563.

[48] D. A. Offord, C. M. John, and J. H. Griffin, Langmuir, 10 (1994) 761.

[49] H. Schonherr and H. Ringsdorf, Langmuir, 12 (1996) 3891.

[50] H. Schonherr, H. Ringsdorf, M. Jaschke, H.-J. Butt, E. Bamberg, H. Allinson, and S. D. Evans, Langmuir, 12 (1996) 3898.

[51] D. Hobara, M. Ota, S.-I. Imabayashi, K. Niki, and T. Kakiuchi, J. Electroanal. Chem., 444 (1998) 113.

[52] J. F. Kang, R. Jordan, and A. Ulman, Langmuir, 14 (1998) 3983.

[53] J. F. Kang, A. Ulman, S. Liao, and R. Jordan, Langmuir, 15 (1999) 2095.

[54] S.-I. Imabayashi, M. Iida, D. Hobara, Z. Q. Feng, K. Niki, and T. Kakiuchi, J. Electroanal. Chem., 428 (1997) 33.

[55] M. Nishizawa, T. Sunagawa, and H. Yoneyama, J. Electroanal. Chem., 436 (1997) 213.

[56] S.-I. Imabayashi, D. Hobara, T. Kakiuchi, and W. Knoll, Langmuir, 13 (1997) 4502.

[57] A. J. Guiomar, J. T. Guthrie, and S. D. Evans, Langmuir, 15 (1999) 1198.

[58] C. D. Bain, H. A. Biebuyck, and G. M. Whitesides, Langmuir, 5 (1989) 723.

[59] M. M. Walczak, C. Chung, S. M. Stole, C. A. Widrig, and M. D. Porter, J. Am. Chem. Soc., 113 (1991) 2370.

[60] C. D. Bain and G. M. Whitesides, J. Am. Chem. Soc., 111 (1989) 7164.

[61] M. M. Walczak, D. D. Popenoe, R. S. Deinhammer, B. D. Lamp, C. Chung, and M. D. Porter, Langmuir, 7 (1991) 2687.

[62] Y. Sato and F. Mizutani, Electroanalysis, 10 (1998) 633.

[63] M. M. Walczak, C. A. Alves, B. D. Lamp, and M. D. Porter, J. Electroanal. Chem., 396 (1995) 103.

[64] D. E. Weisshaar, M. M. Walczak, and M. D. Porter, Langmuir, 9 (1993) 323.

[65] A. P. Brown and F. C. Anson, Anal. Chem., 49 (1977) 1589.

[66] L. Sun and R. M. Crooks, J. Electrochem. Soc., 138 (1991) L23.

[67] C. A. McDermott, M. T. McDermott, J.-B. Green, and M. D. Porter, J. Phys. Chem., 99 (1995) 13257.

[68] C. Schoenenberger, J. A. M. Sondag-Huethorst, J. Jorritsma, and L. G. J. Fokkink, Langmuir, 10 (1994) 611.

[69] J. A. M. Sondag-Huethorst, C. Schonenberger, and L. G. J. Fokkink, J. Phys. Chem., 98 (1994) 6826.

[70] M. Sugawara, K. Kojima, H. Sazawa, and Y. Umezawa, Anal. Chem., 59 (1987) 2842.

[71] F. Malem and D. Mandler, Anal. Chem., 65 (1993) 37.

[72] J. Wang, H. Wu, and L. Angnes, Anal. Chem., 65 (1993) 1893.

[73] J. H. Kim, T. M. Cotton, and R. A. Uphaus, J. Phys. Chem., 92 (1988) 5575.

[74] M. T. Rojas, R. Koniger, J. F. Stoddart, and A. E. Kaifer, J. Am. Chem. Soc., 117 (1995) 336.

[75] O. Chailapakul and R. M. Crooks, Langmuir, 11 (1995) 1329.

[76] R. Bilewicz, T. Sawaguchi, R. V. Chamberlain, II, and M. Majda, Langmuir, 11 (1995) 2256.

[77] J.-B. D. Green, M. T. McDermott, and M. D. Porter, J. Phys. Chem., 100 (1996) 13342.

[78] N. J. Simmons, Ph.D. Thesis, Iowa State University, Ames, 1997.

Table 1. Infrared spectroscopic band assignments and peak positions for MBA and HT mixed monolayers on annealed gold on mica.

	peak position (cm^{-1})	
Band Assignment[a]	MBA[b]	HT[c]
ν(O-H)	3579	
ν(C=O)	1749	
ν(C=C, aromatic)	1480, 1589	
δ(O-H•••O)/ν(C-OH)	1400-1430	
δ(O-H)	1364	
ν(C-OH)	1189	
δ(C-H, ip, aromatic)	1015, 1093, 1173	
$\nu_a(CH_2)$		2921
$\nu_s(CH_2)$		2852
$\nu_a(CH_3$, ip)		2966
$\nu_s(CH_3, FR_1)$		2939
$\nu_s(CH_3,FR_2)$		2878

[a] Key: ν, stretch; δ, bend; a, asymmetric; s, symmetric; ip, in-plane; FR_1 and FR_2, Fermi-resonance couplet of the higher and lower energy components, respectively.
[b] from [20]
[C] from [17]

Table 2. Values of integrated charge (μC) and total integrated charge (μC) under voltammetric reductive desorption waves for MBA and HT mixed monolayers on annealed Au/mica as a function of immersion time. The total charge per geometric area (μC/cm^2) for single-component MBA and HT are also listed.

Immersion Time (min)	Charge from MBA (μC)	Charge from HT (μC)	Total charge (μC)	Total Charge/cm^{-2} (μC/cm^2)[a]
1	24.2	8.7	32.9	56.7
15	23.9	23.9	47.8	82.4
60	23.2	22.5	45.7	78.8
90	23.5	27.4	50.9	87.8
210	22.5	26.7	49.2	84.8
9660	10.0	37.8	47.8	82.4
MBA alone[b]				67.6 ±5
HT alone[c]				90.0 ±7

[a] The total charge per area is calculated by dividing the total charge by the O-ring size of 0.58 cm^2.
[b] from ref [78]
[C] from ref [24]

Figure Captions

Figure 1. A schematic illustrates two extreme cases in the phase behavior of the MBA/HT mixed monolayer. The top one is a phase separated monolayer where individual islands of MBA and HT adsorbates exist on the terraces. The bottom one is a completely homogeneously mixed monolayer which the two components are homogeneously distributed on the surface.

Figure 2. IRRAS spectra of monolayers of (A) HT, (B) MBA/HT, R=1, (C) MBA/HT, R=100, and (D) MBA formed at annealed Au/mica with 5 min immersion.

Figure 3. Precursor composition dependence of the HT coverage. The symmetric methyl stretching mode absorbance at ~2877cm^{-1} from HT of MBA/HT monolayer is plotted against the composition of the precursor solutions. The thin solid line is determined with 15 min immersion. The dotted line is determined with 90 min immersion. The thick solid line shows the idealized absorbance when there is no preferential adsorption and the surface composition of the monolayers is the same as the precursor solutions.

Figure 4. Cyclic voltammograms of the reductive desorption of monolayers from MBA (bottom left), HT (bottom right), and MBA/HT (top) at Au/mica in 0.5 M KOH. The mixed monolayer electrode was formed from precursor solution of R=19, with 15 min immersion. Sweep rate is 50 mV/s. Electrode geometric area is 0.58 cm^2. Initial potential, -200 mV. Potential reversed at -1350 mV.

Figure 5. Cyclic voltammograms of the reductive desorption of MBA/HT mixed monolayers formed from precursor solutions of different R. Immersion time for all samples is 5 min. Electrolyte is 0.5 M KOH. Sweep rate is 50 mV/s. Electrode geometric area is 0.58 cm^2. Initial potential: -200 mV. Potential reversed at -1350 mV.

Figure 6. Cyclic voltammograms of the reductive desorption of MBA/HT mixed monolayers formed from precursor solution of R=19. Electrolyte is 0.5 M KOH. Sweep rate is 50 mV/s. Electrode geometric area is 0.58 cm^2. The two dashed lines are diagnostic reductive desorption potentials of MBA (at -580 mV) and HT (at -880 mV). Initial potential: -200 mV. Potential reversed at -1350 mV.

Figure 7. A schematic depiction of how MBA and HT adsorbates distributed on gold surfaces during immersion. The dark circles represent the HT adsorbates and the light circles represent the MBA adsorbates. (A) 1 min immersion, $E_{p, MBA}$ is -540 mV, (B) 15 min immersion, $E_{p, MBA}$ is -650 mV, (C) 60 min immersion, $E_{p, MBA}$ is -700 mV, (D) 90 min immersion, $E_{p, MBA}$ is -725 mV, and (E) 210 min immersion, $E_{p, MBA}$ is -735 mV, (F) 161 hours immersion, $E_{p, MBA}$ is 755 mV.

Figure 8. IRRAS spectra of MBA/HT mixed monolayers immersed in solution of R=19 for (A) 15 min and (B) 90 min.

Figure 9. A STM image (56 nm x 56 nm) of a mixed monolayer acquired from a sample of HT monolayer that has been immersed in 1mM MBA for 120 hr. The smooth or low regions are HT domains. The rougher and appeared higher areas outside of the HT domains are the regions occupied by the MBA adsorbates that have replaced the HT adsorbates. Setpoint current: 500 pA. Bias voltage: 900 mV.

Figure 10. STM images (100 nm x 42 nm) of MBA/HT mixed monolayers immersed in solution of R=19 for (A) 15 min. and (B) 90 min. The surface became more homogeneous with longer immersion time in precursors solutions. Setpoint current: 600 pA for (A) and 500 pA for (B). Bias voltage: 600 mV for both (A) and (B).

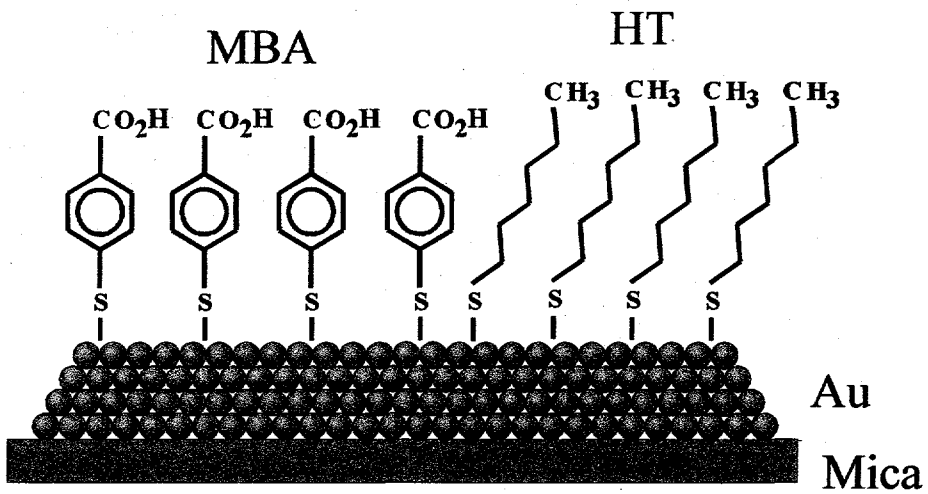

Phase Separated

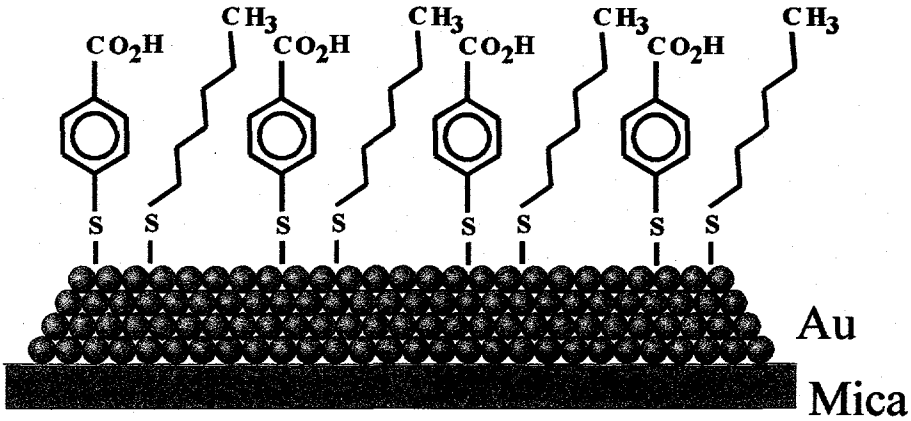

Homogeneously Mixed

Figure 1

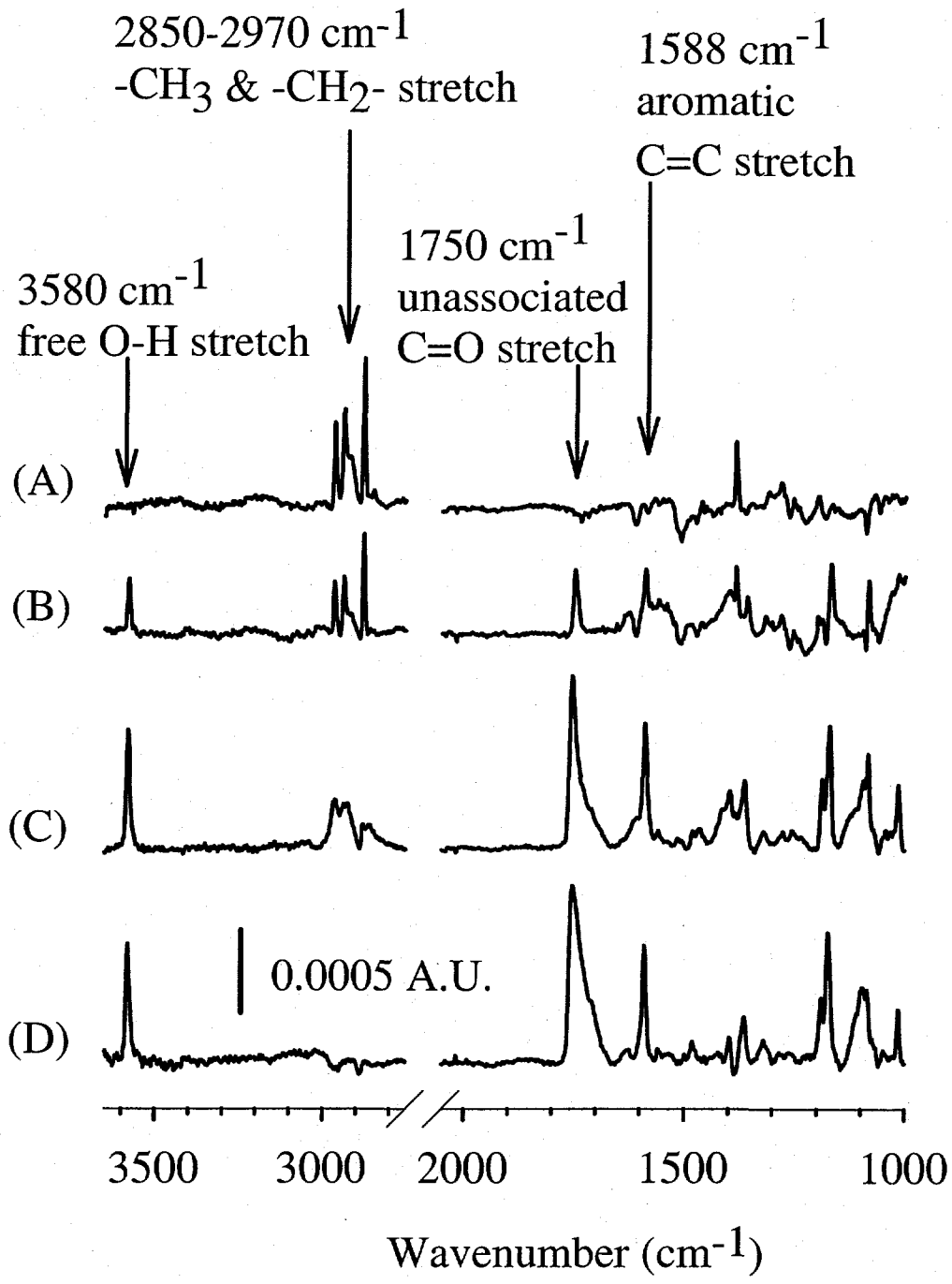
2850-2970 cm-1
-CH3 & -CH2- stretch
1588 cm-1
aromatic
C=C stretch
1750 cm-1
unassociated
C=O stretch
3580 cm-1
free O-H stretch
(A)
(B)
(C)
(D)
0.0005 A.U.
3500
3000
2000
1500
1000
Wavenumber (cm-1)

Figure 2

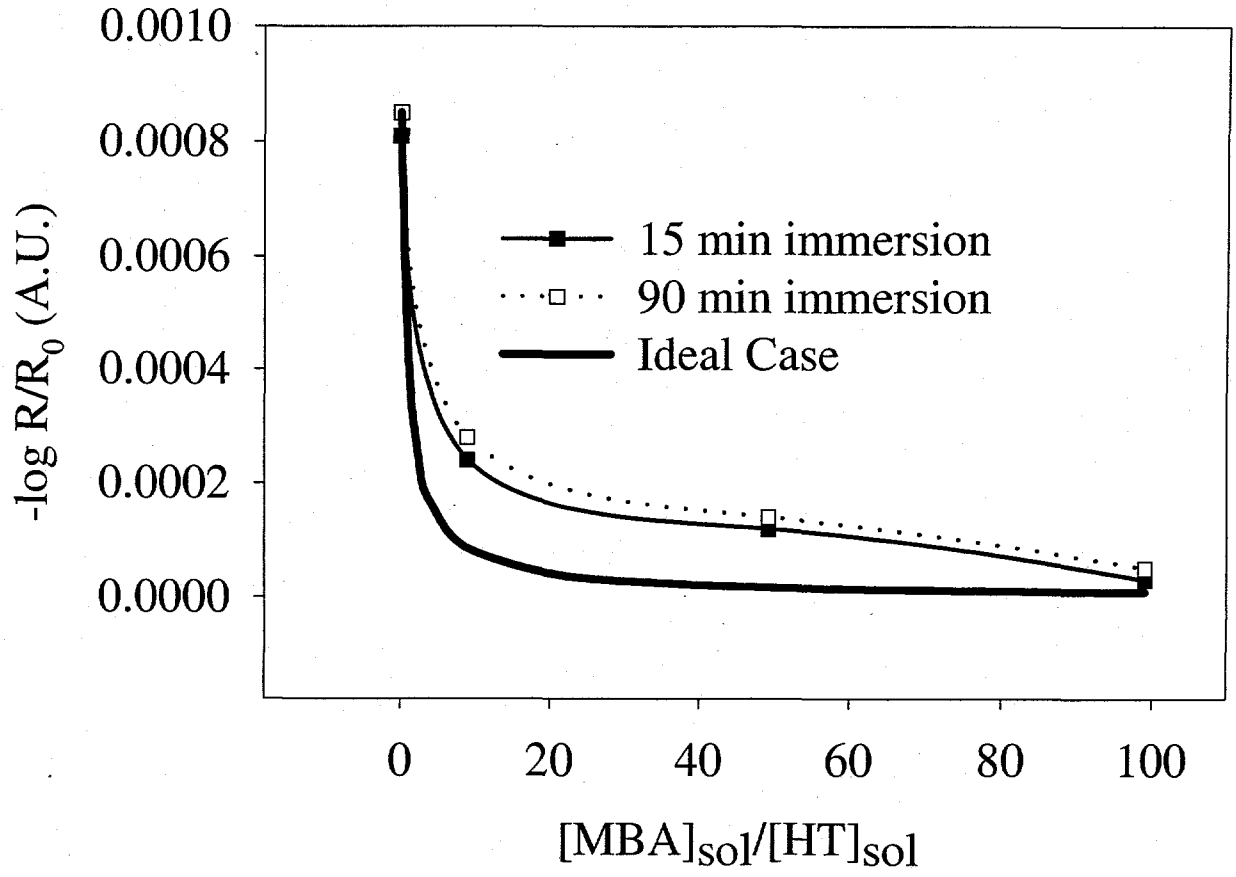
0.0010
0.0008
0.0006
0.0004
0.0002
0.0000
-log R/R0 (A.U.)
15 min immersion
90 min immersion
Ideal Case
0
20
40
60
80
100
[MBA]sol/[HT]sol

Figure 3

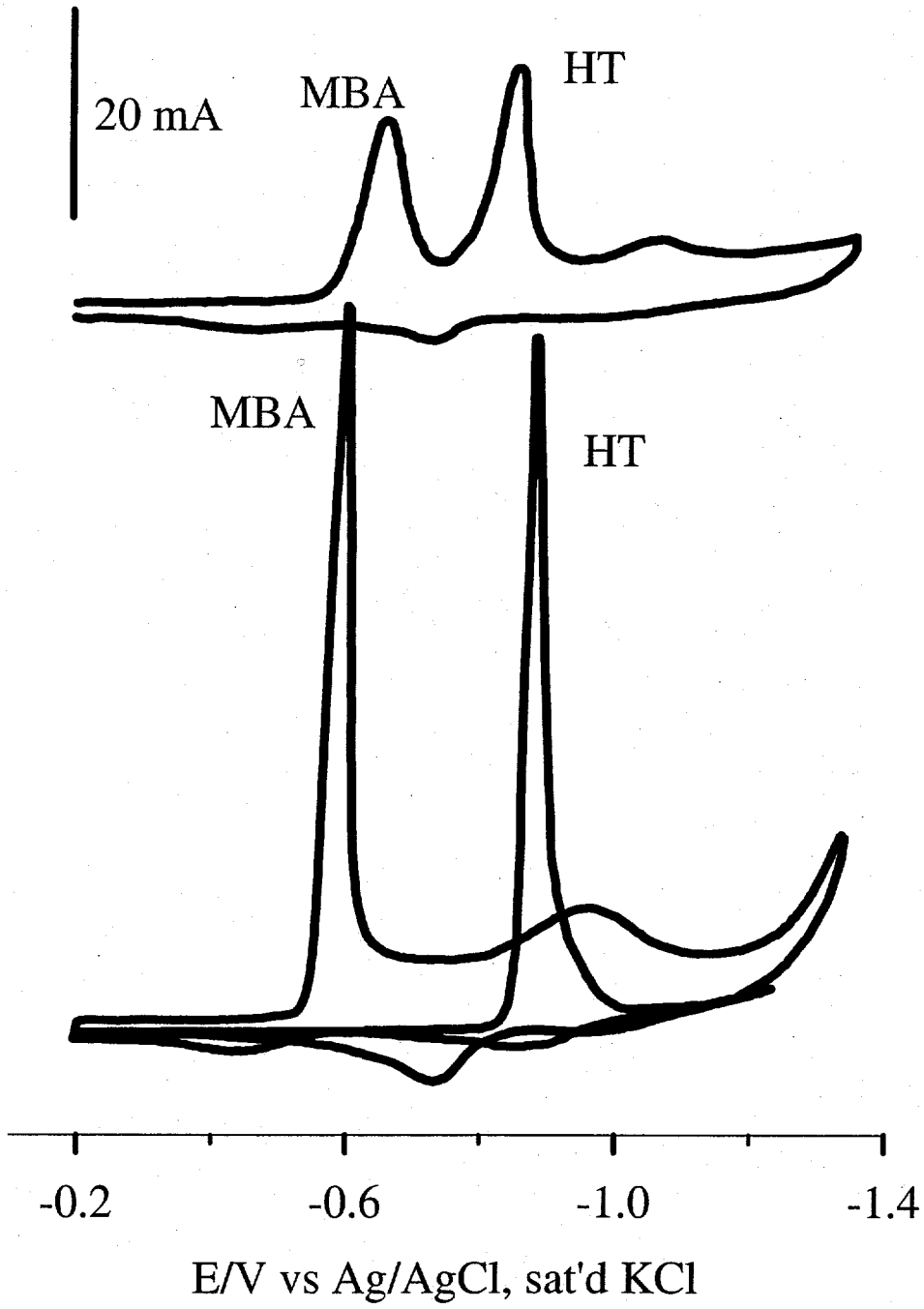

Figure 4

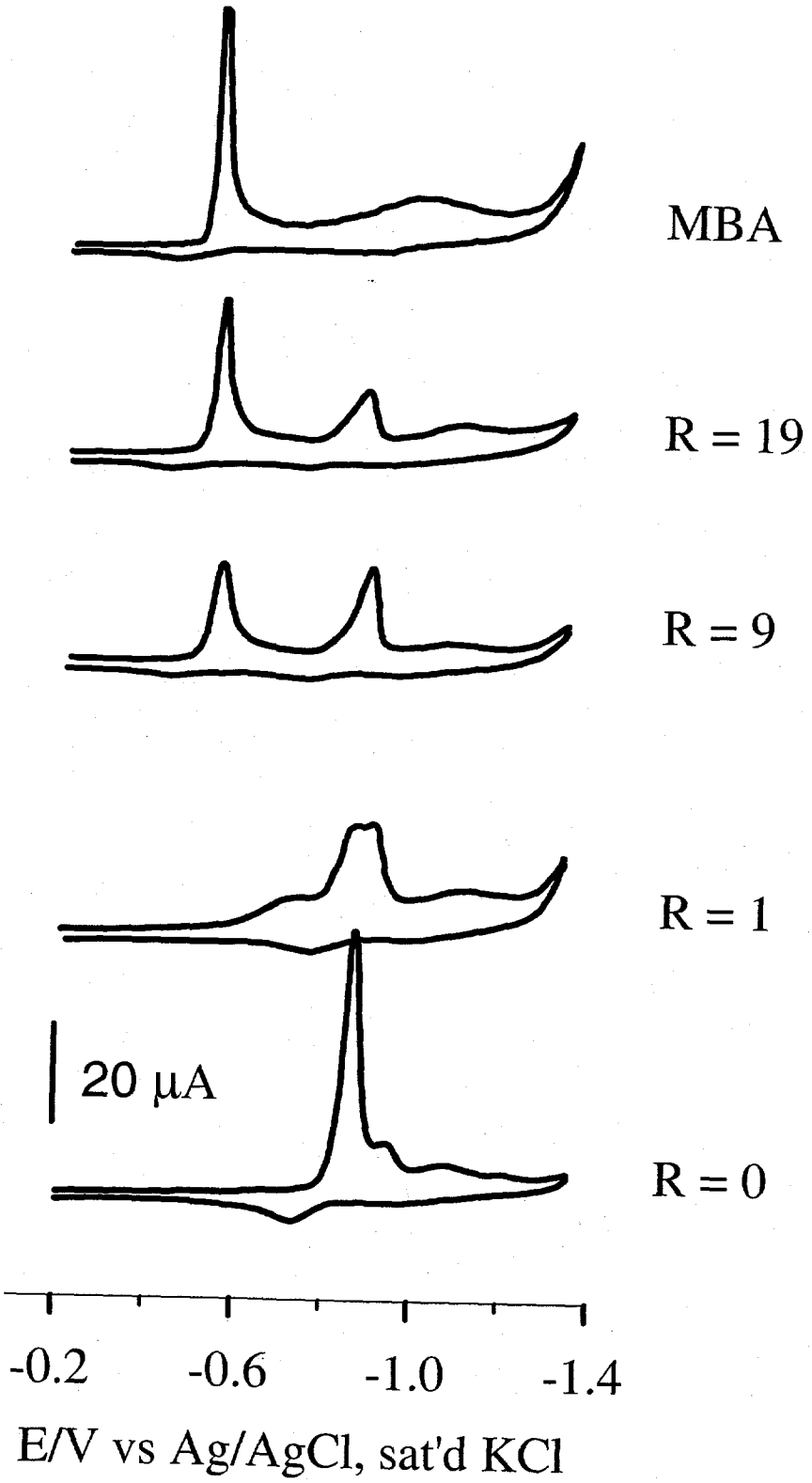

Figure 5

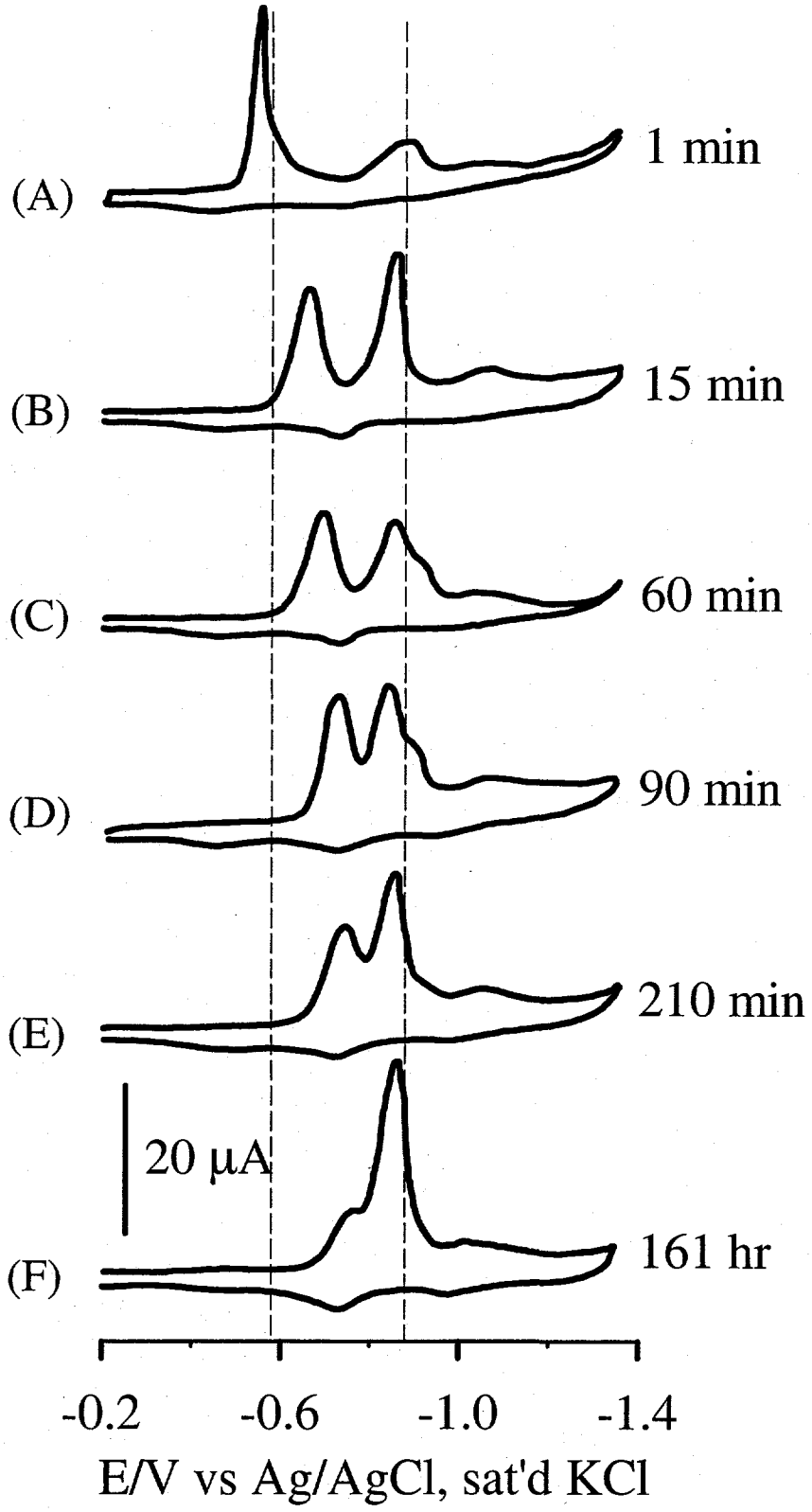
(A)
1 min
(B)
15 min
(C)
60 min
(D)
90 min
(E)
210 min
20 μA
(F)
161 hr
-0.2
-0.6
-1.0
-1.4
E/V vs Ag/AgCl, sat'd KCl

Figure 6

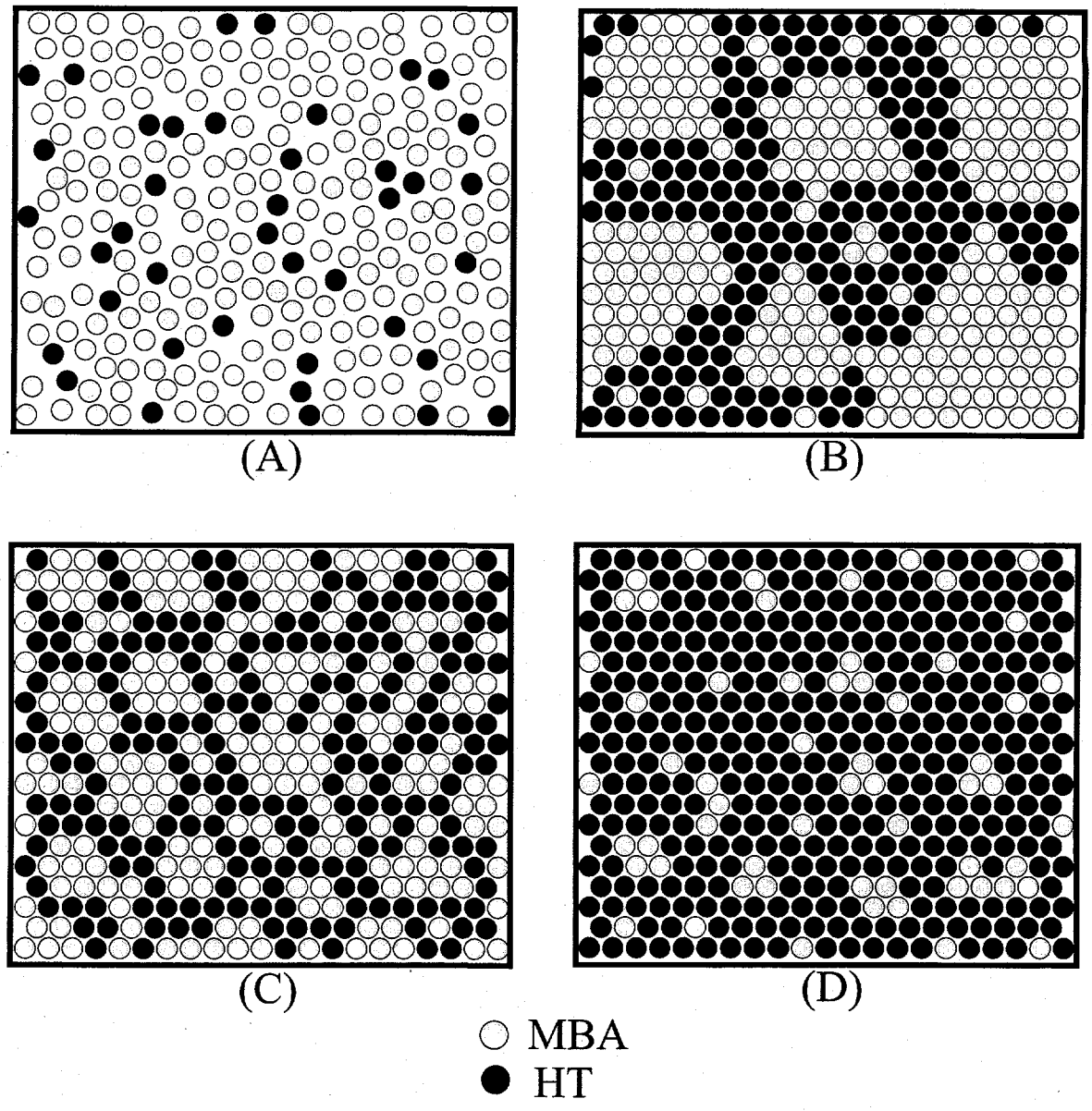

Figure 7

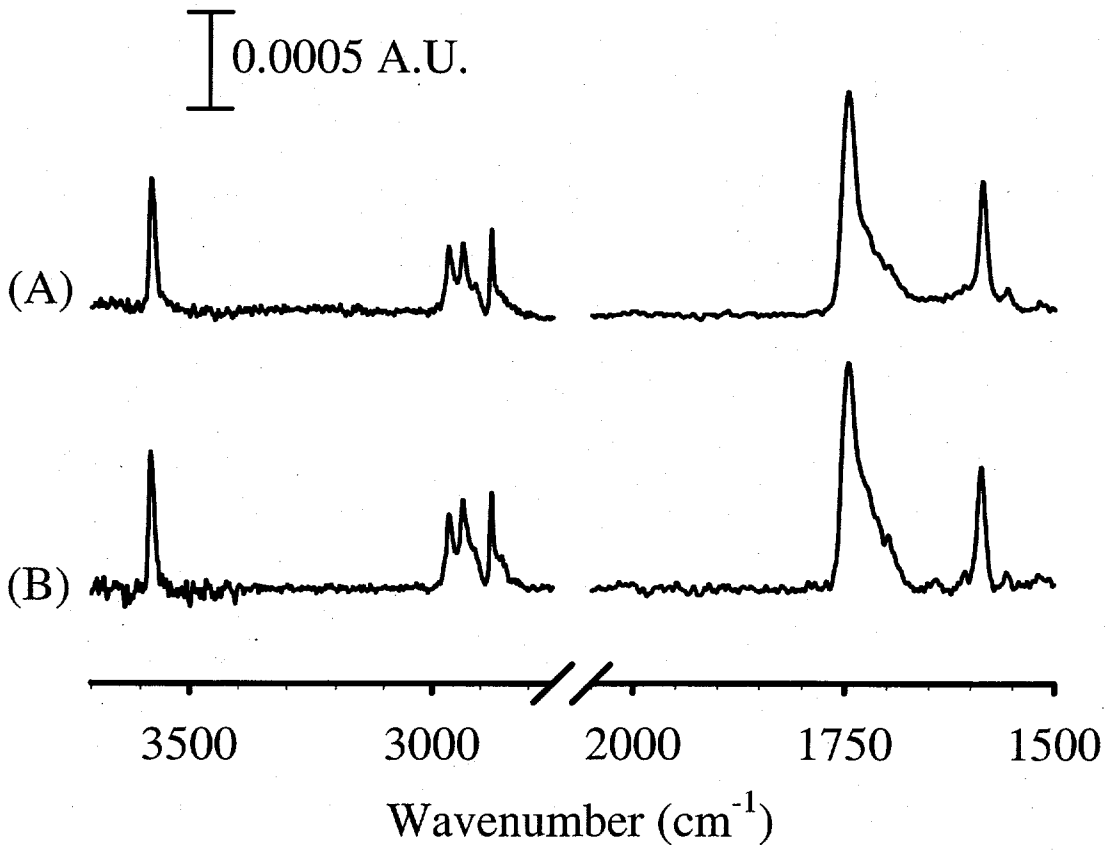

Figure 8

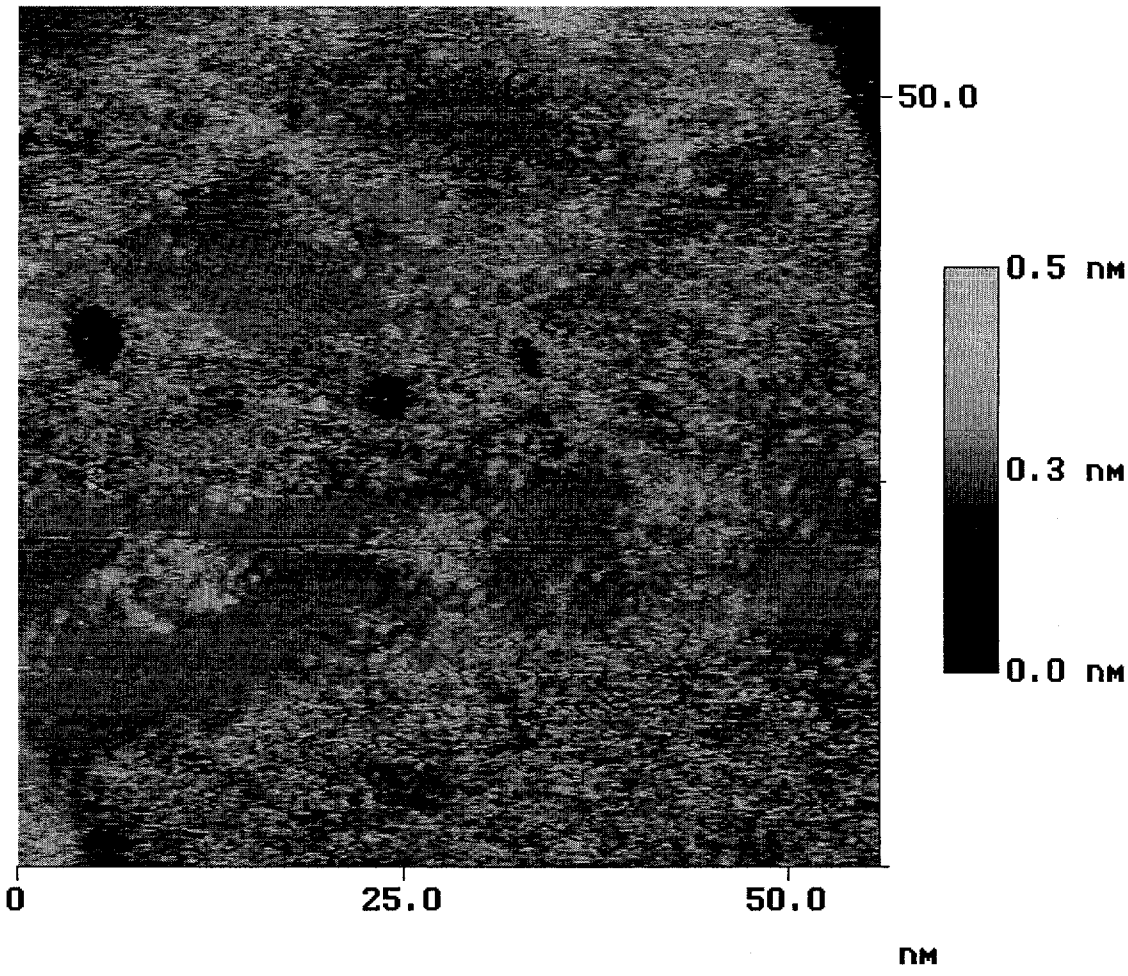

Figure 9

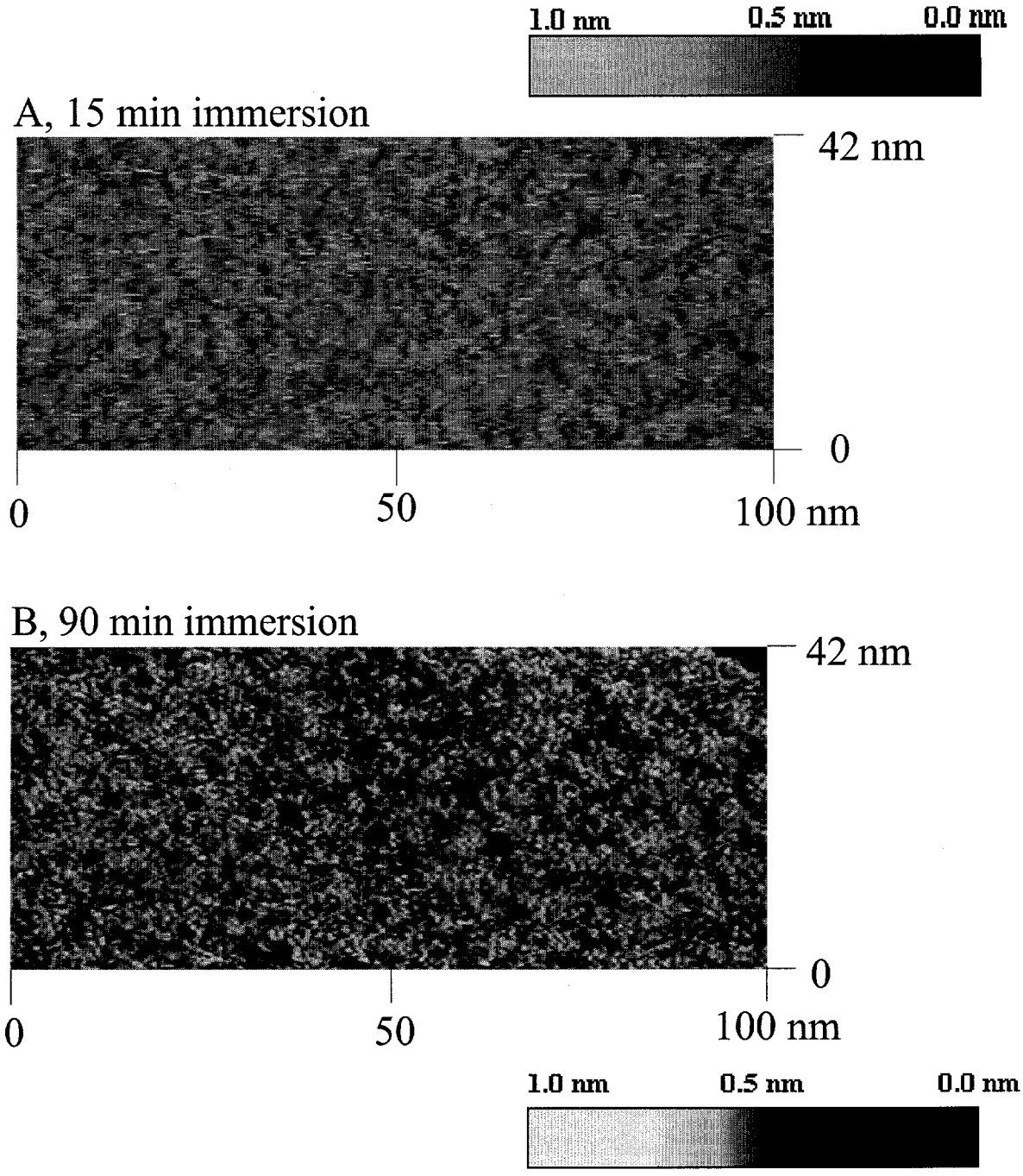
1.0 nm
0.5 nm
0.0 nm
A, 15 min immersion
42 nm
0
0
50
100 nm
B, 90 min immersion
42 nm
0
0
50
100 nm
1.0 nm
0.5 nm
0.0 nm

Figure 10

CHAPTER 4. MAPPING ORIENTATION DIFFERENCES OF TERMINAL FUNCTIONAL GROUPS BY FRICTION FORCE MICROSCOPY

A paper published in Analytical Chemistry[1]

Sze-Shun Wong, Hajime Takano, and Marc D. Porter[2]

Abstract

The ability to map differences in the spatial orientation of terminal chemical groups is of major significance to areas as diverse as biological recognition and boundary lubrication. This capability is demonstrated herein using a scanning force microscope to detect differences in the friction between a probe tip and organic monolayers with different terminal group orientations. As a starting point, the basis for the discrimination of the orientation differences in terminal groups is developed through considerations of surface free energy. The viability of the concept is then confirmed by the friction imaging of samples patterned with alternating domains of organic monolayers having different terminal group orientations. Opportunities presented by this new capability are briefly noted.

---

[2]Author to whom correspondence should be addressed.

Introduction

A host of significant processes in the life and physical sciences (e.g., biological recognition, heterogeneous catalysis, and mechanical lubrication) are controlled by interfacial architectures.[1] The development of methods that can detect differences in the composition and orientational disposition of these architectures at high spatial resolution is therefore technologically important. This level of information is also essential for advancing insights into the molecular level origins of many interfacial processes. To these ends, several recent investigations have explored the utility of the many variants of scanning force microscopy (SFM) to map the chemical group distribution of surfaces,[2-9] exploiting a range of interfacial properties (e.g., friction and adhesion) as contrast mechanisms. In furthering our interests in this area,[8,9] this paper presents the first findings that demonstrate the orientation mapping capabilities of friction force microscopy (FFM) via a correlation between the detected friction and the difference in the terminal group orientation of organic monolayers.

Friction at a microcontact is a function of the contact load, the area of the contact, and the surface free energies of the two contacting materials.[10] In general, an increase in any of these three parameters results in an increase in friction.[11] It is the demonstrated role of surface free energy[4,8] that motivated us to consider extending FFM to the detection of differences in the orientation of the terminal groups at surfaces. We postulated that if the orientation of terminal groups contributes to surface free energy, then FFM may provide a means to map orientation distributions at nanometer length scales.[12]

The feasibility of this concept is perhaps best assessed by considering the well established chain length dependence of the orientation for the terminal methyl group of monolayers chemisorbed at gold surfaces from dilute solutions of *n*-alkanethiols ($CH_3(CH_2)_nSH$, n>12).[13] As developed in a series of detailed infrared reflection spectroscopic investigations,[13-15] the dependence of the methyl group orientation arises from the ~24° tilt of the all trans alkyl chains with respect to the surface normal. Figure 1 depicts the general structural features of this system. Thus, the permanent dipole moment of the methyl group, which closely coincides with that for the transition dipole of the symmetric methyl stretching mode, is canted more from the surface normal when n is even (~53°) than when n is odd (~26°).[15]

The above "odd-even" effect translates to subtle differences in the wettability for several of the most studied monolayer systems.[16-19] Monolayers, for example, of *n*-alkanoic acids chemisorbed on silver surfaces exhibit contact angles that differ by as much as 5° because of the odd-even variation in the methyl group orientation.[16,18] Though near the detection limit of the characterization, contact angles for the gold-bound monolayers prepared from *n*-alkanethiols have been reported that are ~2° larger when n is odd than when n is even.[18-20] It then follows that the surface free energies of these systems are correlated with the spatial orientation of the terminal methyl group.[21] If then the difference in surface free energy results in a detectable difference in friction, FFM should be able to discriminate between domains of orientationally distinct terminal groups. We can further project that the gold-supported monolayers with an even number of methylene units should have a slightly

higher friction than those with an odd number of methylene units because the surface free energy is slightly larger when n is even than when n is odd.

Before presenting the results of our concept tests, we note that FFM has been applied to investigate friction at the microcontacts formed between probe tips and surfaces modified with *n*-alkanethiol-derived monolayers and other similar systems.[22-23] These studies focused largely on the use of monolayers as models for unraveling the fundamentals of lubrication. The sensitivity of friction to differences in the orientation of terminal functional groups has, to our knowledge, not been explored.

Experimental

Sample Preparation. Substrates were prepared by the vapor deposition of 300 nm of gold onto fleshly cleaved mica (B & M Trading Inc.) at ambient temperatures. The deposition rate was ~0.3 nm/s. The pressure in the cryopumped Edwards E360A coating system during evaporation was less than 9×10^{-5} Pa. The gold-coated substrates were then annealed at 300 °C for 5 hours in a muffle furnace; this process yields a surface composed of large (100-200 nm) atomically smooth Au(111) crystallites.[24]

Patterns of *n*-alkanethiol-based monolayers were prepared in two steps. This process was designed to yield micron-sized domains of an adlayer where n is odd-numbered that were surrounded by similar sized domains where n is even-numbered. The first step used microcontact printing (μP) [25] to stamp an adlayer of length n in a predefined pattern onto a gold surface. The second step employed the solution deposition (SD) of an *n*-alkanethiol of

length n±1 to fill in the areas on the gold surface intentionally not coated by the stamping process. This procedure not only results in a modified surface where the orientation of the terminal groups in neighboring domains are determined by whether n is even or odd, but also facilitates the identification of the orientationally distinct domains by the shapes of the patterns defined during the stamping process. The concentrations of the ethanolic thiol solutions for microcontact printing and solution deposition were 10 and 1 mM, respectively, and exposure times were 30 seconds and 10 minutes, respectively.

Characterizations Using FFM. A MultiMode NanoScope III SFM (Digital Instruments), equipped with a 130 μm tube scanner and operated in the ambient, was utilized for all FFM characterizations. All images were collected in the contact mode using 100 μm, oxide sharpened Si_3N_4 cantilevers (Nanoprobes), with normal bending and torsional force constants of ~0.38 N/m and ~100 N/m, respectively. Plots of friction (f) vs. contact load (F_N) were developed from friction loops collected over 10-nm scan lines on an atomically flat portion of each sample surface at a rate of ~0.16 μm/s. The values of the normal bending and the torsional force constants of the 200 μm, oxide sharpened, Si_3N_4 cantilever (Nanoprobes) used for the determinations of F_N and f are 0.12 N/m and 150 N/m, respectively.

We note that small transient changes in the friction contrast in the fast scan direction of the images were occasionally observed. We attribute the transients to changes in the surface composition (e.g., contaminant sorption/loss) of the tip during imaging.

Reagents. Ethanol (Quantum, punctilious grade) was used as received. *n*-alkanethiols (n = 13-15, 17) were acquired from several sources (Aldrich, n = 15,17; Pfaltz &

Bauer, Inc., n = 13; Columbia Organic Chemical, n = 14) and were used as received. Tridecanethiol (n = 12) and heptadecanethiol (n = 16) were synthesized according to literature procedures.[26]

Results and Discussion

To test this mapping concept, FFM was used to image *n*-alkanethiol-based monolayers patterned in a two-step process on gold films that have large (100-200 nm), atomically smooth terraces with a (111)-surface crystallinity.[24] As discussed, the patterning process was designed to yield micron-sized domains of an adlayer where n is odd-numbered that were surrounded by similar sized domains where n is even-numbered. This procedure has two attributes: 1) the orientation of the terminal groups in neighboring domains are determined by whether n is even or odd, and 2) the identification of the orientationally distinct domains is facilitated by the shapes of the patterns defined during the stamping process.

The ability to detect differences in the terminal group orientation of these samples is demonstrated by the series of friction images (120 μm x 120 μm) in Figure 2. These images were collected at a contact load of ~25 nN using uncoated, oxide-sharpened Si_3N_4 probe tips. Figure 2A is an image of a sample that was first stamped with an n=15 adlayer (n_{15}(μP)), followed by the solution deposition of an n=16 adlayer (n_{16}(SD)). Thus, the dipole moment of the methyl groups in the n_{15}(μP) domains is oriented more towards the surface normal than that of the methyl groups in the n_{16}(SD) domains. As is evident, the friction between the

probe tip and n_{16}(SD) domains is greater than that between the probe tip and n_{15}(μP) domains.

This result establishes that FFM can detect the differences in surface free energies that correlate with the orientation difference of the terminal methyl groups. Moreover, the observed difference in friction tracks with the expectation based on the relative surface free energies of the two orientationally distinct domains. That is, the microcontact formed at the higher surface free energy domains of n_{16}(SD) exhibit a larger friction than that formed at the lower surface free energy domains of n_{15}(μP).

As a control experiment, the patterning sequence used to prepare the sample in Figure 2A was reversed. This experiment assessed whether the friction difference in Figure 2A was an artifact of the preparative method, a concern reflected by the limited number of structural comparisons of the adlayers formed by the two different procedures.[27] The image in Figure 2B is therefore of a sample patterned with n_{16}(μP) domains that are surrounded by n_{15}(SD) domains. Consistent with the results in Figure 2A, the friction in Figure 2B is greater at n_{16}(μP) than at n_{15}(SD), substantiating that the observed contrast correlates with the difference in terminal group orientation.

The friction images in Figures 2C-F build on the above findings. These images are of samples patterned by decreasing the length of the alkyl chain by one methylene unit for each of the alternating domains in Figures 2C,D and by two methylene units for those in Figures 2E,F. Figure 2C is then an image for n_{14}(μP) domains surrounded by n_{15}(SD) domains, whereas Figure 2D is an image for a sample prepared upon pattern reversal. Similarly,

Figures 2E,F are images for domains of $n_{13}(\mu P)$ and $n_{14}(SD)$ and of $n_{14}(\mu P)$ and $n_{13}(SD)$, respectively. In each case, the detected friction is greater when n is even-numbered as opposed to odd-numbered, paralleling the results in Figures 2A,B. We roughly estimate the lateral resolution in these two images at ~50 nm, as judged from the distance clearly separating orientationally different domains for images collected by scanning over smaller-sized areas (i.e., 2 μm) to increase pixel density.[28] Taken together, these correlations provide compelling evidence for the ability of FFM to map differences in the spatial orientation of terminal surface groups at the high lateral resolution of SFM techniques.

A more quantitative development of our findings is presented in Figure 3 through plots of friction (f) as a function of the contact load (F_N). These data, which were collected using solution deposited monolayers, are based on an analysis of the trace-retrace plots collected while scanning only across atomically flat regions of the samples to avoid contributions to the measurement from substrate topography.[29] As found in earlier studies of organic monolayer films,[4,8,23] the dependencies of f on F_N in Figure 3 can be described by a linear function. However, the slope of each plot (i.e., the coefficient of friction) increases with respect to n as 15<16<13<14<12. This trend, which is summarized by the inset plot of f vs. n at a F_N of 25 nN and includes the corresponding dependence of the magnitude for the symmetric methyl stretching mode using infrared reflection spectroscopy, substantiates the correlations established by the images in Figure 2.

The inset also shows that f undergoes a gradual decrease as n increases. This trend suggests that there may be a mechanical contribution (e.g., adlayer elasticity[3,7,30]) from

differences in chain length that is superimposed on the correlation between friction and terminal group orientation. In other words, the trend in the data implies that there is a convoluted dependence of the compressibility for these adlayers on the magnitude of *n* and on whether n is even- or odd numbered. These interpretations, drawn from several structural assessments[1c], support a general decrease in the packing density, and therefore, the compressibility of these adlayers as n decreases. Spectroscopic experiments aimed at whether such a correlation can be developed based on whether n is odd- or even numbered are presently being designed.

Conclusions

In summary, our results show that the spatial orientation of the terminal groups at interfaces has a detectable impact on friction, notably extending the remarkable capability of FFM as a high resolution surface characterization technique. We believe that this new dimension in performance will potentially find widespread applications in the life and physical sciences, spanning areas such as biological sequencing and recognition, phase separated polymeric composites, and analytical separations. Efforts along some of these lines, as well as on the furthering our fundamental understanding of the friction process, are underway. We are also exploring the use of chemically modified probe tips[3-6,8] which, because of the role of surface free energies on the extent of the detected friction, can potentially be exploited to enhance image contrast.

Acknowledgements

Valuable discussions with V. W. Jones are gratefully appreciated. H. Takano acknowledges a Post-Doctoral Fellowship through the Institute of Physical Research and Technology of Iowa State University. This work was supported by the U.S. Department of Energy. The Ames Laboratory is operated for the U.S. Department of Energy by Iowa State University under Contract No. W-7405-eng-82.

References and Notes

1. (a) Mallouk, T. E.; Harrison, D. J. *ACS Symposium Series 561: Interfacial Design and Chemical Sensing*; American Chemical Society: Washington, DC, 1994. (b) Israelachvili, J. N. *Intermolecular and Surface Forces: With Applications to Colloidal and Biological Systems*; Academic Press: San Diego, CA, 1985. (c) Ulman, A. *An Introduction to Ultrathin Organic Films: From Langmuir-Blodgett to Self-Assembly*; Academic Press: San Diego, CA, 1991.

2. (a) Overney, R. M.; Meyer, E.; Frommer, J.; Brodbeck, D.; Lüthi, R; Howald, L; Güntherodt, H.-J.; Fujihira, M.; Takano, H.; Gotoh, Y. *Nature* **1992**, *359*, 133-135. (b) Frisbie, C. D.; Rozsnyai, L. F.; Noy, A.; Wrighton, M. S.; Lieber, C. M. *Science* **1994**, *265*, 2071-2974. (c) Dufrêne, Y. F.; Barger, W. R.; Green, J.-B. D.; Lee, G. U. *Langmuir* **1997,** *13*, 4779-4784. (d) Piner, R. D.; Mirkin, C. A. *Langmuir* **1997**, *13*, 6864-6868. (e) Hayes, W. A.; Kim, H.; Yue, X.; Perry, S. S.; Shannon, C. *Langmuir* **1997**,*13*, 2511-2518. (f) Zhou, Y.; Fan, H.; Fong, T.; Lopez, G. P. *Langmuir* **1998**, *14*, 660-666.

3. Thomas, R.C.; Houston, J. E.; Crooks, R. M.; Kim, T.; Michalske, T. A. *J. Am. Chem. Soc.* **1995**, *117*, 3830-3834.

4. Noy, A.; Frisbie, C. D.; Rozsnyai, L. F.; Wrighton, M. S.; Lieber, C. M. *J. Am. Chem. Soc.* **1995**, *117*, 7943-7951.

5. Wilbur, J. L.; Biebuyck, H. A.; MacDonald, J. C.; Whitesides, G. M. *Langmuir* **1995**, *11*, 825-831.

6. McKendry, R.; Theoclitou, M.-E.; Rayment, T.; Abell, C. *Nature* **1998**, *391*, 566-568.

7. Finot, M. O.; McDermott, M. T. *J. Am. Chem. Soc.* **1997**, *119*, 8564-8565.

8. Green, J.-B. D.; McDermott, M. T.; Porter, M.D.; Siperko, L. M. *J. Phys. Chem.* **1995**, *99*, 10960-10965.

9. (a) Green, J.-B. D.; McDermott, M. T.; Porter, M. D. *J. Phys. Chem.* **1996**, *100*, 13342-13345. (b) Wang, J.; Kenseth, J. R.; Jones, V. W.; Green, J.-B. D.; McDermott, M. T.; Porter, M. D. *J. Am. Chem. Soc.* **1997**, *119*, 12796-12799.

10. (a) Kendall, K. *Nature* **1986**, *319*, 203-205. (b) Pollock, H. M. In *Fundamentals of Friction: Macroscopic and Microscopic Processes*; Singer, I. L., Pollock, H. M., Eds.; Kluwer Academic Publishers, Dordrecht, The Netherlands, 1992; pp. 77-94. (c) Israelachvili, J. N. In *Handbook of Micro/Nano Tribology*; Bhushan, B., Ed.; CRC Press, Boca Raton, FL, 1995; pp.267-319.

11. Briscoe, B. J.; Evans, D. C. B. *Proc. R. Soc. London, Ser. A* **1982**, *380*, 389-407.

12. (a) Binnig, G.; Quate, C. F.; Gerber, Ch. *Phys. Rev. Lett.* **1986**, *56*, 930-933. (b) Mate, C. M.; McClelland, G. M.; Erlandsson, R.; Chiang, S. *Phys. Rev. Lett.* **1987**, *59*, 1942-1945.

13. (a) Nuzzo, R. G.; Dubois, L. H.; Allara, D. L. *J. Am. Chem. Soc.* **1990**, *112*, 558-569. (b) Laibinis, P. E. Whitesides, G. M.; Allara, D. L.; Tao, Y.-T.; Parikh, A. N.; Nuzzo, R. G. *J. Am. Chem. Soc.* **1991**, *113*, 7152-7167. (c) Bryant, M. A.; Pemberton, J. E. *J. Am. Chem. Soc.* **1991**, *113*, 8284-8293. (d) Li, T.-W.; Chao, I.; Tao, Y.-T. *J. Phys. Chem. B.* **1998**, *102*, 2935-2946.

14. Walczak, M. M.; Chung, C.; Stole, S. M.; Widrig, C. A.; Porter, M. D. *J. Am. Chem. Soc.* **1991**, *113*, 2370-2378.

15. Parikh, A. N.; Allara, D. L. *J. Chem. Phys.* **1992**, *96*, 927-945.

16. Tao, Y.-T. *J. Am. Chem. Soc.* **1993**, *115*, 4350-4358.

17. Smith, E. L.; Porter, M. D. *J. Phys. Chem.* **1993**, *97*, 8032-8038.

18. Chau, L. K. Ph.D. Dissertation, Iowa State University, 1990.

19. Chang, S.-C.; Chao, I.; Tao, Y.-T. *J. Am. Chem. Soc.* **1994**, *116*, 6792-6805.

20. These differences, which are found using hexadecane as the wettability probe liquid, are only just observed above the ± 1° repeatability of the measurement. We also see a 2° variation when using water as the probe liquid (Wong, S.-S.; Takano, H.; Porter, M. D. unpublished results).

21. Using Young's Equation and the literature value for the surface free energy of hexadecane (27.5 mJ/m^2) (Jasper, J. J. *J. Phys. Chem. Ref. Data* **1972**, *1*, 841), we estimate that the surface free energies for the odd and even-numbered monolayers with this system are ~20 mJ/m^2 and ~21 mJ/m^2 respectively.

22. (a) Xiao, X.; Hu, J.; Charych, D. H.; Salmeron, M. *Langmuir* **1996**, *12*, 235-237. (b) Lio, A.; Charych, D. H.; Salmeron, M. *J. Phys. Chem. B* **1997**, *101*, 3800-3805. (c)

Lio, A.; Morant, C.; Ogletree, D. F.; Salmeron, M. *J. Phys. Chem. B* **1997**, *101*, 4767-4773.

23. McDermott, M. T.; Green, J.-B. D.; Porter, M. D. *Langmuir* **1997**, *13*, 2504-2510.

24. Chidsey, C. D. E.; Loiacono, D. N.; Sleator, T.; Nakahara, S. *Surf. Sci.* **1988**, *200*, 45-66.

25. (a) Kumar, A,; Whitesides, G. M. *Appl. Phys. Lett.* **1993**, *63*, 2002-2004. (b) Kumar, A.; Biebuyck, H. A.; Whitesides,G. M. *Langmuir* **1994**, *10*, 1498-1511.

26. Bain, C .D.; Troughton, E. B.; Tao, Y.-T.; Evall, J.; Whitesides, G. M.; Nuzzo, R. G. *J. Am. Chem. Soc.* **1989**, *111*, 321-335.

27. (a) Bar, G.; Rubin, S.; Parikh, A. N.; Swanson, B. I.; Zawodzinski, T. A, Jr.; Whangbo, M.-H. *Langmuir* **1997**, *13*, 373-377. (b) Larsen, N. B.; Biebuyck, H.; Delamarche, E.; Michel, B. *J. Am. Chem. Soc.* **1997**, *119*, 3017-3026.

28. This estimate of resolution is based upon an analysis (see reference 8) of 2 μm-sized images, which were collected by scanning across partial portions of the patterned domains of the samples in Figures 2A,B. Issues related, for example, to the differences in the friction between domains, however, must be considered when attempting to translate the resolution estimated for the arrays in Figures 2A,B to other samples.

29. The friction responses reported in Figure 3 are approximately twice that described in our previous work (reference 23). This difference is attributed to differences in the types of tips used in the two separate studies. Our earlier data were obtained using conventional silicon nitride tips, whereas the results in Figure 3 were acquired using

oxide-sharpened tips. Thus, differences in the size, shape, and probable surface composition of the two types of tips result in the observed differences in the FFM-measured friction. Factors such as the mechanical properties of the tip, sample, and tip-sample microcontact, all of which we are presently attempting to detail further, also play roles that are not well understood.

30. Joyce, S. A.; Thomas, R. C.; Houston, J. E.; Michalske, T. A.; Crooks, R. M. *Phys. Rev. Lett.* **1992**, *68*, 2790-2793.

Figure Captions

Figure 1. Idealized structures for *n*-alkanethiolate monolayers chemisorbed at gold. The structure on the left is for an adlayer with an odd number of methylene groups in the alkyl chain, whereas that on the right is for an adlayer with an even number of methylene groups in the alkyl chain. The spatial dispositions of the dipole moment of the terminal methyl groups are approximated by the crossed arrows.

Figure 2. 120 μm x 120 μm friction images (z-scale = 0.2 V, with brighter contrast corresponding to higher friction) of *n*-alkanethiolate monolayers patterned on smooth gold by microcontact printing (μP), followed by solution deposition (SD). (A) n_{15}(μP), n_{16}(SD); (B) n_{16}(μP), n_{15}(SD); (C) n_{14}(μP), n_{15}(SD); (D) n_{15}(μP), n_{14}(SD); (E) n_{13}(μP), n_{14}(SD); and (F) n_{14}(μP), n_{13}(SD). The concentrations of the ethanolic thiol solutions for microcontact printing and solution deposition were 10 and 1 mM, respectively. The contact load was ~25 nN.

Figure 3. Plots of friction force (*f*) vs. the contact load (F_N) for *n*-alkanethiolate monolayers of varying chain length chemisorbed on smooth gold. The inset plots *f* vs. n at a F_N ~25 nN and the absorbance of the lower energy symmetric methyl stretching mode $\nu_s(CH_3)$ obtained for each monolayer using infrared

reflection spectroscopy (see reference 17 for experimental details). The systematic variation of the absorbance arises from the difference of the spatial orientation of the methyl groups with respect to the surface normal of the gold substrate.

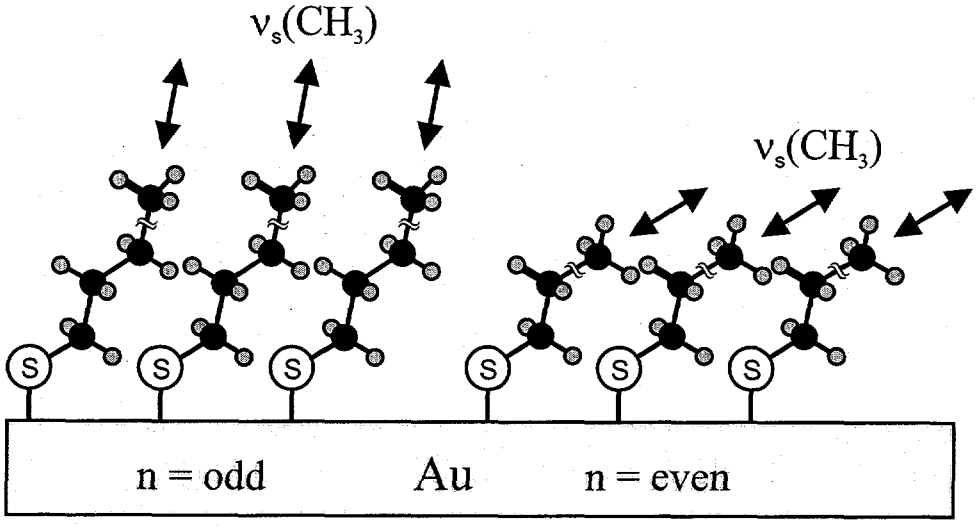

Figure 1

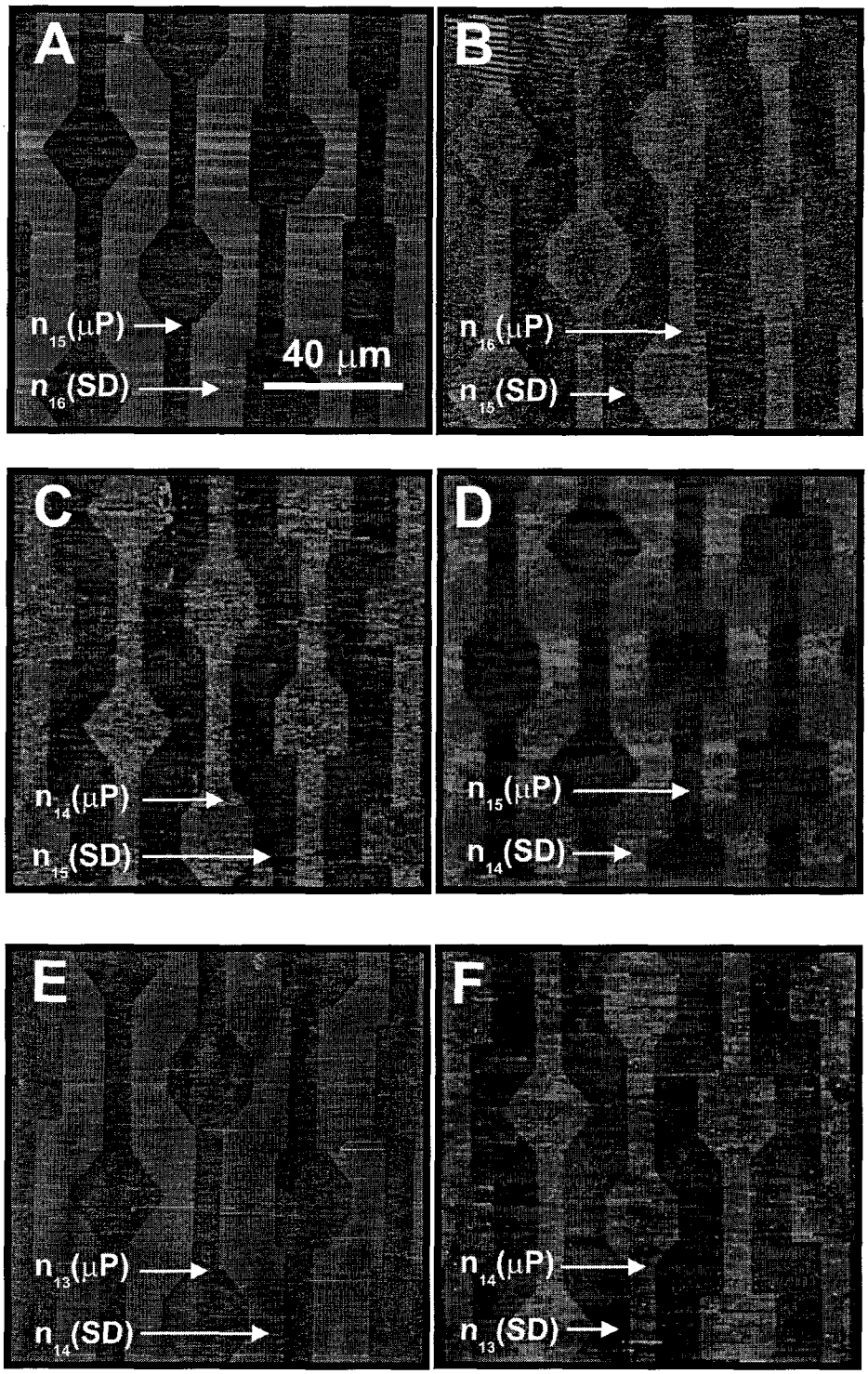
A
$n_{15}(\mu P)$
$n_{16}(SD)$
40 μm
B
$n_{16}(\mu P)$
$n_{15}(SD)$
C
$n_{14}(\mu P)$
$n_{13}(SD)$
D
$n_{15}(\mu P)$
$n_{14}(SD)$
E
$n_{13}(\mu P)$
$n_{14}(SD)$
F
$n_{14}(\mu P)$
$n_{13}(SD)$

Figure 2

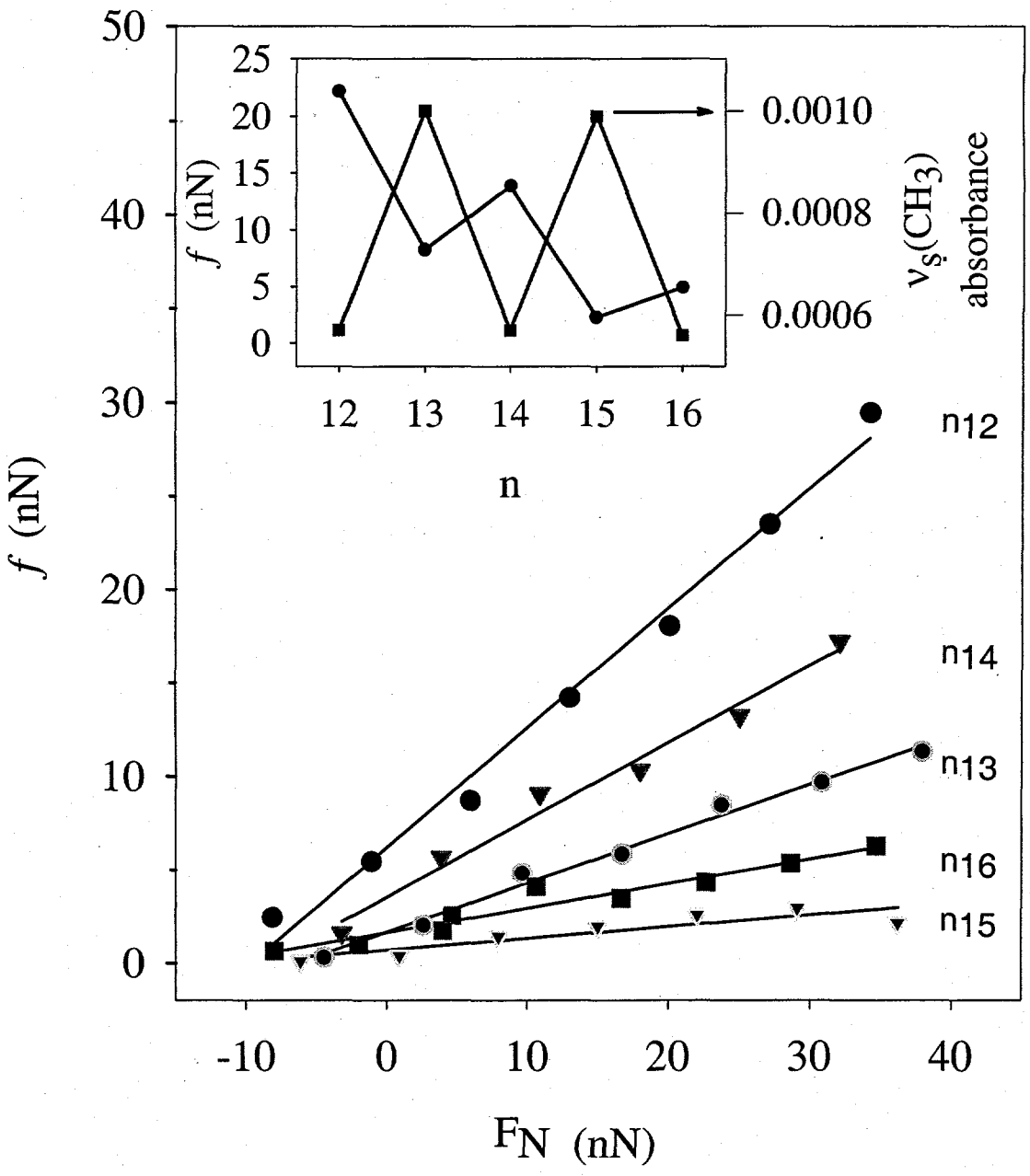
50
40
30
20
10
0
f (nN)
-10
0
10
20
30
40
F_N (nN)
n12
n14
n13
n16
n15
25
20
15
10
5
0
f (nN)
12
13
14
15
16
n
0.0010
0.0008
0.0006
ν_S(CH_3) absorbance

Figure 3

GENERAL CONCLUSIONS AND FUTURE PROSPECTUS

This dissertation has presented several results which add to the general knowledge base regarding organothiolates monolayers spontaneously adsorbed at gold films. Common to the body of this work is the use of voltammetric reductive desorption and variants of scanning probe microscopy to gain insight into the nature of the monolayer formation process as well as the resulting interface.

The most significant result from this work is the success of using friction force microscopy to discriminate the end group orientation of monolayers chemisorbed at smooth gold surfaces with micrometer resolution (Chapter 4). The ability to detect the differences in the orientational disposition is demonstrated by the use PDMS polymer stamp to microcontact print an adlayer of *n*-alkanethiolate of length n in a predefined pattern onto a gold surface, followed by the solution deposition of a *n*-alkanethiol of n±1 to fill in the areas on the gold surface intentionally not coated by the stamping process. These two-component monolayers can be discriminated by using friction force microscopy which detects differences in friction contributed by the differences in the orientation of the terminal groups at surfaces. This success has recently led to the detection of the orientation differences at nanometer scale. Although the substrates examined in this work consisted entirely of smooth gold films, the same test can be performed on other smooth substrates and monolayer materials.

Studies of the voltammetric reductive desorption process at short immersion times in Chapter 1 have shown that the substrate surface reconstructs during the formation of organothiolate monolayers at as-evaporated Au/mica and Au/glass. The extent of the

reconstruction is related to the length of alkanethiolates and the nature of the terminal function groups. Multi-technique characterization including electrochemical reductive desorption, IRRAS, GFAAS, and STM has provided both macroscopic and microscopic information which suggest that a cooperative process induced by thiolate binding to gold, in which the structural interactions among chains and end groups affect energetically the substrate reconstruction, is at work. Continued studies along this vein include the in-situ STM investigation of the substrate reconstruction during the formation of monolayer of different chain length and terminal functional groups.

The other studies described in this dissertation have primarily relied on voltammetric reductive desorption to 1) probe the origin of multiple voltammetric desorption waves of long chain alkanethiolate monolayers chemisorbed at annealed gold electrodes, and 2) examine the phase behavior of two-component monolayers formed from immersion of gold substrate into precursor ethanolic solution of alkanethiols and aromatic thiols. The origin of the multiple voltammetric desorption was concluded to be related to the different sizes of domains on large Au(111) terraces. The amount of each component and its spatial distribution on a two-component monolayer were found to be immersion time dependent and can be determined by monitoring the shift of reductive desorption peak potentials and the peak areas of each component.

The ability to manipulate surface architectures and control and characterize the interfacial properties of materials will continue to be dependent on the advancement of nano-technology. With the improvements in instrumentation (e.g. electrochemical hardware), the advent of new materials (e.g., nanoparticles), or the development of methods to manipulate

and characterize ever smaller-sized sample, the field of organothiolate monolayers will expand and more applications will be found.